AD-A156 030   LASER TARGET DESIGN SCALING FOR THE UPGRADED NRL (NAVAL   1/2
               RESEARCH LABORATO. (U) MISSION RESEARCH CORP
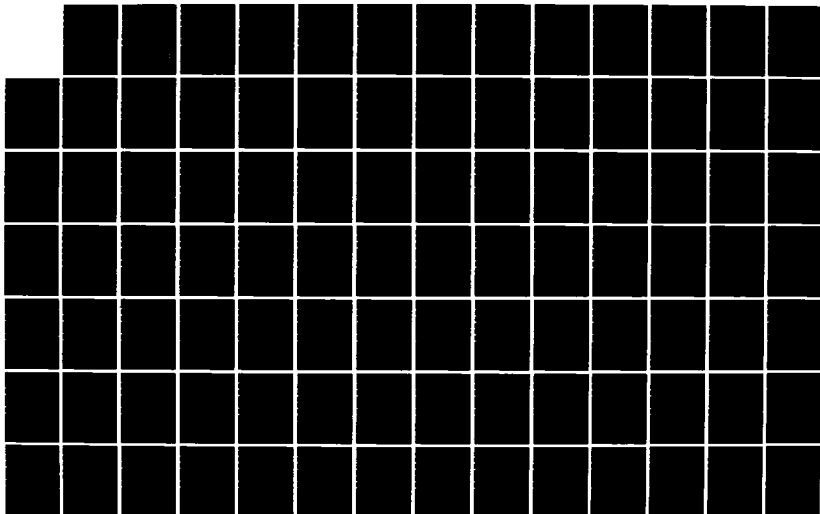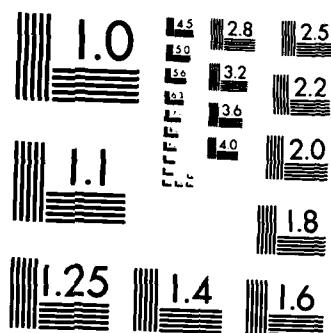   ALBUQUERQUE NM   R F STELLINGWERF 30 APR 84 AMRC-R-486
UNCLASSIFIED   DNA-TR-84-174 DNA001-82-C-0120   F/G 20/5   NL

AD-A156 030

DNA-TR-84-174

LASER TARGET DESIGN SCALING FOR THE UPGRADED NRL FACILITY

R.F. Stellingwerf
Mission Research Corporation
EM System Applications Division
1720 Randolph Road, SE
Albuquerque, NM 87106-4245

30 April 1984

Technical Report

CONTRACT No. DNA 001-82-C-0120

DTIC
ELECTE
S
JUN 2 6 1985
D
B

DTIC FILE COPY

Prepared for
Director
DEFENSE NUCLEAR AGENCY
Washington, DC 20305-1000

85
3

Destroy this report when it is no longer needed. Do not return
to sender.

REPORT DOCUMENTATION PAGE		READ INSTRUCTIONS BEFORE COMPLETING FORM
1. REPORT NUMBER DNA-TR-84-174	2. GOVT ACCESSION NO. AD·A156c39	3. RECIPIENT'S CATALOG NUMBER
4. TITLE (and Subtitle) LASER TARGET DESIGN SCALING FOR THE UPGRADED NRL FACILITY		5. TYPE OF REPORT & PERIOD COVERED Technical Report
		6. PERFORMING ORG. REPORT NUMBER AMRC-R-486
7. AUTHOR(s) R. F. Stellingwerf		8. CONTRACT OR GRANT NUMBER(s) DNA 001-82-C-0120
9. PERFORMING ORGANIZATION NAME AND ADDRESS Mission Research Corporation 1720 Randolph Road, SE Albuquerque, NM 87106-4245		10. PROGRAM ELEMENT, PROJECT, TASK AREA & WORK UNIT NUMBERS Task I25BAXHX-00010
11. CONTROLLING OFFICE NAME AND ADDRESS Director Defense Nuclear Agency Washington, DC 20305-1000		12. REPORT DATE 30 April 1984
		13. NUMBER OF PAGES 114
14. MONITORING AGENCY NAME & ADDRESS(if different from Controlling Office)		15. SECURITY CLASS. (of this report) UNCLASSIFIED
		15a. DECLASSIFICATION DOWNGRADING SCHEDULE N/A since UNCLASSIFIED

16. DISTRIBUTION STATEMENT (of this Report)

Approved for public release; distribution is unlimited.

17. DISTRIBUTION STATEMENT (of the abstract entered in Block 20, if different from Report)

19. KEY WORDS (Continue on reverse side if necessary and identify by block number)

Laser Plasma
High Altitude Bursts
Numerical Fluid Dynamics
Plasma Physics

20. ABSTRACT (Continue on reverse side if necessary and identify by block number)

This report describes research undertaken by Mission Research Corporation during 1983-84 in support of the experimental effort to model effects of high altitude nuclear bursts using high power lasers. Hydrodynamic simulations of experiments at NRL are discussed; the appropriate scaling laws are derived for variation of all important experimental parameters.

DD FORM 1473 1 JAN 73   EDITION OF 1 NOV 65 IS OBSOLETE

Conversion factors for U.S. customary to metric (SI) units of measurement.

To Convert From	To	Multiply By
angstrom	meters (m)	$1.000\ 000 \times E -10$
atmosphere (normal)	kilo pascal (kPa)	$1.013\ 25 \times E +2$
bar	kilo pascal (kPa)	$1.000\ 000 \times E +2$
barn	meter^2 (m^2)	$1.000\ 000 \times E -28$
British thermal unit (thermochemical)	joule (J)	$1.054\ 350 \times E +3$
cal (thermochemical)/cm^2§	mega joule/m^2 (MJ/m^2)	$4.184\ 000 \times E -2$
calorie (thermochemical)§	joule (J)	$4.184\ 000$
calorie (thermochemical)/g§	joule per kilogram (J/kg)*	$4.184\ 000 \times E +3$
curie§	giga becquerel (GBq)$^\perp$	$3.700\ 000 \times E +1$
degree Celsius‡	degree kelvin (K)	$t_K = t°_C + 273.15$
degree (angle)	radian (rad)	$1.745\ 329 \times E -2$
degree Fahrenheit	degree kelvin (K)	$t_K = (t°_F + 459.67)/1.8$
electron volt§	joule (J)	$1.602\ 19 \times E -19$
erg§	joule (J)	$1.000\ 000 \times E -7$
erg/second	watt (W)	$1.000\ 000 \times E -7$
foot	meter (m)	$3.048\ 000 \times E -1$
foot-pound-force	joule (J)	$1.355\ 818$
gallon (U.S. liquid)	meter^3 (m^3)	$3.785\ 412 \times E -3$
inch	meter (m)	$2.540\ 000 \times E -2$
jerk	joule (J)	$1.000\ 000 \times E +9$
joule/kilogram (J/kg) (radiation dose absorbed)§	gray (Gy)*	$1.000\ 000$
kilotons§	terajoules	4.183
kip (1000 lbf)	newton (N)	$4.448\ 222 \times E +3$
kip/inch^2 (ksi)	kilo pascal (kPa)	$6.894\ 757 \times E +3$
ktap	newton-second/m^2 (N-s/m^2)	$1.000\ 000 \times E +2$
micron	meter (m)	$1.000\ 000 \times E -6$
mil	meter (m)	$2.540\ 000 \times E -5$
mile (international)	meter (m)	$1.609\ 344 \times E +3$
ounce	kilogram (kg)	$2.834\ 952 \times E -2$
pound-force (lbf avoirdupois)	newton (N)	$4.448\ 222$
pound-force inch	newton-meter (N·m)	$1.129\ 848 \times E -1$
pound-force/inch	newton/meter (N/m)	$1.751\ 268 \times E +2$
pound-force/foot^2	kilo pascal (kPa)	$4.788\ 026 \times E -2$
pound-force/inch^2 (psi)	kilo pascal (kPa)	$6.894\ 757$
pound-mass (lbm avoirdupois)	kilogram (kg)	$4.535\ 924 \times E -1$
pound-mass-foot^2 (moment of inertia)	kilogram-meter^2 (kg·m^2)	$4.214\ 011 \times E -2$
pound-mass/foot^3	kilogram-meter^3 (kg/m^3)	$1.601\ 846 \times E +1$
rad (radiation dose absorbed)§	gray (Gy)*	$1.000\ 000 \times E -2$
roentgen§	coulomb/kilogram (C/kg)	$2.579\ 760 \times E -4$
shake	second (s)	$1.000\ 000 \times E -8$
slug	kilogram (kg)	$1.459\ 390 \times E +1$
torr (mm Hg, 0° C)	kilo pascal (kPa)	$1.333\ 22 \times E -1$

*The gray (Gy) is the accepted SI unit equivalent to the energy imparted by ionizing radiation to a mass of energy corresponding to one joule/kilogram.
-The becquerel (Bq) is the SI unit of radioactivity; 1 Bq = 1 event/s.
‡Temperature may be reported in degree Celsius as well as degree kelvin.
§These units should not be converted in DNA technical reports; however, a parenthetical conversion is permitted at the author's discretion.

TABLE OF CONTENTS

TABLE OF CONTENTS (Concluded)

LIST OF ILLUSTRATIONS

LIST OF ILLUSTRATIONS (Continued)

LIST OF ILLUSTRATIONS (Concluded)

6

LIST OF TABLES

8

SECTION 1

INTRODUCTION AND SUMMARY

1-1 INTRODUCTION.

In anticipation of a much wider range of parameters to be made available in the projected upgrade of the NRL laser facility, we undertake here a comprehensive study of target design options with particular emphasis upon application to HANE modeling.

The approach in this study will build upon previous work,[1] but will vary somewhat in design: we adopt here a "standard model" (called model "U0") with the following parameters:

Geometry = disk target, single-sided illumination,
Laser Energy = 1.5 kJ,
Wavelength = 1.06 microns,
Pulse length = 3.4 ns,
Target material = aluminum (Z = 13),
Target (disk) radius = 290 microns (0.0290 cm),
Maximum Absorbed Laser Intensity = 1.28×10^{14} W/cm^2.

Further details of this model are given in Section 2-4. Sequences of models will be constructed, all of which include the standard model but vary a specific parameter. In this way, detailed information about the effect of the variable parameter on the plasma expansion is obtained. The parameters to be varied are

1. Laser energy,
2. Laser intensity,
3. Flow divergence (geometry),
4. Wavelength,

SECTION 3

LASER ENERGY EFFECTS

In this section we discuss the effects of varying the laser
energy while maintaining the other parameters, including intensity, fixed.
A sequence of models has been designed in which larger targets are used at
larger energies, thus eliminating the strong physical variations that
depend on intensity. The remaining variations, discussed below, are con-
sequences of larger debris mass and energy, as well as the geometric con-
sequences of a more nearly plane-parallel expansion.

3-1   MODELS IN SEQUENCE U1.

A series of five models has been run with laser energies of
23 J, 187 J, 0.5 kJ, 1.5 kJ and 5 kJ. Model U1-4 is the standard model
U0. Model parameters were obtained from equations 2-6 and are listed in
Table 3-1. Laser energy, peak power and target radius is given for each
model for both the disk and the spherical interpretations.

Table 3-2 lists the input parameters and the results for these
models; specific details are discussed below.

3-2   RADIUS, DENSITY AND ABSORPTION EFFECTS.

One consequence of maintaining a fixed angle of divergence (edge
effects) while irradiating larger and larger targets is a plasma flow that
is more nearly plane-parallel in nature, as shown schematically in Figure
3-1. This is also clearly seen in Figure 3-2, which is a log-log plot of
the initial radius, critical radius at 7 ns, and outer radius at 7 ns. The
outer radius remains relatively constant, while the (spherical) target
radius and critical surface radius increase with increasing laser energy to

TABLE 2-1.

NRL Laser Upgrade-Model U0

Run number	U0
E laser (d)	1.5 kJ
Wavelength	1.06 μm
Pulse length	3.4 ns
Target Z	13
Radius (d)	0.0290 cm
Divergence	80 deg
Mult factor	8.55
Intensity-ab	1.28E14 W/cm^2
Absorption	0.90
KE fraction	0.69
RE fraction	0.13
Corona Mass	2.29E-6 g
U(ion peak)	0.91 (8) cm/s
U max	1.37 (8) cm/s
Delta U/U	0.38
R crit	0.0385 cm
R outer	0.5770 cm
T max	1.26 keV
T outer	0.75 keV
ρ outer	3.76E-7 g/cm^3

2-5   MODEL-UO.

The full set of parameters for the benchmark model are listed in
Table 2-1. Input parameters are above the horizontal line, output parame-
ters at time = 7 ns, appear below. At 7 ns, for FWHM = 3.4 ns, roughly 90%
of laser energy has been delivered. "KE fraction" is the fraction of total
model energy in kinetic energy; "RE fraction" is the ratio of the total
radiated energy to the total model energy; "U (ion peak)" is the velocity
at the dN/dU peak - this is the velocity of the greatest number of ions
(units of 10^8 cm/sec); "delta U/U" is the width of the dN/dU distribution;
"T_{max}" is the maximum coronal electron temperature (keV) - achieved near
the critical surface; and "T_{outer}" is the electron temperature at the
outer edge of the debris. Ion temperatures are generally much lower in the
outer debris region.

We see that velocities of about 10^8 cm/sec are achieved in this
model, with a fairly broad ($\Delta U/U$ = 38%) spread. The total absorption found
here is 90% - higher than that found in lower energy models. This is due
to a longer density scale length in the corona and will be discussed in
Section 3-2. Of this energy, 13% is radiated (this number is somewhat
uncertain due to the approximate treatment of radiation in the corona), and
69% of the remainder is found in ion kinetic energy.

Other model parameters are then calculated from equations 2-1 - 2-5 to obtain:

$$MULT = 2/(1 - \cos(\theta_{DIV}/2)) \quad ,$$

$$\text{Laser energy on sphere} = E_s = MULT \times E_d \text{ (kJ)},$$

$$\text{Laser power on sphere} = P_s = 2.568 \times 10^{11} E_s (3.4/FWHM) \text{ (Watts)},$$

$$\text{Laser power on disk} = P_d = P_s/MULT \text{ (Watts)}, \tag{2-6}$$

$$\text{Disk target radius} = R_d = 0.024 \left[E_d \left(\frac{\alpha_{INT}}{0.7} \right) \left(\frac{I_a}{10^{14}} \right)^{-1} \left(\frac{FWHM}{3.4} \right)^{-1} \text{ (cm)} \right]^{\frac{1}{2}} ,$$

$$\text{Spherical target radius} = R_s = (MULT)^{1/2} R_d/2 \quad .$$

Note that α_{INT} is treated as an input quantity but in reality is a model result. A rough estimate of this quantity is used in model design and, in most cases, some variation in the final model results, primarily the intensity, is accepted.

2-3 LASER INTENSITY.

Of primary importance to the present study is a measure of the laser energy deposited in the target material per unit area. To this purpose, we define an effective "absorbed maximum laser intensity," I_a, in the following way:

$$I_a = \left(\frac{P_{max}}{\text{target area}}\right) \times \alpha_{INT} \quad , \quad (2-5)$$

where α_{INT} is the time-integrated laser energy absorption fraction. Here we use the initial target area to obtain I_a, rather than the actual area at the time at which P_{max} is achieved (as done in Reference 1). This is only an estimate of the true laser energy deposition, but one that is commonly used. Since α_{INT} is a derived parameter, I_a is also. In practice, we estimate α_{INT} expected for a given model, specify a desired I_a, and thereby obtain the required target size using equation 2-5. The value of I_a actually obtained will vary somewhat from the desired value.

Of course, I_a represents a maximum value of the time varying laser deposition. The mean value will be roughly $I_a/2$.

2-4 SUMMARY OF MODEL RELATIONS.

Here we summarize the relations between the spherical and disk target input parameters. Normal input quantities are

1. Laser energy on disk target, E_d, (kJ),
2. Laser intensity, I_a, (Watts/cm^2),
3. Integrated absorption estimate, α_{INT},
4. Pulse FWHM, (ns),

and

5. Flow divergence angle, θ_{DIV}, (degrees).

19

$$MULT = \frac{\text{Sphere Area}}{\text{Sector Area}} = \frac{2}{1 - \cos(\theta_{DIV}/2)} . \qquad (2-1)$$

The relation connecting the sphere radius and the disk radius in Figure 2-1 is obtained by requiring that the disk area be equal to the area of the sphere sector being modeled. We obtain,

$$\text{Sector Area} = 2\pi(1 - \cos(\theta_{DIV}/2))R_S^2 = \pi R_d^2 ,$$

or,

$$R_d = R_S[2(1 - \cos(\theta_{DIV}/2)]^{1/2}$$

$$= R_S \frac{2}{\sqrt{MULT}} . \qquad (2-2)$$

where R_S is the sphere radius, and R_d is the disk radius. All targets in this survey will have a shell thickness of 25 microns. This is sufficiently thick to prevent premature void closure.

2-2   PULSE SHAPE.

We use here an exponential pulse shape that is a generalization of the shape previously used.[1] Here we include a time stretching factor to allow variation of the pulse length. The formula is

$$\frac{P}{P_{max}} = 0.9103 \left(e^{-0.75 \tau + 2} + e^{0.3\tau - 1.7} \right)^{2.3} - 0.00865 ,$$

where

$$\tau = t \left(\frac{3.4 \text{ ns}}{\text{FWHM}} \right) , \qquad (2-3)$$

P = power, t = time, and FWHM = full width at half maximum, both in nanoseconds. Pulse shapes for three values of FWHM are shown in Figure 2-2. P_{max} is the maximum laser power, given by

$$P_{max} = 2.568 \times 10^{11} E_L(kJ) \left(\frac{3.4}{\text{FWHM}} \right) \quad \text{Watts} , \qquad (2-4)$$

where E_L is the laser energy.

18
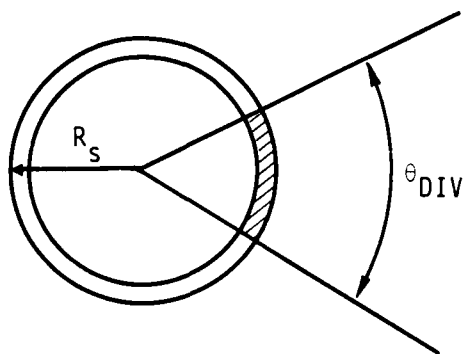
Figure 2-1. Spherical and disk target model.

Time (ns)
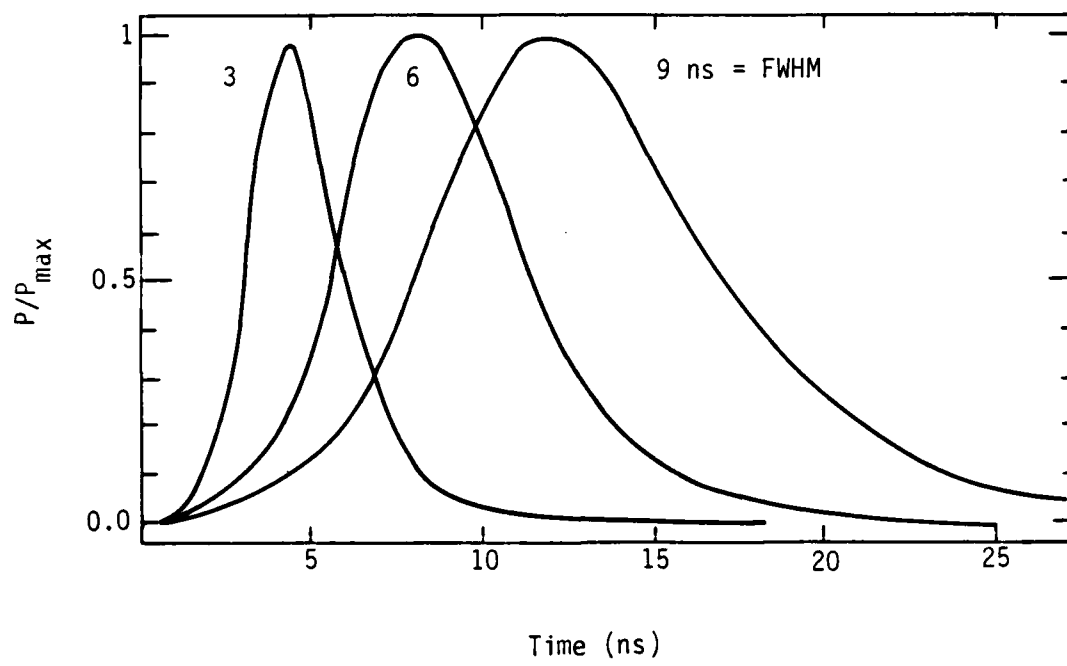
Figure 2-2. Exponential pulse shapes.

SECTION 2

MODEL DESIGN

In this section, the basic model construction technique is presented. Physical assumptions and derivations in the hydrodynamic simulation code (MACH1) have been discussed previously,[1] and will not be repeated in detail. The code employs a three-temperature scheme: electron, hot electron and ion temperatures. A multigroup local radiation treatment is used. Absorption physics is described in Reference 1, inverse bremsstrahlung is the primary mechanism with the efficiency factor taken to be 0.5 for all present models - this is the "Langdon factor"[2] predicted by kinetic theory to be near 0.446[3] and shown to be consistent with experiment in Reference 1. At the critical surface, 30% of the light penetrating to this level is assumed to be absorbed by collective processes.

2-1   FLOW DIVERGENCE - SPHERICAL VERSUS FLAT TARGETS.

The laser targets modeled here are flat targets with single-sided illumination. Experimentally, such targets produce a diverging flow of plasma with a total divergence angle of about 80 degrees. This configuration can be adequately represented by a one-dimensional hydrodynamic simulation using a spherical model, as shown in Figure 2-1, in which the diverging flow within a sector approximates the disk target case. Normally, the angle of divergence, θ_{DIV} is taken to be 80°, but this angle can be varied to represent different experimental conditions. For example, an expansion produced by double-sided illumination should be essentially spherical, and we take $\theta_{DIV} = 360°$. The laser energy delivered to the sphere is greater than the energy on the equivalent flat target by the multiplication factor:

16

These relations and the others given in each section of this report should assist in the design of laser targets for specific HANE applications.

4. Electron/ion coupling is stronger, and

5. Ion velocity distribution width is slightly narrower.

These secondary effects are weaker in the energy range near 1.5 KJ than in the range near 200 J laser pulses.

1-2.7   Low Energy Models.

A sequence of models with laser energy of 23 J was also computed to compare with the "high pressure" NRL experiments carried out in 1983/84. Only five models were computed with various combinations of intensity and target material. A detailed comparison of the predicted charge-cup current with two experimental shots shows very good agreement.

1-2.8   Multivariate Scaling.

Multiple regression analysis has been performed on the set of all of the "upgrade" models in this report. The scaling relations obtained in this way include the following:

1. Laser absorption $\propto I^{-.1}\lambda^{-.25} FW^{.1}$,

2. Ion velocity $\propto I^{.3}\lambda^{.2} FW^{.5}$,

3. Ion velocity spread $\propto E^{.4}\lambda^{1} FW^{-1}$,

4. Outer temperature $\propto I^{.5} E^{.3}\lambda^{1} FW^{1.5}$.

Here I is the absorbed laser intensity, E the laser energy, λ the laser wavelength, and FW the laser pulse length.

1-2.5   Laser Pulse Length Effects.

The most important effects seen as a result of varying the laser pulse length are:

1. The character of the flow changes strongly from that of an isothermal rarefaction expansion (with a linear increase of the velocity with radius) in the case of a short pulse (1 ns or less), to that of a steady-state (wind) flow solution (with a logarithmic variation of the velocity with radius) for the long pulse case (few ns or longer). This in turn produces a very broad spread in the velocity distribution for the short pulse case.

2. We find a very strong increase in the coronal temperature as the laser pulse length is increased. This is in part due to larger radiative losses for short pulses.

3. Laser absorption increases for longer pulses, roughly as $\alpha \propto FWHM^{0.1}$, where FWHM is the laser pulse length.

1-2.6   Target Material Effects.

The primary effect of increasing target Z is:

1. Radiative energy losses increase from 2% of the absorbed energy at $Z = 4$ to 41% at $Z = 26$.

This induces the following secondary effects:

2. Coronal mass decreases,

3. Outer temperatures and velocities decrease, outer density increases,

2. Higher density and temperature gradients than in the flat target case, resulting in somewhat reduced absorption.

3. Decreased ion velocity, but only mildly, to about 8.5×10^7 cm/sec for the standard case.

4. A strong resemblance to lower power plasma expansion with lower flow divergence.

1-2.4   Laser Wavelength Effects.

Three sequences of models have been computed with different assumptions on how the wavelength is varied, the conclusions are:

1. If the laser wavelenath is varied with all other parameters held fixed, the increase in coronal velocity with increasing wavelenqth is weaker than expected from simple scaling arguments. The reason for this is the change in coronal structure caused by larger temperature gradients at shorter wavelengths.

2. If the laser wavelength is varied with $I\lambda^2$ held fixed, then the models actually predict larger coronal velocities for the shorter wavelength shots.

3. In all cases we find narrower velocity distributions at shorter wavelengths, a desirable feature for HANE simulations.

4. These models confirm that excellent absorption efficiency should be obtained at shorter wavelengths.

efficiency of laser energy to ion kinetic energy peaks near
laser energy of 1.5 KJ.

3. Ion velocity at the dN/dU peak is largest at $E_1 = 1.5$ KJ,
reaching a value of 9×10^7 cm/sec for $I = 10^{14}$ W/cm^2.

1-2.2   Laser Intensity Effects.

Models have been computed with intensity ranging from 10^{12} to
10^{16} W/cm^2. The main conclusions drawn from this sequence are:

1. The plasma temperatures in the corona and near the critical
surface scale as absorbed intensity to the 0.26 - 0.31
power. This is the dependence expected from classical laser
deposition and thermal conductivity.

2. Coronal ion velocities depend strongly on intensity ($U \propto$
$I^{0.25}$) and range from 2×10^7 to 2×10^8 cm/sec as inten-
sity is varied.

3. The ion velocity distribution width decreases at higher
intensities, probably indicating incipient shock formation.

1-2.3   Flow Divergence Effects.

Models with varying angle of coronal flow divergence show that,
as flow symmetry is increased toward a spherical configuration, the
following effects can be expected:

1. A much narrower distribution of ion velocities than in the
flat target case, leading to early shock formation.

5. Pulse length,

and

6. Target material.

Of primary concern among the dependent variables are absorption and energy balance, coronal (debris) velocity structure, coronal scale lengths, and coronal temperature structure.

An additional sequence of models with laser energy = 23 J, similar to current low power experiments, is also included for comparison purposes.

Note that in sections with many tables and figures, these items are grouped at the end of the section to avoid lengthy breaks in the text.

1-2   SUMMARY OF PRINCIPAL RESULTS.

1-2.1   Laser Energy Effects.

A sequence of models were computed with varying laser energy, while maintaining all other parameters, including laser intensity, constant (the laser spot size was varied to achieve constant intensity). The primary effect found in this sequence that breaks the simple mass/energy scaling is that of flow geometry: high energy laser pulses on larger targets produce a plasma flow that is more nearly plane parallel in nature. The consequences of this are:

1. Temperature and density gradients are smaller at higher energies.

2. Integrated laser absorption is higher, while kinetic energy fraction if lower at high energies. Overall conversion

maintain constant intensity. This, taken together with the flow divergence, results in a much lower density corona for the low energy models: outer density of 5 x 10^{-8} g/cm^3 for model U1-1 versus 2 x 10^{-6} g/cm^3 for model U1-5, as shown in Figure 3-3. Higher outer density at higher energy in turn produces a larger absorption fraction, plotted as α_{INT} in Figure 3-4, increasing from 60% to 93% at 5 kJ. On the other hand, the moderation of the density gradient reduces the pressure acceleration somewhat and thus reduces the kinetic energy fraction, also shown in Figure 3-4. A measure of the actual change in kinetic energy is the product KE fraction x α_{INT}. This quantity, as shown by the dashed line in Figure 3-4, peaks near E_L = 1.5 kJ where its value is about 35% higher than at low energy.

Figure 3-5 shows the variation of the coronal mass at 7 ns. As expected, $M \propto E_L$.

The scaling laws for all quantities, as derived by a linear least-squares fit in the log-log plane, are summarized in Table 3-3. We find:

$$R_{crit} \propto E_L^{0.5} , \qquad (3-1)$$

while

$$R_{outer} \propto E_L^{0.1} , \qquad (3-2)$$

resulting in

$$\rho_{outer} \propto E_L^{0.7} . \qquad (3-3)$$

The absorption scales as

$$\alpha_{INT} \propto E_L^{0.1} , \qquad (3-4)$$

while

$$KEF \propto E_L^{-0.4} , \qquad (3-5)$$

and

$$\text{corona mass} \propto E_L^{1.0} . \qquad (3-4)$$

Table 3-3 also shows confidence intervals based on the five models, and correlation coefficients in the log-log fit.

3-3   VELOCITY AND TEMPERATURE EFFECTS.

The variation of the maximum electron temperature (achieved near
the critical surface) and the outer electron temperature for the models at
7 ns is shown in Figure 3-6. Two trends are apparent. First, higher
coronal temperatures are attained at larger laser energies. This is a con-
sequence of increasing α_{INT} and decreasing KE fraction (Figure 3-4).
Second, the outer temperature approaches nearer to T_{max} at higher ener-
gies. This trend is consistent with the more nearly plane-parallel nature
of the flow at higher energies, causing shallower gradients.

The increasing trend in electron temperature is reflected in an
increase in the maximum coronal velocity (the "fast ion velocity," shown in
Figure 3-7 as U_{max}). This velocity is very nearly five times the coronal
sound speed, as predicted by a steady flow picture of coronal expansion.[1]

Also shown in Figure 3-7 is the variation of the velocity at the
peak of the dN/dU ion number distribution (U_i). This velocity is closely
related to the conversion efficiency of laser energy to kinetic energy
(dashed line in Figure 3-4), and peaks in the vicinity of the 1.5 kJ model.

Finally, Figure 3-8 shows the dependence of the width of the
velocity distribution on laser energy. A narrow distribution implies that
the debris ions are nearly monoenergetic, a desirable feature from a diag-
nostic point of view. We see here a rather strong variation in this quan-
tity, with broader distribution functions at higher energies. This trend
is illustrated in more detail in Figure 3-9, in which velocity versus
radius and dN/dU versus velocity are shown for models U1-1, U1-3 and U1-5.
The behavior seen here is caused by divergent expansion at low energies
causing the outer corona to cool and a shock structure to form in models
U1-1 and U1-2 as faster moving inner material overtakes the cool outer

layers. For the higher energy models, however, the flow is less divergent, the corona more nearly isothermal, and the outer layers begin to approach the linear increase of an isothermal rarefaction wave.

Table 3-3 gives the scaling parameters for the above quantities. We have

$$T_{max} \propto E_L^{0.2} \quad , \tag{3-7}$$

while

$$T_{outer} \propto E_L^{0.35} \quad . \tag{3-8}$$

For the velocities, we see that

$$U_i \propto E_L^{0.04} \quad , \tag{3-9}$$

and

$$U_{max} \propto E_L^{0.1} \quad , \tag{3-10}$$

following the square root of T_{max}. A stronger relation is seen in the width of the distribution:

$$\Delta U/U \propto E_L^{0.5} \quad . \tag{3-11}$$

3-4   SUMMARY OF LASER ENERGY EFFECTS.

We have presented a series of models of disk targets in vacuum irradiated by laser pulses of fixed shape, duration and intensity, but of varying total energy and target radius. The primary effect found in this sequence that breaks the simple mass/energy scaling is that of flow geometry: high energy laser pulses on larger targets produce a plasma flow that is more nearly plane parallel in nature. The consequences of this are:

1. Temperature and density gradients are smaller at higher energies.

2. Integrated laser absorption is higher, while kinetic energy fraction is lower at higher energies. Overall conversion efficiency of laser energy to ion kinetic energy peaks near laser energy of 1.5 kJ.

3. Ion velocity at the dN/dU peak is largest at $E_L \approx 1.5$ kJ, reaching a value of 9×10^7 cm/sec for $I \approx 10^{14}$ W/cm^2.

4. The width of the velocity distribution increases strongly at higher energies, due to a more nearly isothermal expansion.

TABLE 3-1.

Parameters for Sequence U1: Laser Energy Variation

Model #	E disk	R disk	P disk	E sphere	R sphere	P sphere
U1-1	0.023	0.0041	5.9E09	0.20	0.0060	5.1E10
U1-2	0.187	0.0096	4.8E10	1.60	0.0140	4.1E11
U1-3	0.500	0.0181	1.3E11	4.27	0.0265	1.1E12
U1-4	1.500	0.0290	3.9E11	12.8	0.0430	3.3E12
U1-5	5.000	0.0625	1.3E12	42.7	0.0914	1.1E13

TABLE 3-2.

Model Results for Sequence U1

	-1-	-2-	-3-	-4-	-5-
Run number	U1-1	U1-2	U1-3	U1-4	U1-5
*E laser (d)	0.023	0.187	0.500	1.500 kJ	5.000
Wavelength	1.06	1.06	1.06	1.06 μm	1.06
Pulse length	3.4	3.4	3.4	3.4 ns	3.4
Target Z	13	13	13	13	13
*Radius (d)	0.0041	0.0096	0.0181	0.0290 cm	0.0625
Divergence	80	80	80	80 deg	80
Intensity-ab	6.70E13	1.20E14	1.06E14	1.28E14 W/cm^2	9.77E13
Absorption	0.59	0.72	0.85	0.90	0.93
KE fraction	0.77	0.76	0.71	0.69	0.62
RE fraction	0.13	0.13	0.13	0.13	0.14
Corona Mass	4.60E-8	2.79E-7	8.39E-7	2.29E-6 g	8.07E-6
U(ion peak)	0.69	0.85	0.88	0.91 (8) cm/s	0.82
U max	0.81	1.16	1.23	1.37 (8) cm/s	1.37
Delta U/U	0.09	0.13	0.28	0.38	0.96
R crit	0.0071	0.0191	0.0207	0.0385 cm	0.0945
R outer	0.3567	0.5010	0.5150	0.5770 cm	0.5978
T max	0.52	0.69	1.06	1.26 keV	1.35
T outer	0.16	0.32	0.49	0.75 keV	0.99
Rho outer	3.78E-8	6.35E-8	2.00E-7	3.76E-7 g/cm^3	1.51E-6

*Varied Quantities

TABLE 3-3.

Sequence U1: Power Law Scale Factors

$$Q = \alpha \, E_L^{\beta}, \; r = \text{correlation coefficient (log)}$$

Quantity	α	β	r
Absorption*	0.847 ± .04	0.09 ± .01	0.97
KE fraction*	0.685 ± .03	-0.393 ± .009	-0.93
RE fraction	0.133 ± .004	0.01 ± .007	0.66
Corona Mass (g)	1.6E-6 ± 2E-7	0.963 ± .02	1.00
U (ion peak)/10^8*	0.852 ± .08	0.036 ± .02	0.69
$U_{max}/10^8$*	1.27 ± .1	0.099 ± .02	0.94
$\Delta U/U$	0.37 ± .1	0.437 ± .07	0.96
R_{crit}	0.0367 ± .008	0.455 ± .05	0.98
R_{outer}	0.543 ± .04	0.095 ± .02	0.96
T_{max} (kev)*	1.08 ± .1	0.193 ± .03	0.97
T_{outer} (kev)*	0.602 ± .04	0.350 ± .02	1.00
ρ_{outer}*	3.4E-7 ± 2E-7	0.69 ± .1	0.96

*These quantities show curvature in their logarithmic dependence on E_L.
 See Table 3-2 and figures for the nature of the relation.

Divergent Flow
for Low Energy
Small Target
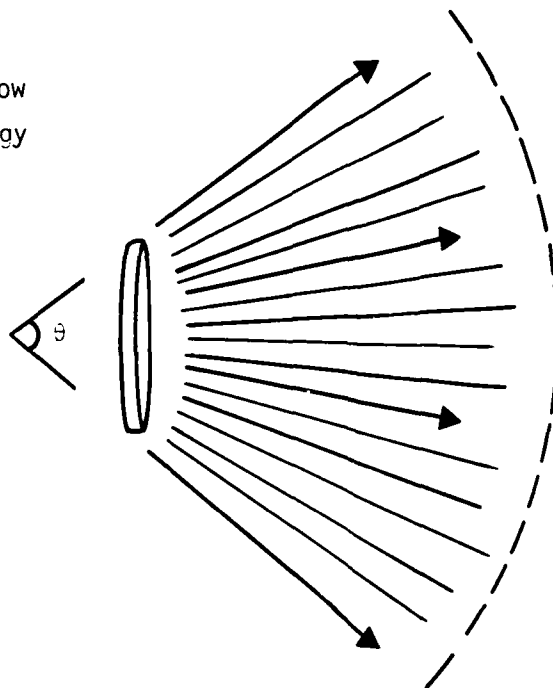
Divergent Flow
for High Energy
Large Target
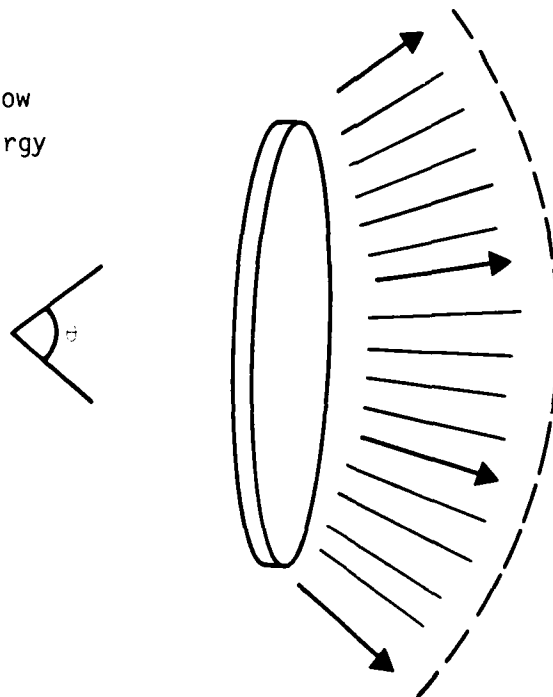
Figure 3-1. Divergent flow from disk targets of varying size at
constant intensity.
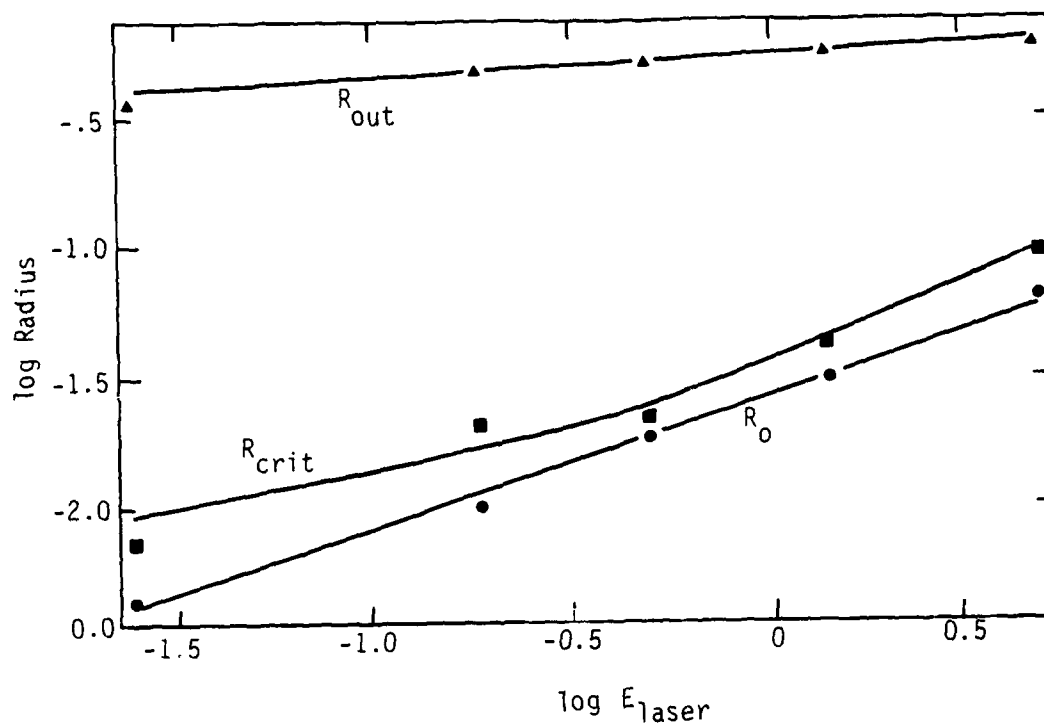
Figure 3-2. Target radii versus laser energy.
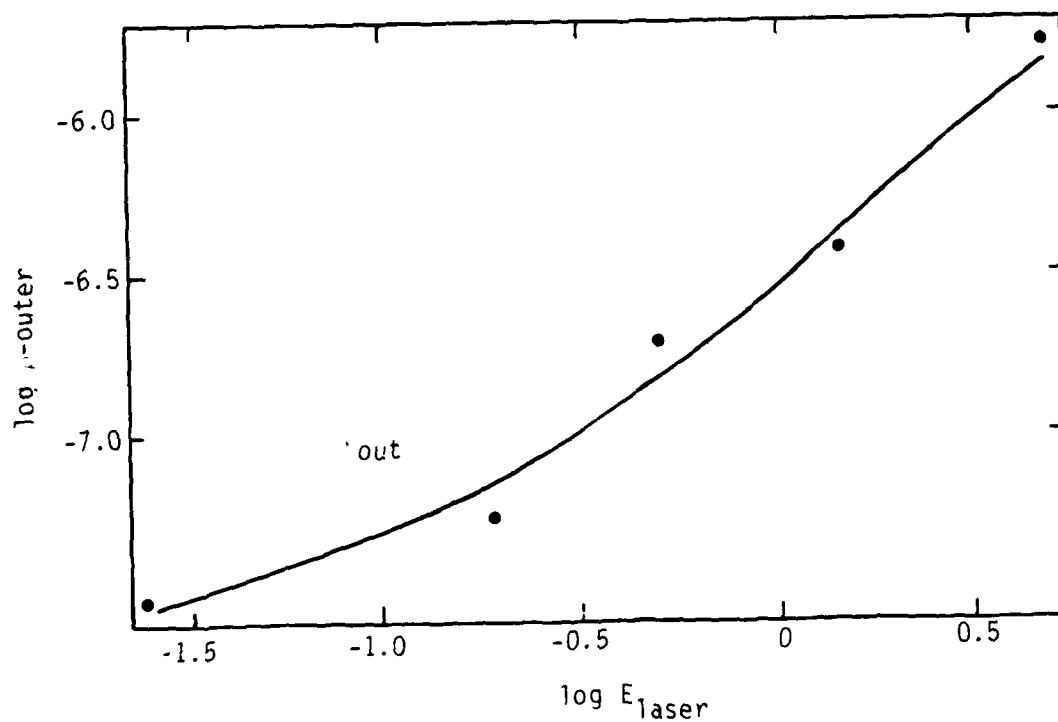
Figure 3-3. Outer coronal density versus laser energy.

31
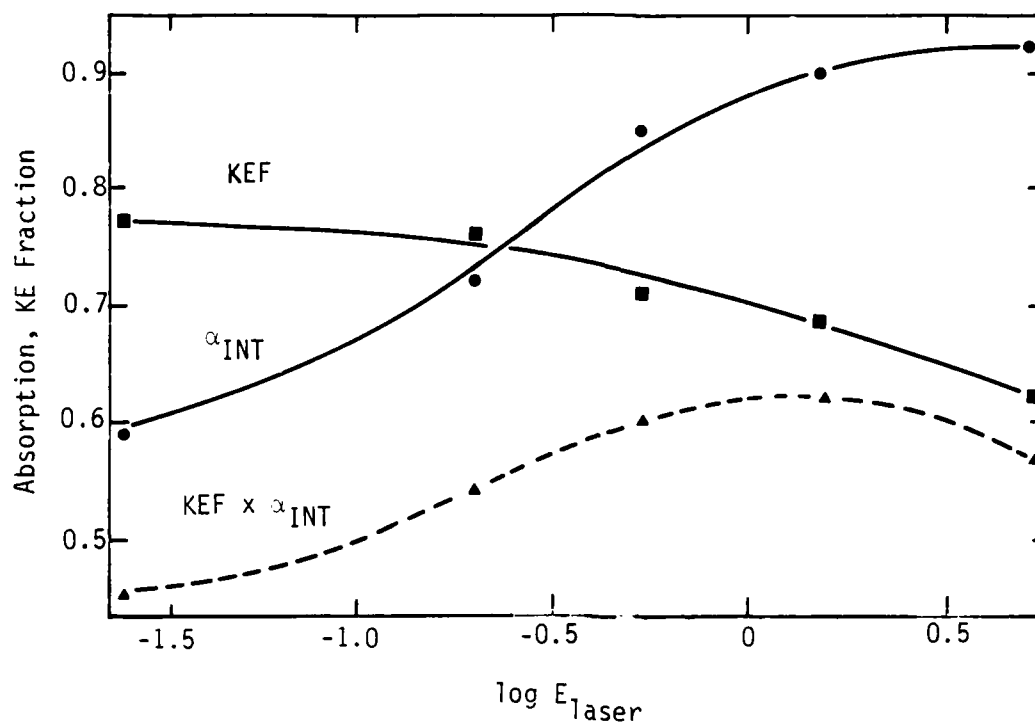
Figure 3-4. Absorption and KE fractions versus laser energy.
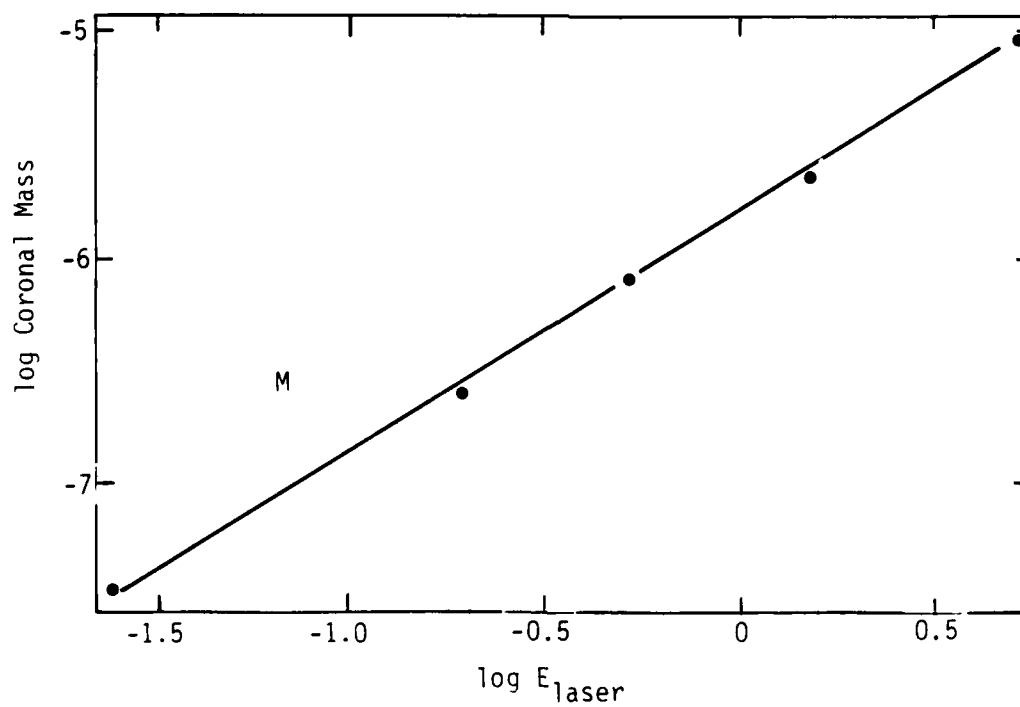
Figure 3-5. Coronal mass versus laser energy.
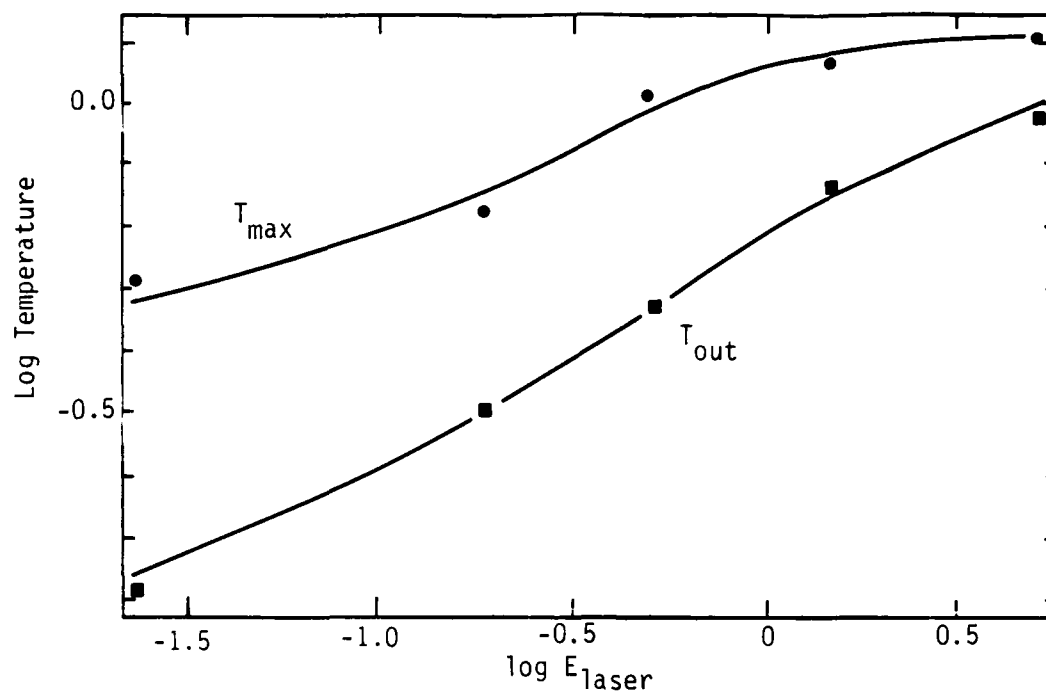
Figure 3-6. Coronal temperature versus laser energy.
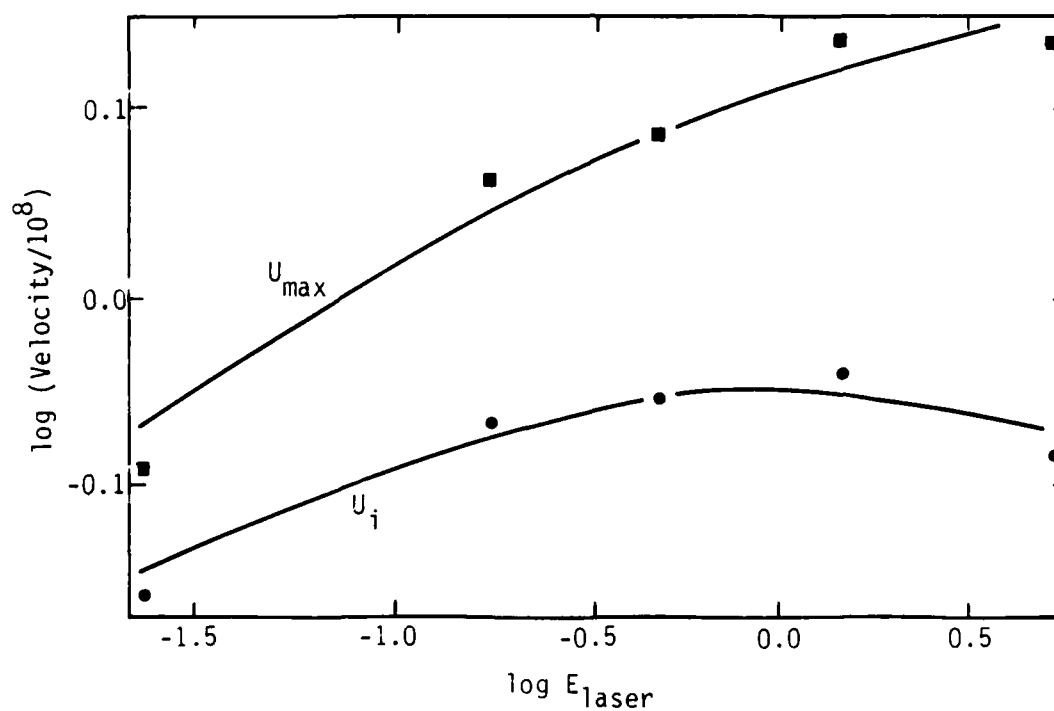
Figure 3-7. Fast ion velocity (U_{max}) and velocity at the peak of the ion distribution function (U_i) versus laser energy.
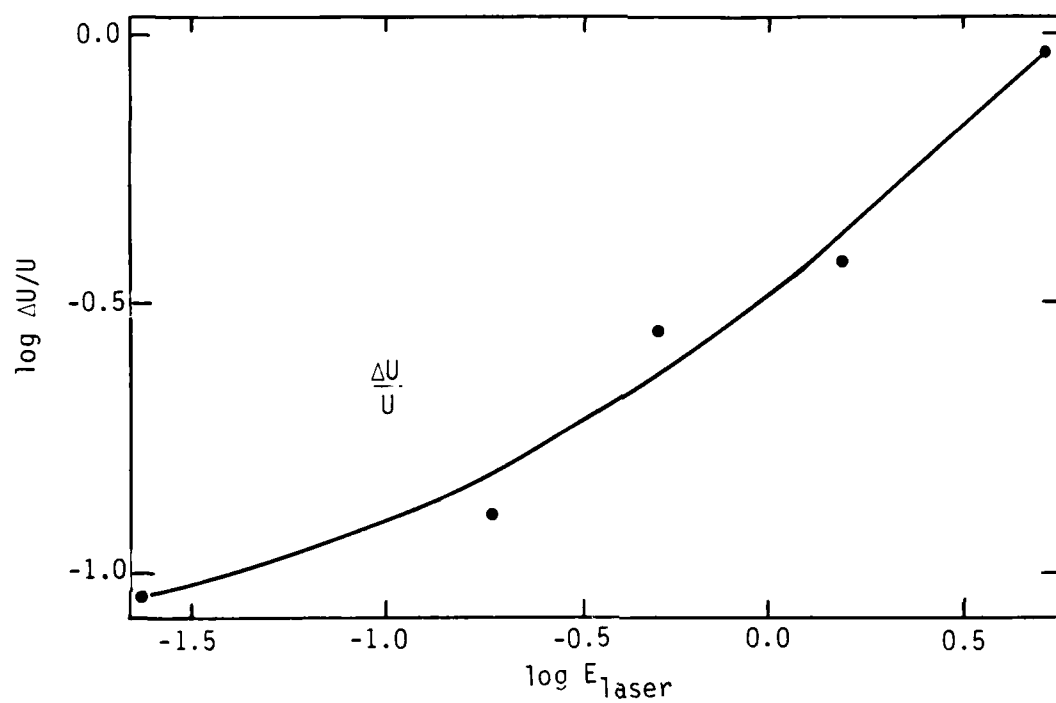
Figure 3-8.   Width of the ion velocity distribution function
versus laser energy.
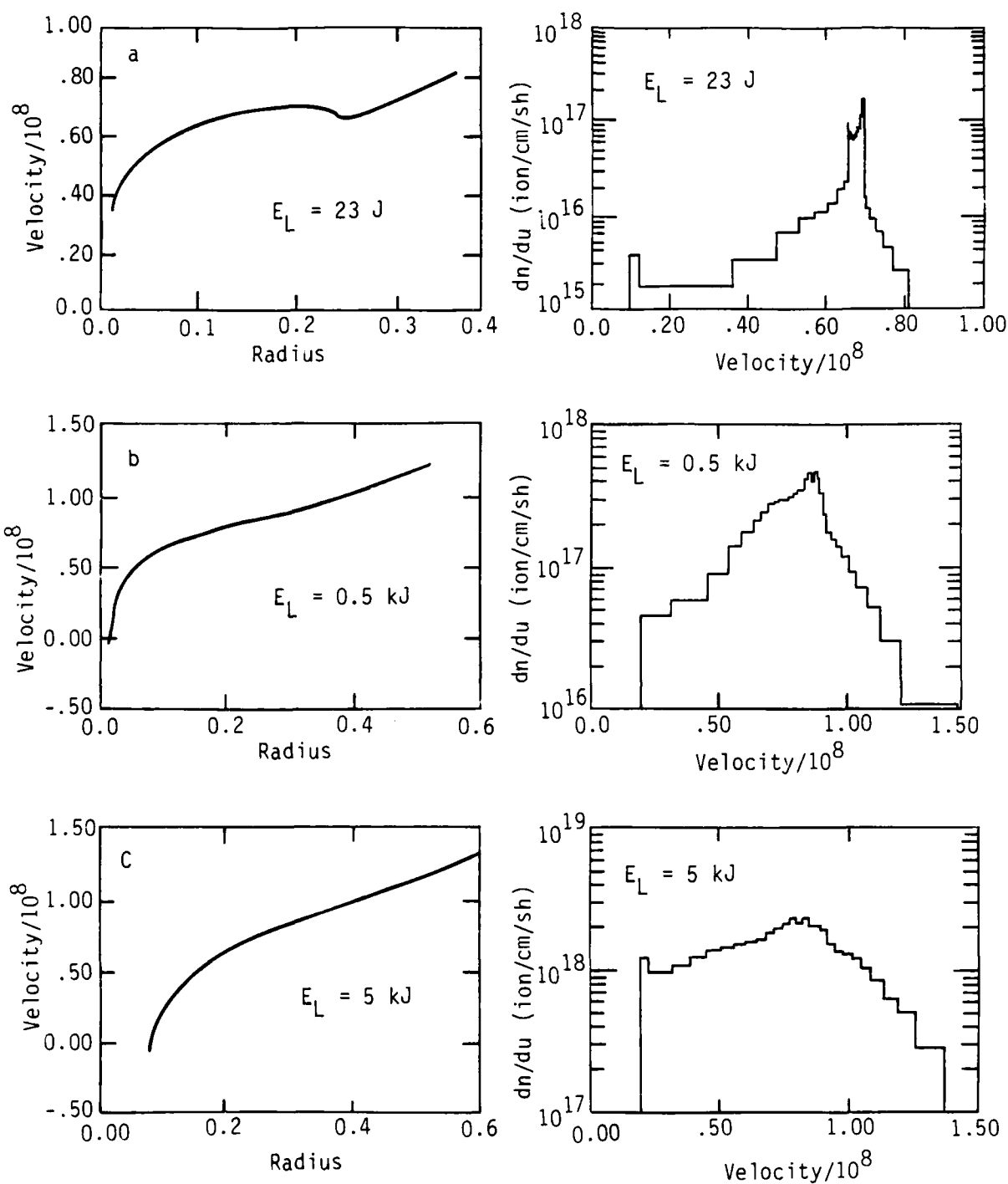
Figure 3-9. Comparison of velocity distributions for three laser energies.

SECTION 4

LASER INTENSITY EFFECTS

In this section we discuss the effects of varying the laser wave-length over the range 10^{12} W/cm^2 to 10^{16} W/cm^2. Laser energy for all of these models (except the highest intensity model) was held fixed at 1.5 kJ, while the target radius was varied to achieve the desired intensity. This procedure is roughly equivalent to varying the laser spot size, a common experimental practice. All other target and laser parameters were taken to be the "model U0" values as discussed in Section 2. The precise definition of "laser intensity" used here is given in Section 2-3; it includes the effect of partial absorption of the laser light.

4-1 MODELS IN SEQUENCE 2.

A series of five models were computed with laser intensities of 10^{12}, 10^{13}, 10^{14}, 8.7×10^{14}, and 9.8×10^{15} W/cm^2. Model U2-3 is model U0. A full description of the model parameters and results is given in Tables 4-1 and 4-2, with the format as in previous sections. The model U2-5 (10^{16} W/cm^2) required special treatment, since with a laser energy of 1.5 kJ the spherical target radius needed for the simulation is only 36 microns and the resulting target mass is so low that the entire target becomes under-dense very early in the simulation. To avoid this, the model shown here uses a laser energy of 15 kJ, allowing a larger target at the desired intensity. One additional parameter was varied in these models: the shell thickness. This was taken to be 10, 25, 25 and 50 microns for models U2-1 -- U2-4, and model U2-5 is a solid sphere with radius 115 microns. This variation in target thickness is needed to maintain resolution in the computations with reasonable zoning. As in previous sections, the "disk" numbers in Tables 4-1 and 4-2 represent parameters pertaining to a flat target experiment, while the "sphere" numbers are those actually used in the

computation. These models can be compared to the sequence of low energy models discussed in Section 9, which also treat intensity as a parameter.

The results given in Table 4-2 are presented graphically in Figures 4-1 through 4-7, and power law scale factors are given in Table 4-3. Since model U2-5 is higher power case than the other models, its results do not conform to the normal pattern for some parameters. In Table 4-3 several regressions were done using only the first four models (as indicated) because the fifth case appeared somewhat abnormal. The regressions as given should be correct for a 1.5 kJ laser.

4-2   PHYSICAL PROCESSES.

Laser intensity represents the energy density of the deposited energy flux, and is the most important parameter affecting the coronal temperature, sound speed, and expansion velocity. In very simple terms, the temperature of the corona is determined through a balance of the deposition energy flux and the conduction flux that carries the energy to the bulk of the target. In the present models, the electron conductivity is given by:

$$\kappa = \frac{\kappa_0}{1 + \top T/(fn_e v_e)} \qquad (4-1)$$

where κ_0 is the classical "Spitzer" conductivity (see below), "f" is the flux-limit factor (taken to be equal to the classical value of 0.4 here), $v_e = (T_e/m_e)^{1/2}$ is the electron free-streaming velocity, and $u_e = n_e T_e$ is the electron energy density. The free-streaming limit to the flux is only important at high temperatures, and is discussed in detail below. Note that the common practice of drastically reducing the value of "f" in order to increase model temperatures has not been adopted in these models.

TABLE 5-1.

Sequence U3: Flow divergence variation.

Model No.	E disk	R disk	P disk	E sphere	R sphere	P sphere
U3-1	1.50	0.0333	3.9E11	42.7	0.0914	1.1E13
U3-2	1.50	0.0333	3.9E11	12.8	0.0430	3.3E12
U3-3	1.50	0.0333	3.9E11	4.27	0.0265	1.1E12
U3-4	1.50	0.0333	3.9E11	1.60	0.0140	3.9E11

TABLE 5-2.

Model results for sequence U3.

	-1-	-2-	-3-	-4-
Run number	U3-1	U3-2	U3-3	U3-4
E laser (d)	1.50	1.50 kJ	1.50	1.50
Wavelength	1.06	1.06 mic	1.06	1.06
Pulse Length	3.4	3.4 ns	3.4	3.4
Target Z	13	13	13	13
Radius (d)	0.0333	0.0333 cm	0.0333	0.0333
*Divergence	40	80 deg	145	360
Intensity-ab	9.77E13	1.28E14	1.06E14	1.20E14
Absorption	0.93	0.90	0.85	0.72
KE fraction	0.62	0.69	0.71	0.76
RE fraction	0.14	0.13	0.13	0.13
Corona Mass	2.42E-6	2.29E-6 g	2.52E-6	2.23E-6
U(ion peak)	0.82	0.91 (8)	0.88	0.85
U max	1.37	1.37 (8)	1.23	1.16
Delta U/U	0.96	0.38	0.28	0.13
R crit	0.0945	0.0385 cm	0.0207	0.0191
R outer	0.5978	0.5770 cm	0.5150	0.5010
T max	1.35	1.26 keV	1.06	0.69
T outer	0.99	0.75 keV	0.49	0.32
Rho outer	1.51E-6	3.76E-7 g/	2.00E-7	6.35E-8

*Varied Quantities

resulting velocities are plotted in Figure 5-5: the velocity at the ion
distribution peak reflects the decreased temperatures, but varies very
little over the sequence. Finally, the width of the velocity distribution
is shown in Figure 5-6. This quantity is strongly affected by the diver-
gence, and varies roughly as the inverse of the divergence angle.

The power law scale factors representing these variations are
given in Table 5-3. The most significant correlations are found for the
coronal density ($= \theta^{-1.4}$), δ U/U ($= \theta^{-0.9}$), the coronal temperatures ($=
\theta^{-0.5}$), and the critical surface radius ($= \theta^{-0.7}$). The coronal veloci-
ties, absorption, KE fraction and RE fraction show little variation across
the sequence.

5-3   SUMMARY OF FLOW DIVERGENCE EFFECTS.

We have shown that, as flow symmetry is increased toward a spher-
ical configuration, the following effects can be expected:

1. A much narrower distribution of ion velocities than in the
    flat target case.

2. Higher density and temperature gradients than in the flat
    target case, resulting in somewhat reduced absorption.

3. Decreased ion velocity, but only mildly, to about 8.5×10^7
    cm/sec for the standard case.

It is seen that, in comparison with Section 3, the effects asso-
ciated with a spherical flow geometry generally just cancel the effects of
increasing the laser energy to 1.5 kJ. Flow characteristics at the higher
energy and using double-sided illumination should resemble the 200 J flat
target shots in nearly all respects, according to this estimate.

50

U3-2), while double-sided illumination should produce a divergence approaching 360 degrees (model U3-4). Model U3-2 is model UO, discussed in Section 2.

A summary of the results of these calculations is given in Table 5-2. Details of these results are given below.

5-2   GEOMETRICAL EFFECTS.

The model sequence shown here corresponds in many respects to the sequence in which the laser energy is varied (Section 3). The strong effect of the divergence of the flow, which was shown to be important when dealing with targets of varying radii (Figure 3-1), is also the most important feature when holding the target radius fixed, but varying the flow geometry. In particular, we will see that probably the most significant aspect of this sequence is the increase in the gradient of the density, temperature and pressure for models with a more spherical symmetry.

The variation of the radius (distance from a center of divergence) of the outer limit of the plasma and of the critical surface of the models at time = 7 ns is plotted in Figure 5-1. The radius of the critical surface is smaller for large divergence, since laser light can penetrate deeper in this case, but the effect is weak. The variation of the outer density, on the other hand (Figure 5-2) is strong, and reflects the geometry of the flow. Large divergence produces a significantly lower density in the outer corona. This larger density gradient in turn causes a decrease in the integrated absorption, as seen in Figure 5-3, while the KE fraction tends to increase in the large divergence case.

Figure 5-4 shows the variation expected in the maximum and outer temperatures as the divergence is varied. Higher flow divergence results in lower coronal temperatures and higher temperature gradients. The

49

SECTION 5

FLOW DIVERGENCE EFFECTS

Current experiments at NRL employ flat target geometry and result
in a strongly asymmetric plasma expansion. The upgraded system will
include the capability of two-sided target illumination and should produce
a more nearly spherically symmetric flow pattern - a highly desirable fea-
ture from a simulation point of view. In this section, we present the
results of a sequence of models in which all experimental parameters are
held fixed except the divergence angle of the flow. This is, of course, a
purely theoretical exercise since the flow divergence is not precisely con-
trollable in the experiment and must be estimated "a posteriori". As seen
in Section 3 of this report, however, a number of experimental parameters
do influence the degree of flow divergence, even in the flat target con-
figuration, and these effects can be measured. Also, a continuous sequence
of models could prove to be very useful in estimating parameters in cases
in which complete symmetry is not achieved, but differ strongly from the
one-sided case.

5-1   MODELS IN SEQUENCE U3.

A sequence of four models have been computed whose flow diver-
gence angle (see Figure 2-1) varies from 40 degrees to 360 degrees. All
other parameters of the disk target model are held fixed. The flow pattern
is varied by actually computing the flow in spherical geometry with parame-
ters as given in Table 5-1. Here a larger spherical radius produces a
smaller divergence angle, since the radius of the sector representing the
flat target is held fixed. The total energy and power for the spherical
model must be scaled in such a way as to hold the intensity fixed. Flat
target illumination corresponds to a divergence of about 80 degrees (model

48
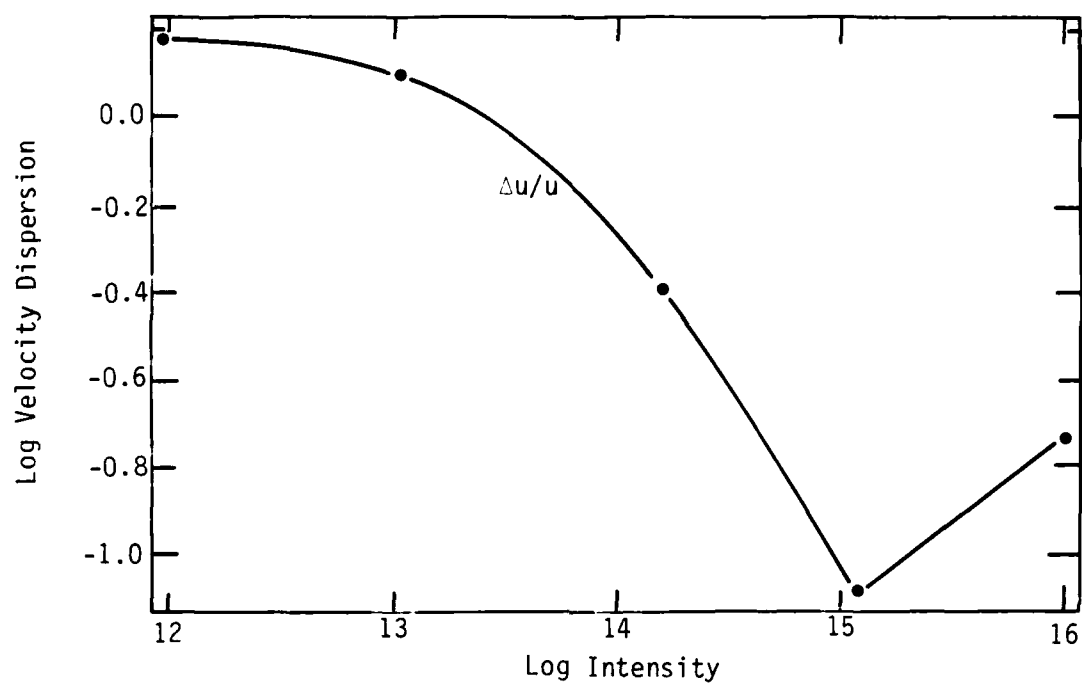
Figure 4-7. Width of the ion velocity distribution versus laser intensity.
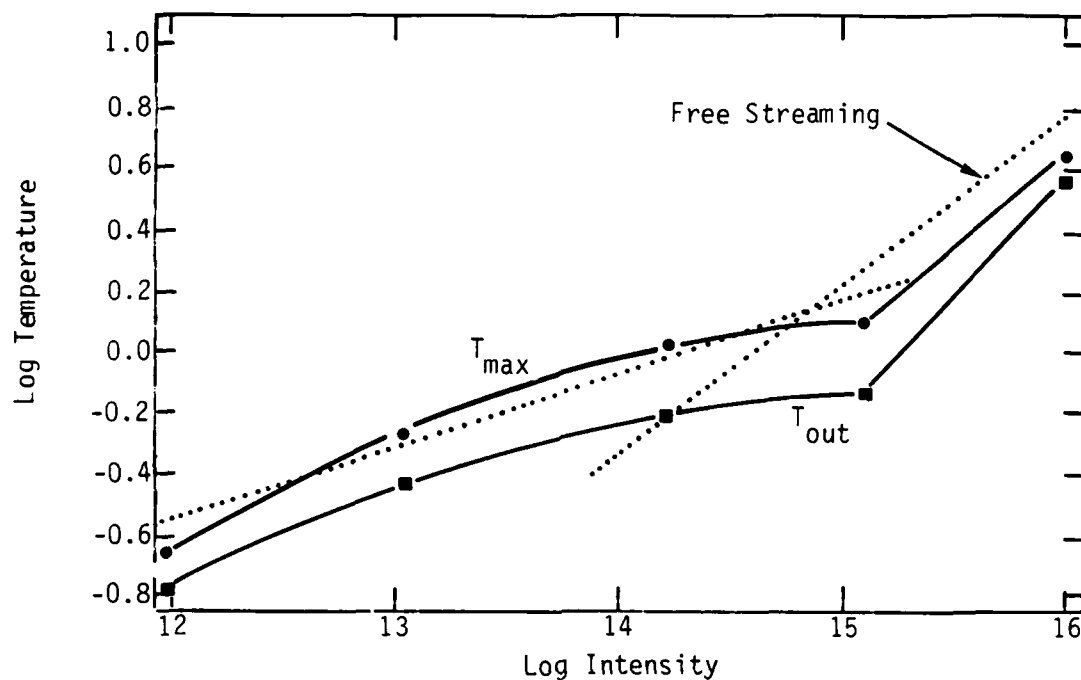
Figure 4-5. Coronal temperatures versus laser intensity, <u>dotted lines</u>: analytic fit based on steady conduction model.
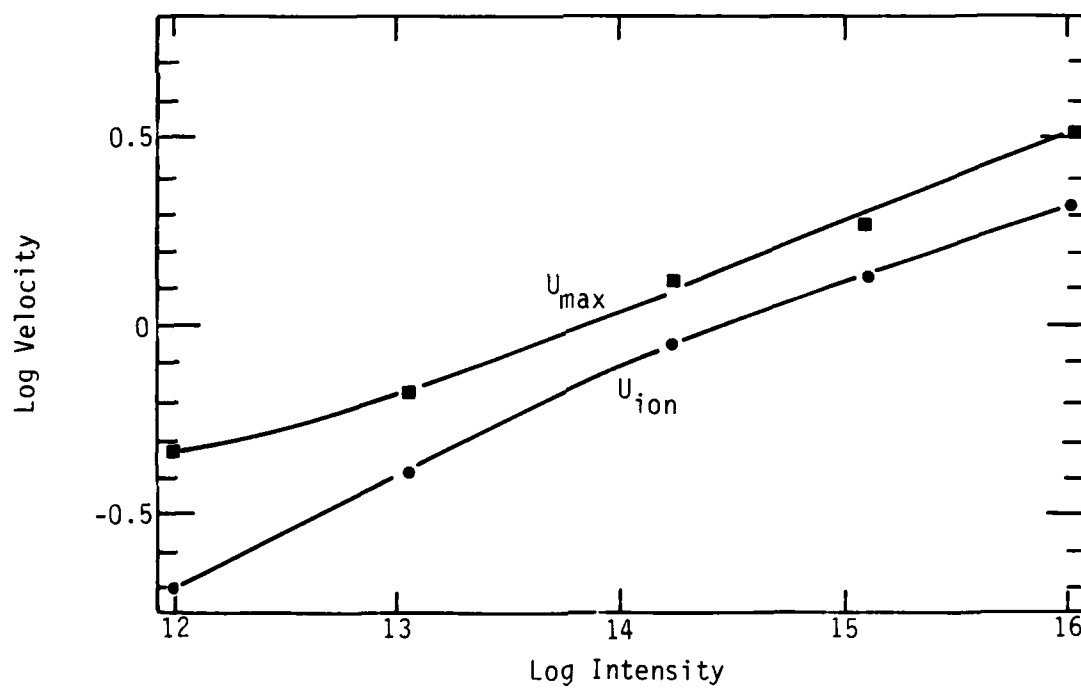
Figure 4-6. Coronal velocities versus laser intensity.
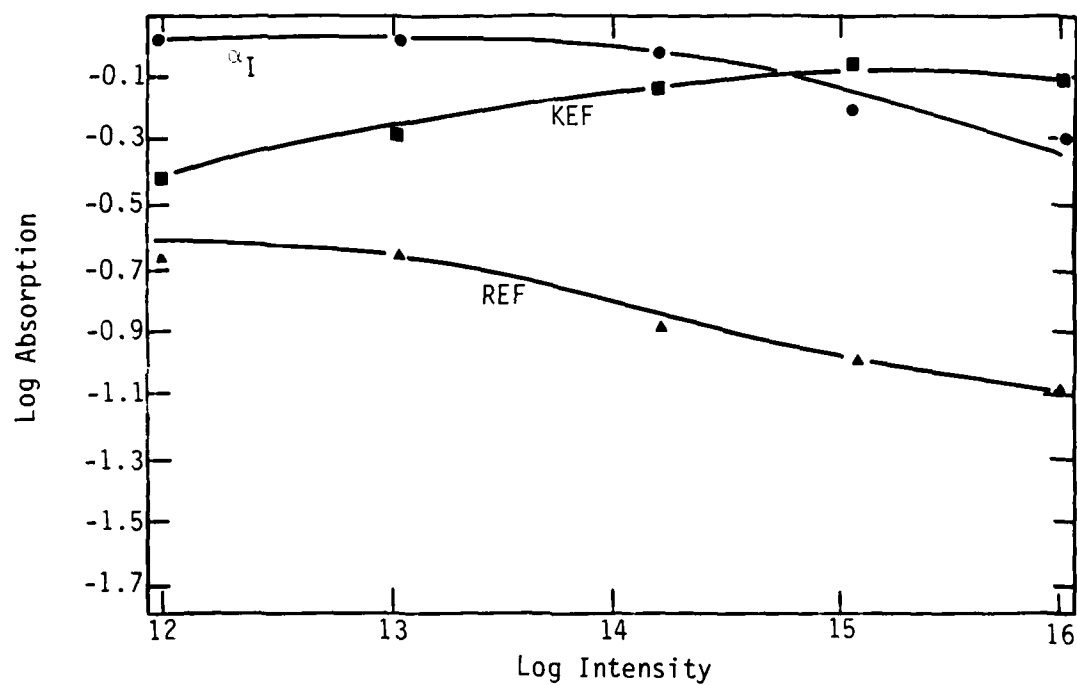
Figure 4-3. Integrated absorption, kinetic and radiative energy fractions versus laser intensity.
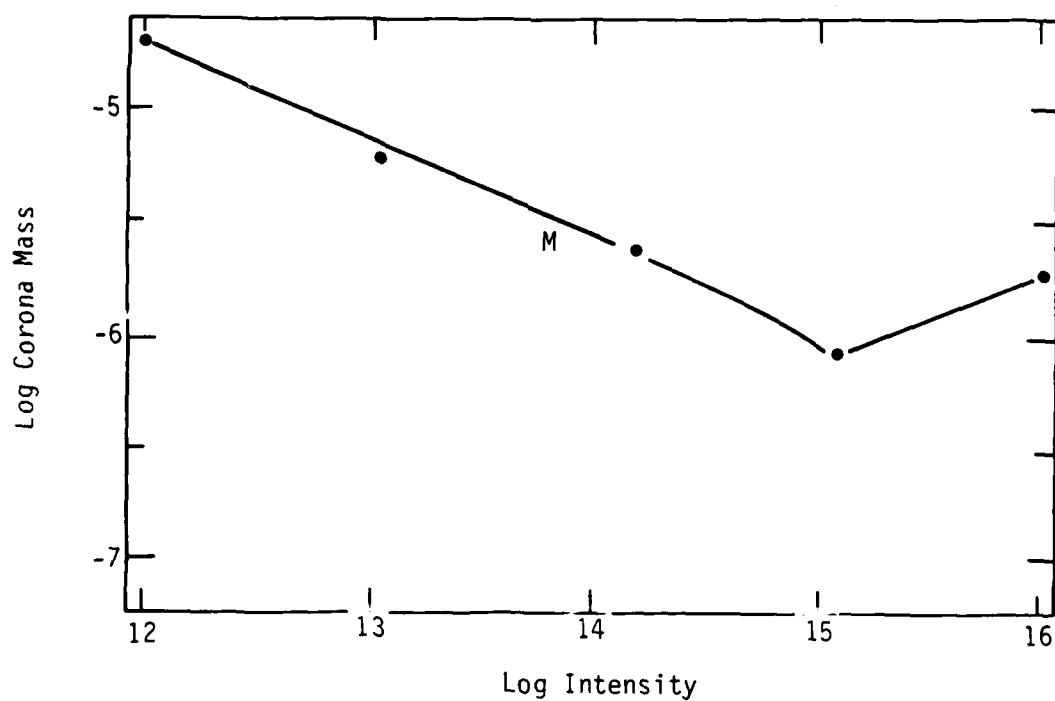
Figure 4-4. Coronal mass versus laser intensity.

45
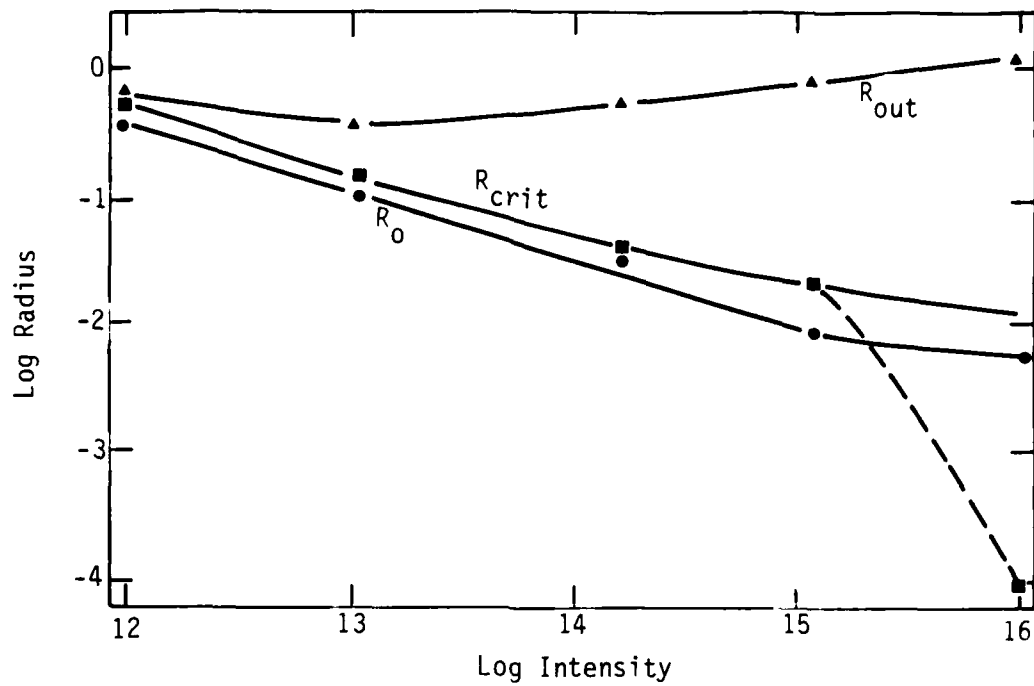
Figure 4-1. Target radii versus laser intensity.
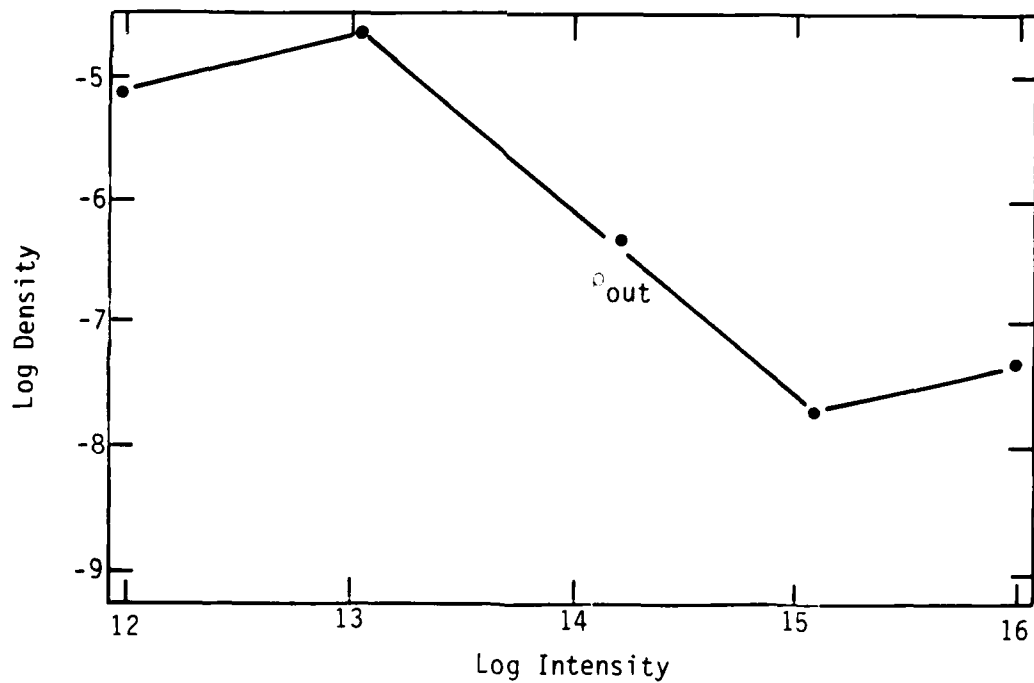
Figure 4-2. Outer coronal density versus laser intensity.

TABLE 4-3.

Sequence U2: Power law scale factors.

$Q = \alpha I^{\beta}$, r = correlation coefficient (log)

Quantity	α	β	r
Absorption	8.70± .7	-7.59E-2± .02	-0.90
KE fraction	3.37E-2± .003	8.85E-2± .02	0.92
RE fraction*	4.09± .2	-0.11± .01	-0.97
Corona Mass (g) (4)	7.23± .4	-0.46± .02	-1.00
U (ion peak)/10^8*	1.49E-4± 1E-5	0.26± .02	0.99
U_{max}/10^8	1.41E-3± 6E-5	0.21± .01	1.00
$\Delta U/U$* (4)	3.8E5± 1E5	-0.44±0.1	-0.94
R_{crit} (4)	2.87E5± E4	-0.48± .03	-1.00
R_{outer}*	3.58E-2± 7E-3	9.15E-2± .05	0.74
T_{max}*	5.14E-5± 5E-6	0.31± .04	0.98
T_{outer}*	1.23E-4± 1E-5	0.26± .04	0.98
ρ_{outer}*	2.82E6± 6E6	-0.92± .3	-0.89

*These quantities show curvature in their logarithmic dependence on I.

**Quantities marked "(4)" include models 1-4 only.

43

TABLE 4-1.

Sequence U2: Laser intensity - target radius variation.

Model No.	E disk	R disk	P disk	E sphere	R sphere	P sphere
U2-1	1.50	0.0333	3.9E11	12.8	0.4873	3.3E12
U2-2	1.50	0.1050	3.9E11	12.8	0.1540	3.3E12
U2-3	1.50	0.0290	3.9E11	12.8	0.0430	3.3E12
U2-4	1.50	0.0093	3.9E11	12.8	0.0136	3.3E12
U2-5	15	0.0079	3.9E11	128	0.0115	3.3E13

TABLE 4-2.

Model results for sequence U2.

	-1-	-2-	-3-	-4-	-5-
Run number	U2-1	U2-2	U2-3	U2-4	U2-5
E laser (d)	1.5	1.5	1.50 kJ	1.5	15
Wavelength	1.06	1.06	1.06 mic	1.06	1.06
Pulse Length	3.4	3.4	3.4 ns	3.4	3.4
Target Z	13	13	13	13	13
*Radius (d)	0.3330	0.1050	0.0290 cm	0.0093	0.0079
Divergence	80	80	80 deg	80	80
*Intensity-a	1.06E12	1.03E13	1.28E14	8.70E14	9.78E15
Absorption	0.95	0.93	0.90	0.61	0.49
KE fraction	0.35	0.49	0.69	0.79	0.75
RE fraction	0.21	0.20	0.13	0.10	0.09
Corona Mass	1.91E-5	6.25E-6	2.29E-6 g	7.95E-7	1.96E-6
U(ion peak)	0.20	0.40	0.91 (8)	1.30	2.20
U max	0.47	0.68	1.37 (8)	1.96	2.96
Delta U/U	1.50	1.25	0.38	0.08	0.18
R crit	0.4898	0.1567	0.0385 cm	0.0210	0.0001
R outer	0.6498	0.3721	0.5770 cm	0.8697	1.2100
T max	0.22	0.56	1.26 keV	1.67	6.46
T outer	0.16	0.38	0.75 keV	0.92	6.04
Rho outer	6.27E-6	1.73E-5	3.76E-7 g/	2.02E-8	5.10E-8

*Varied Quantities

4-5   SUMMARY OF INTENSITY EFFECTS.

Models have been computed with intensity ranging from 10^{12} to 10^{16} W/cm^2. The main conclusions drawn from this sequence are:

1. In the range considered, the plasma temperatures in the corona and near the critical surface scale as absorbed intensity to the 0.26-0.31 power. This is the dependence expected from classical laser deposition and thermal conductivity.

2. Coronal ion velocities depend strongly on intensity ($U \propto I^{.25}$) and range from 2×10^7 to 2×10^8 cm/s as intensity is varied.

3. The ion velocity dispersion decreases at higher intensities, probably indicating incipient shock formation.

and 4-4. These relations are plotted as dotted lines in Figure 4-5, and
they clearly represent the data very well. The slope determined by the
first four models is 0.31 for T_{max} and 0.26 for T_{outer}, as compared to
2/7=0.286 in the analytic formula. We see that the free-streaming electron
"flux limit" is expected to become operable at laser intensities in excess
of 10^{15} W/cm^2. In this case it is usually the case that smaller values of
"f" are needed to correctly estimate the coronal temperatures, so present
estimates of temperature and velocity could be low at the highest intensi-
ties in this sequence.

The velocity scales as $I^{.25}$ (Table 4-3), which is somewhat
stronger than the sound speed scaling of $I^{.15}$. Another strong trend is
the narrowing of the velocity distribution as intensity is increased, a
result of shock formation at higher intensities. Inspection of the time
histories of the computations indicates that this is a result of the flow
initially setting up a steady-flow type of structure, and then becoming
nearly isothermal at a later time as the laser intensity increases.

4-4   OTHER EFFECTS.

Figures 4-1 and 4-2 show the progression of model radii and outer
densities as the intensity is increased. These results follow directly
from the behavior of the velocities. In Figure 4-3 the absorption quanti-
ties are shown. Total absorption decreases at higher intensities, as
expected. In the limit, sharp density gradients near the critical surface
should virtually eliminate the coronal deposition, leaving only the 30%
deposited at the critical surface. In addition, we note that the amount of
radiated energy tends to decrease at higher intensities, as coronal temper-
atures increase.

4-3   TEMPERATURE AND VELOCITY EFFECTS.

The temperature obtained in these models can be understood as resulting from a balance of the incoming laser energy flux and the thermal conduction flux to the deeper layers. The classical thermal flux term is given by (Spitzer, L. 1962, Physics of Fully ionized Gases, Interscience, NY):

$$\text{flux} \approx 10^{-4} \, f \, \frac{T_e^{5/2}}{Z \, \ln\lambda} \, \frac{dT_e}{dr} \quad \text{(cgs)} \tag{4-2}$$

where T_e is the electron thermal temperature, and $f=0.4$. Here we may approximate $dT_e = T_{max}$ and $dr = $ few microns to obtain an estimate of the flux. If we equate the result to the absorbed laser intensity we find the scaling law:

$$T_e(\text{keV}) \approx (I/10^{14} \, \text{W/cm}^2)^{2/7}, \quad \text{(classical)}, \tag{4-3}$$

which is very close to the scaling laws given in Table 4-3 for T_{max} and T_{outer}. For very high temperatures, it is known that this type of relation overestimates the flux. In the models the flux is limited to the classical free-streaming value (Equation 4-1). In this case we have:

$$\text{flux} \approx f \, (n_e T_e)(T_e/m_e)^{1/2}, \quad \text{(free-streaming)}, \tag{4-4}$$

where, again, we have $f=0.4$ (this factor accounts for the cold electron return current), and the two terms represent the electron energy density and velocity. Equating this flux to the intensity, and taking $n_e = n_{crit}$, we obtain:

$$T_e(\text{keV}) \approx [(0.4/f)(I/10^{14} \, \text{W/cm}^2)(\lambda)^2]^{2/3}, \tag{4-5}$$

where λ is the laser wavelength in microns. The actual temperature at the critical surface should be the maximum of the values given in equations 4-3

39

At higher intensities, care must be taken to include a variety of parametric laser processes not important in the lower intensity regime. We include here a brief discussion of the treatment of several of these.

It is well known that at higher intensities there is a tendency for the density gradient at the critical surface to steepen (caused by a number of factors including ponderomotive force), and consequently the inverse Bremsstrahlung absorption is weakened and tends to be replaced by other absorption mechanisms, such as resonant absorption, operating at the critical surface. In these models this situation is modeled in a very simple way: the coronal absorption is computed at a given time during the calculation, and 30% of the energy that penetrates to the critical surface is assumed to be absorbed at that point. The rest is reflected and may deposit further energy while traversing the corona a second time. At the critical surface a temperature is computed for "hot electrons" presumably created via resonance absorption. These hot electron s are seen primarily in experiments at longer laser wavelengths, and in all cases computed here, the hot electron temperature was found to be nearly equal to the thermal electron temperature. This implies that the absorbed energy appears at the critical surface as a heating mechanism for thermal electrons. The contribution of the critical surface absorption to the total absorption is very small at low intensities, but increases to about 0.20 for models U2-4 and U2-5. It is a small effect and the present treatment is probably adequate.

Other processes, operating in the vicinity of 1/4 critical density, have been observed in experiments. These are Raman scattering and Brillouin scattering. These processes can also produce suprathermal electrons that may act as an energy loss mechanism and a pre-ionizing agent in the background gas. These mechanisms are not thought to be important in the present experiments, however, and are ignored in these calculations. If observed, they will be added in future studies.

TABLE 5-3.

Sequence U3: Power law scale factors.

$$Q = \alpha\theta^\beta, \ r = \text{correlation coefficient (log)}$$

Quantity	α	β	r
Absorption*	$1.474\pm.03$	$-0.117\pm.02$	-0.96
KE fraction	$0.456\pm.006$	$0.088\pm.02$	0.97
RE fraction	0.152 ± 0.002	$-0.030\pm.02$	-0.75
Corona Mass (g)	$2.66E-6\pm8E-8$	$-0.025\pm.04$	-0.42
U (ion peak)$/10^8$*	$0.830\pm.02$	$0.008\pm.003$	0.17
$U_{max}/10^8$	$1.902\pm.03$	$-0.084\pm.02$	-0.94
$\Delta U/U$	$21.4\pm.2$	$-0.876\pm.1$	-0.99
Rcrit	$1.09\pm.2$	$-0.729\pm.2$	-0.92
Router	$0.826\pm.01$	$-0.087\pm.02$	-0.95
T_{max}*	$4.59\pm.3$	$-0.311\pm.06$	-0.96
T_{outer}	$7.13\pm.2$	$-0.528\pm.04$	-1.00
ρ_{outer}	$2.25E-4\pm3E-5$	$-1.405\pm.1$	-1.00

*These quantities show curvature in their logarithmic dependence on θ.

52
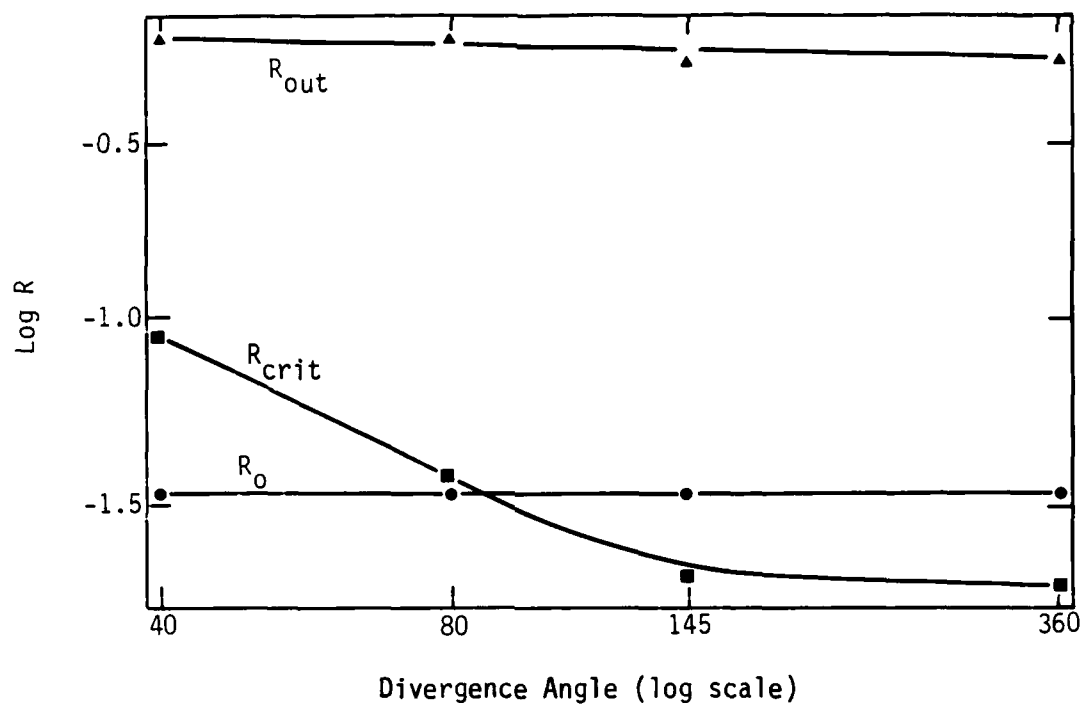
Figure 5-1. Target radii versus flow divergence.
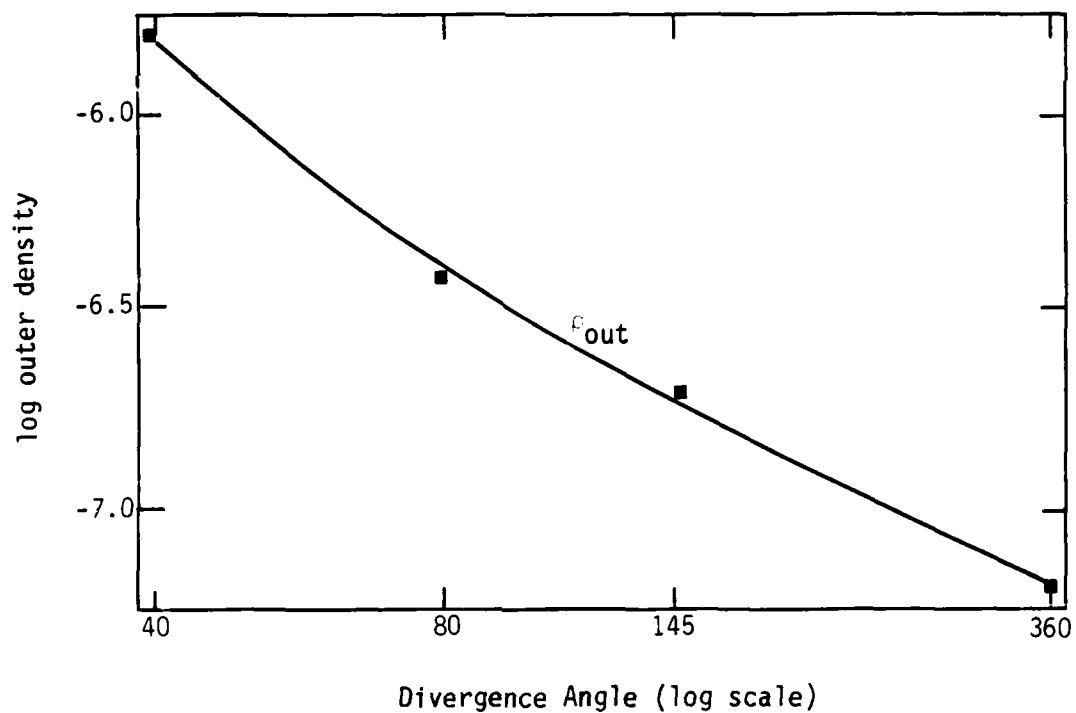
Figure 5-2. Outer density versus flow divergence.
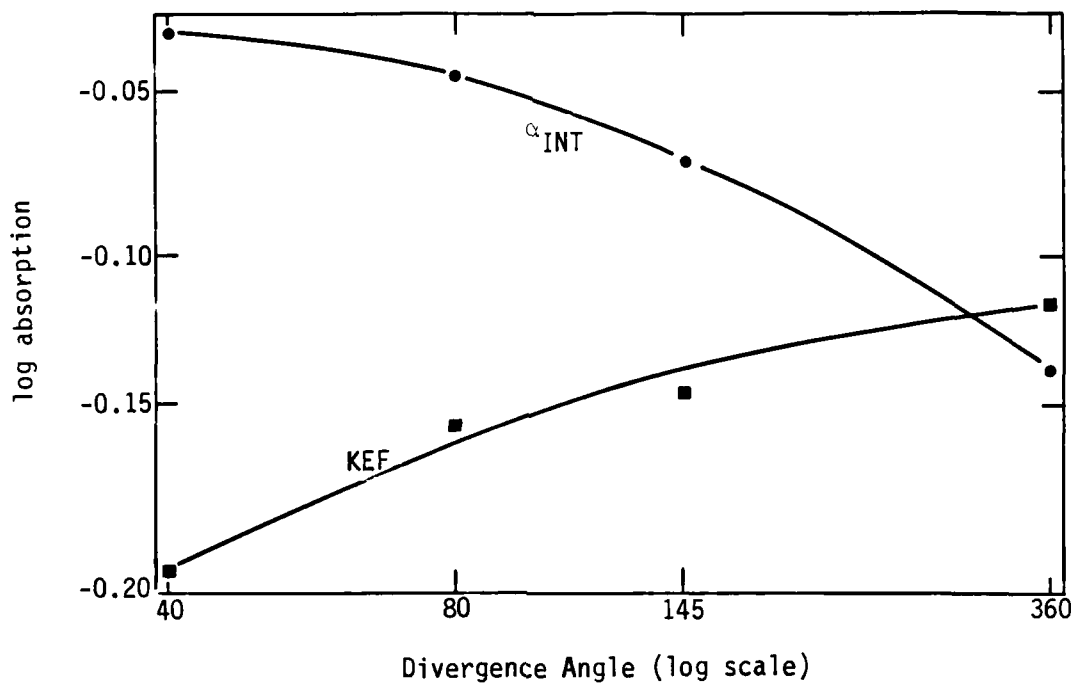
Figure 5-3. Integrated absorption and KE fraction versus flow divergence.
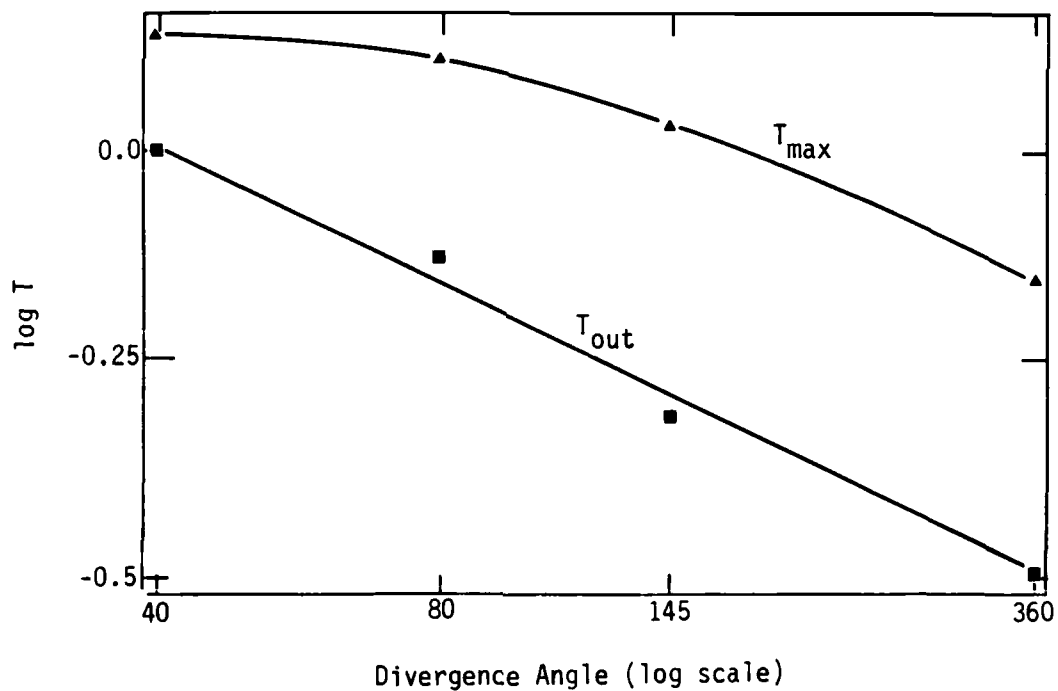
Figure 5-4. Coronal temperatures versus flow divergence.

54
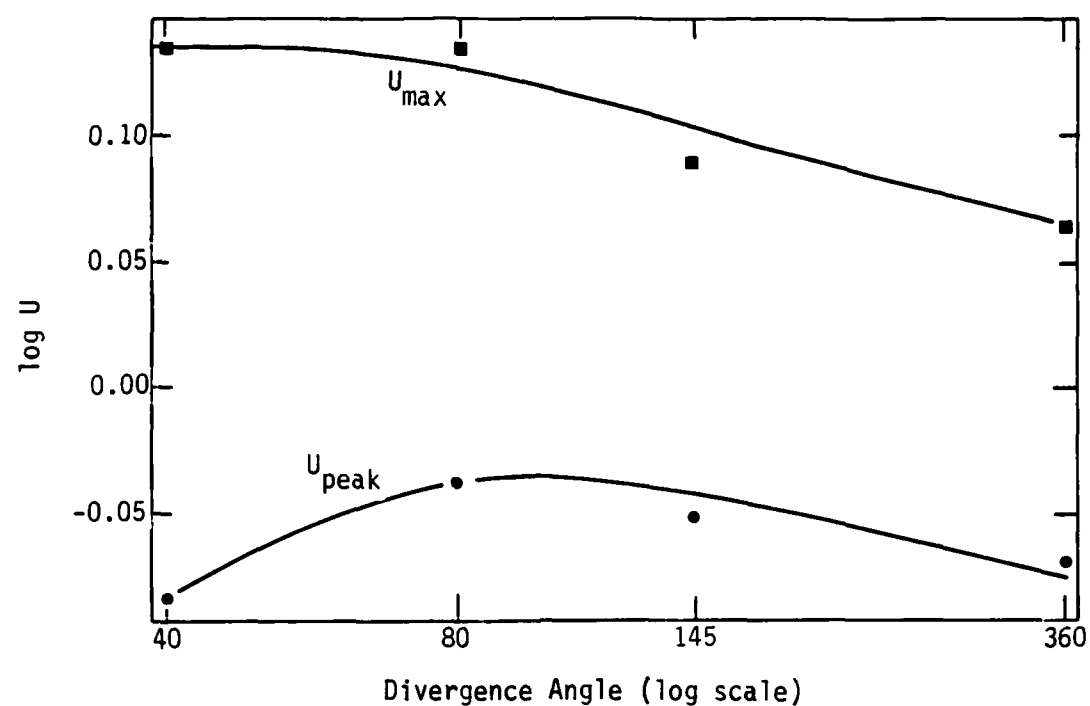
Figure 5-5. Coronal velocities versus flow divergence.
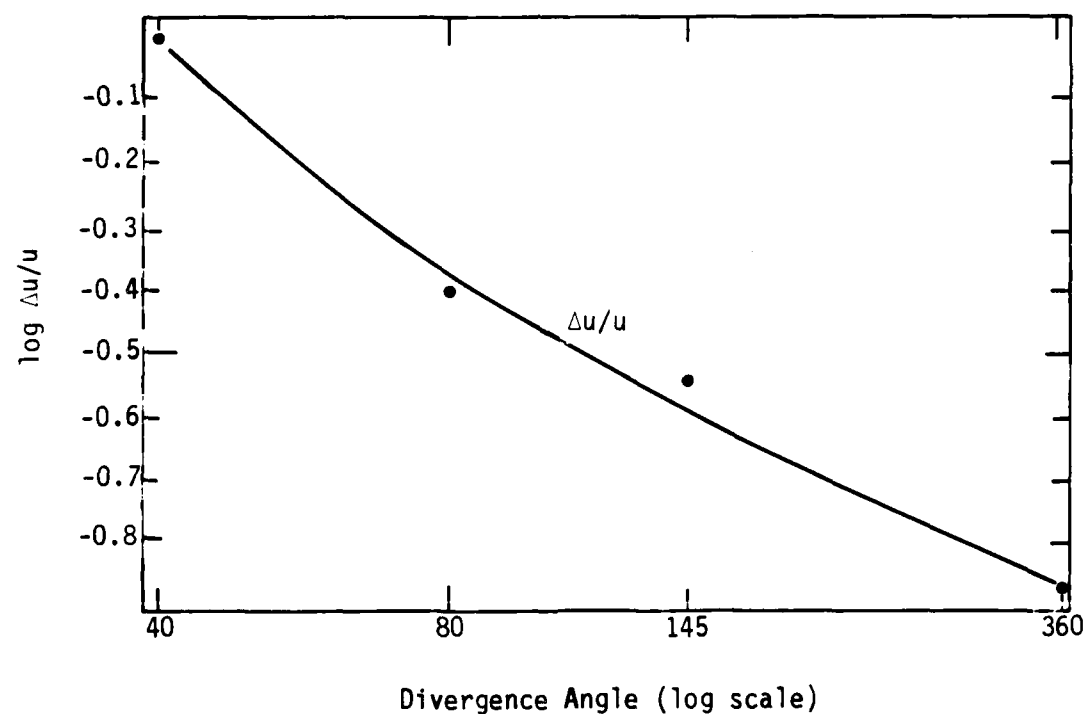
Figure 5-6. Width of the velocity distribution versus flow divergence.

55

SECTION 6

LASER WAVELENGTH EFFECTS

The upgraded NRL Laser facility is planned to include the capability of laser wavelength variation. Wavelengths of 1.06, 0.53, and possibly 0.26 should be available. Shorter wavelengths penetrate to greater depth in the target material and are believed to produce a more efficient ablation flow. It is thus of interest to investigate the effects of wavelength variation on the parameters of interest to the HANE simulation. The models discussed here incorporate the effects of wavelength on absorption, but do not model the various parametric processes, such as Raman scattering, that play an important role at higher intensities.

Three sequences of models have been run to investigate these effects, as summarized here:

Sequence U4: wavelength, intensity and target diameter varied to maintain constant $I\lambda^2$.

Sequence U4B: wavelength, intensity and laser energy varied to maintain constant $I\lambda^2$.

Sequence U4C: only wavelength varied.

Sequencies 4 and 4B are constructed in such a way as to remove the strongest expected variation due to the changing critical surface density, and allow determination of the actual corrections to this expected trend. Sequence 4C was run as a test of wavelength effects at fixed intensity and laser energy.

6-1   MODELS IN SEQUENCE U4.

          The model parameters for the models in sequence U4 are given in
Table 6-1, and the model results are summarized in Table 6-2. Model U4-3
is the same as model U0. The results of simple regression calculations of
the various quantities versus wavelength are given in Table 6-3.

          This sequence maintains constant the product of wavelength
squared and intensity by varying the target size. This procedure
undoubtedly introduces trends due to the variation of geometric factors
(flow divergence). The other sequences discussed below will be used to
evaluate these effects.

          The most important result found here is the increase in the flow
velocity found for smaller wavelengths; we find U proportional to $\lambda^{-0.3}$.
Note that this trend is not due to strong temperature variation with wave-
length, so the cause must be a change in the flow structure itself. This
is illustrated in Figure 6-1: model U4-1 shows a velocity structure that
peaks strongly at a small radius (leading to shock formation), while model
U4-4 shows a nearly linear increase in the velocity versus radius - charac-
teristic of rarefaction expansion. Examination of the models reveals the
reason for this behavior: the timescale for the ablation process depends
on intensity, rather than $I\lambda^2$, so the long wavelength low intensity models
ablate much slower than the short wavelength high intensity models. In
fact, for model U4-4, the corona does not begin to form until most of the
laser energy has been deposited, and the resulting flow approximates a
self-similar rarefaction expansion. On the other hand, model U4-1 ablates
quickly and the velocity is able to track the increase of the laser inten-
sity in time over the pulse length of 3.4 ns; this produces higher veloci-
ties at later times and a flow structure more closely resembling that of a
steady flow in the inner regions of the corona. Another related effect is
a narrower velocity distribution for the short wavelength models due to the
shock formation tendency in the flow.

6-2   MODELS IN SEQUENCE U4B.

To check the results found in the previous section, an additional
sequence of models was computed in which the product of intensity and wave-
length squared was again maintained constant, but here the laser energy was
varied (to vary the intensity) rather than the target size. The resulting
models are less realistic since large laser energies are postulated but
have the advantage that target geometry is constant across the sequence.
The model parameters for sequence U4B are given in Table 6-4, the model
results in Table 6-5, and the power law scale factors are given in Table
6-6.

It is seen that, with the exception of corona mass, all trends
agree rather well between sequences U4 and U4B. In particular, the velo-
city scales as $\lambda^{-0.4}$, and the shorter wavelengths again produce narrower
velocity distributions. The velocity and density structure found here is
very similar to that shown in Figure 6-1. This agreement is consistent
with the ablation timescale argument presented above, since both wavelength
and intensity are nearly identical for the two sequences.

6-3   MODELS IN SEQUENCE U4C.

As a further test of these results, a third sequence of models
was computed in which only the wavelength of the laser light was varied.
In this sequence, all models have identical laser energy and nearly identi-
cal laser intensity. Thus, here we would expect that the ablation time-
scale would be nearly constant across the sequence (to first order), so
that the direct effects of variable wavelength can be assessed. As shown
in previous sections, in general, the dependence of coronal velocity on
intensity is given by U proportional to $I^{0.2}$. If this dependence
actually applies to the quantity $I\lambda^2$, as suggested by simple physical argu-
ments invoking the plasma density at critical, then we would expect U pro-
portional to $\lambda^{0.4}$ for the present models.

The model results for this sequence are given in Table 6-7, and
the power law scale factors are summarized in Table 6-8. We see immedi-
ately that the dependence on wavelength is much weaker than predicted.
This is partially due to the decrease in the absorption fraction at 2.5
microns, which lowers I (absorbed) and depresses the velocity at the long
wavelength end of the sequence. If only the first three models are used,
then the exponent (β) increases from 0.06 to 0.21 for U_{ion}, and increases
from 0.23 to 0.35 for U_{max}. These values are still somewhat lower than
expected and account for part of the trend in the first two sequences
discussed above.

It is worthwhile noting that the primary effect of varying the
wavelength is the strong change in critical surface density, which varies
as λ^{-2}. This has a strong effect on the temperature structure of the
corona. We see that the maximum temperature shown in Table 6-7 changes
very little as wavelength is varied, but the temperature gradient does
vary: the corona is very nearly isothermal at longer wavelengths, but shows
a strong gradient at the shorter wavelengths. This effect works in much
the same way as the timescale effects discussed with reference to sequences
U4 and U4B - at shorter wavelengths acceleration of the coronal ions occurs
at smaller radii and is stronger than the expansion-wave type acceleration
found at long wavelengths. Also, the ion and electron temperatures tend to
remain coupled at shorter wavelengths. Figure 6-2 shows the temperature
and velocity structure for models U4C-1 and U4C-4, which illustrate these
points. This trend affects the ion velocity distribution, and can be
detected using charge cup data in experiments. Figure 6-3 illustrates the
type of differences predicted for shots with different wavelengths. The
trend in the width of the velocity distribution is quite dramatic and
should be easily detectable.

6-4   CONCLUSIONS ON WAVELENGTH SCALING.

In this section, three sequences of models with varying laser
wavelength have been discussed. The main conclusions are:

1. If the laser wavelength is varied with all other parameters
held fixed, the increase in coronal velocity with increasing wavelength is
weaker than expected from simple scaling arguments. The reason for this is
the change in coronal structure caused by larger temperature gradients at
shorter wavelengths.

2. If the laser wavelength is varied with $I\lambda^2$ held fixed, then
these models actually predict larger coronal velocities for the shorter
wavelength shots. The strongest effect here appears to be the transition
from an impulse-response type of behavior at long wavelengths to a quasi-
steady flow response at short wavelengths in which the flow can respond to
the shape of the laser pulse.

3. In all cases we find narrower velocity distributions at
shorter wavelengths, a desirable feature for HANE simulations. In addi-
tion, we see a definite tendency toward strong shock formation in the outer
coronal regions for models with short wavelengths and high intensities.
Both of these trends indicate that shorter wavelengths should be considered
for HANE modeling.

4. These models confirm that excellent absorption efficiency
should be obtainable at shorter wavelengths. Absorption fractions near 90%
are found at 0.25, 0.50, and 1.06 micron wavelengths for laser energy
1.5 kJ.

TABLE 6-1.

Sequence U4: Laser Wavelength Variation

Model No.	E disk	R disk	P disk	E sphere	R sphere	P sphere
U4-1	1.5	0.0069	3.9E11	12.8	0.0100	3.3E12
U4-2	1.5	0.0140	3.9E11	12.8	0.0200	3.3E12
U4-3	1.5	0.0290	3.9E11	12.8	0.0430	3.3E12
U4-4	1.5	0.0660	3.9E11	12.8	0.0960	3.3E12

TABLE 6-2.

Model Results - Wavelength Sequence U4

	-1-	-2-	-3-	-4-
Run number	U4-1	U4-2	U4-3	U4-4
E laser (d)	1.5	1.5	1.5 kJ	1.5
*Wavelength	0.25	0.50	1.06 µm	2.50
Pulse length	3.4	3.4	3.4 ns	3.4
Target Z	13	13	13	13
*Radius (d)	0.0064	0.0140	0.0290 cm	0.0660
Divergence	80	80	80 deg	80
*Intensity-a	1.64E15	4.4E14	1.28E14 W/cm^2	2.0E13
Absorption	0.64	0.79	0.90	0.68
KE fraction	0.75	0.77	0.69	0.53
RE fraction	0.14	0.13	0.13	0.15
Corona Mass	7.47E-7	1.46E-6	2.29E-6 g	2.14E-6
U ion peak	1.25	1.15	0.91 (8) cm/s	0.60
U max	1.61	1.56	1.37 (8) cm/s	0.91
Delta U/U	0.16	0.13	0.38	1.17
R crit	0.0001	0.0175	0.0385 cm	0.1314
R outer	0.7088	0.6915	0.5770 cm	0.3864
T max	1.4	1.27	1.26 keV	0.99
T outer	1.05	0.47	0.75 keV	0.88
Rho outer	2.38E-8	6.83E-8	3.76E-7 g/cm^3	3.59E-6

*Varied Quantities

TABLE 6-3.

Sequence U4: Power Law Scale Factors

$$Q = \alpha\lambda^{\beta}, \quad r = \text{correlation coefficient}$$

Quantity	α	β	r
Absorption	0.753 ± .08	0.034 ± .1	0.22
KE fraction	0.650 ± .03	-0.154 ± .05	-0.89
RE fraction	0.138 ± .005	0.030 ± .04	0.43
Corona Mass*	1.73E-6 ± 3E-7	0.459 ± .2	0.89
U ion peak*	0.861 ± .04	-0.322 ± .06	-0.97
U max*	1.243 ± .08	-0.245 ± .07	-0.92
Delta U/U*	0.401 ± .1	0.935 ± .3	0.93
R crit*	0.021 ± .05	2.857 ± -1	0.89
R outer	0.534 ± .03	-0.266 ± -.07	-0.94
T max	1.174 ± .04	-0.139 ± -0.4	-0.93
T outer*	0.756 ± .2	4.07E-3 ± .2	0.01
Rho outer	3.97E-7 ± 7E-8	2.200 ± .2	0.99

*These quantities show curvature in their logarithmic dependence on E_L.

TABLE 6-4.

Sequence U4B - LASER wavelength and energy variation

Model No.	E disk	R disk	P disk	E sphere	R sphere	P sphere
U4B-1	27.00	0.0290	6.90E12	230.81	0.0430	5.93E13
U4B-2	6.74	0.0290	1.77E12	57.62	0.0430	1.48E13
U4B-3	1.50	0.0290	3.90E11	12.80	0.0430	3.30E12
U4B-4	0.27	0.0290	6.93E10	2.31	0.0430	5.93E11

TABLE 6-5.

Model Results - Wavelength Sequence U4B

	-1-	-2-	-3-	-4-
Run Number	U4B-1	U4B-2	U4B-3	U4B-4
*E laser (d)	27.00	6.74	1.5 kJ	0.27
*Wavelength	0.25	0.50	1.06 μm	2.5
Pulse Length	3.4	3.4	3.4 ns	3.4
Target Z	13	13	13	13
Radius (d)	0.0290	0.0290	0.0290 cm	0.0290
Divergence	80	80	80 deg	80
*Intensity-ab	2.25E15	5.80E14	1.28E14 W/cm^2	1.93E13
Absorption	0.88	0.90	0.90	0.67
KE fraction	0.73	0.74	0.69	0.59
RE fraction	0.17	0.14	0.13	0.15
Corona Mass	1.47E-5	5.79E-6	2.29E-6 g	4.67E-7
U ion peak	1.50	1.15	0.91 (8) cm/s	0.60
U max	2.29	1.82	1.37 (8) cm/s	0.85
Delta U/U	0.17	0.18	0.38	0.92
R crit	0.0167	0.0265	.0385 cm	0.0708
R outer	1.0088	0.7912	.5770 cm	0.3247
T max	3.74	2.09	1.26 keV	0.71
T outer	1.17	1.026	0.75 keV	0.54
Rho outer	1.23E-7	2.00E-7	3.76E-7 g/cm^3	1.10E-6

*Varied Quantities

TABLE 6-6.

Sequence U4B: Power Law Scale Factors

$$Q = \alpha\lambda^{\beta}, \ r = \text{correlation coefficient}$$

Quantity	α	β	r
Absorption	0.0806 ± .04	-0.111 ± .07	-0.76
KE fract	0.667 ± .02	-0.095 ± .03	-0.90
RE fract .	0.144 ± .01	-0.054 ± .07	-0.46
Corona Mass*	2.05E-6 ± 2E-7	-1.478 ± .1	-1.00
U ion peak*	0.884 ± .02	-0.391 ± .03	-1.00
U max*	1.319 ± .04	-0.428 ± .04	-0.99
Delta U/U*	0.398 ± .06	0.768 ± .2	0.96
R crit*	0.039 ± .001	0.615 ± .03	1.00
R outer	0.543 ± .03	-0.489 ± .05	-0.99
T max	1.33 ± .03	-0.715 ± .03	-1.00
T outer*	0.759 ± .02	-0.346 ± .03	-0.99
Rho outer	4.12E-7 ± 4E-8	0.947 ± .1	0.99

*These quantities show curvature in their logarithmic dependence on E_L.

TABLE 6-7.

Model Results - Wavelength Sequence U4C

	-1-	-2-	-3-	-4-
Run Number	U4C-1	U4C-2	U4C-3	U4C-4
E laser (d)	1.5	1.5	1.5 kJ	1.5
*Wavelength	0.25	0.50	1.06 μm	2.5
Pulse Length	3.4	3.4	3.4 ns	3.4
Target Z	13	13	13	13
Radius (d)	0.0290	0.0290	0.0290 cm	0.0290
Divergence	80	80	80 deg	80
Intensity-ab .	1.42E14	1.40E14	1.28E14 W/cm^2	9.68E13
Absorption	0.98	0.97	0.90	0.67
KE fraction	0.62	0.67	0.69	0.64
RE fraction	0.23	0.17	0.13	0.13
Corona Mass	4.19E-6	3.13E-6	2.29E-6 g	1.44E-6
U ion peak	0.67	0.76	0.91 (8) cm/s	0.75
U max	0.82	1.10	1.37 (8) cm/s	1.39
Delta U/U	0.04	0.13	0.38	1.00
R crit	0.0212	0.0268	0.0385 cm	0.0804
R outer	0.4396	0.5919	0.5770 cm	0.5429
T max	1.00	1.12	1.26 keV	1.29
T outer	0.17	0.35	0.75 keV	1.077
Rho outer	2.44E-6	7.95E-7	3.76E-7 g/cm^3	3.42E-7

*Varied Quantities
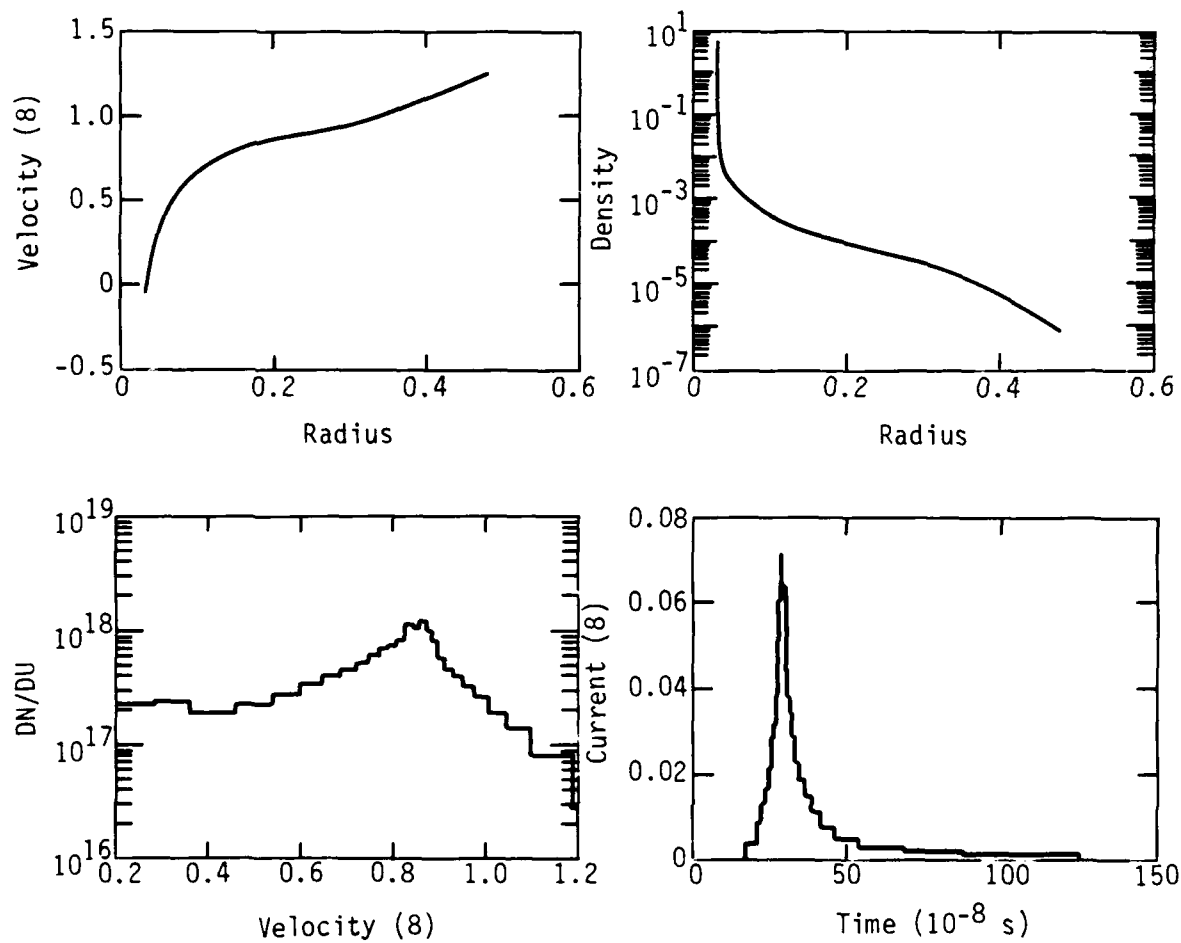
Figure 7-5. Characteristics of Model U5-5 at time = 7 ns.
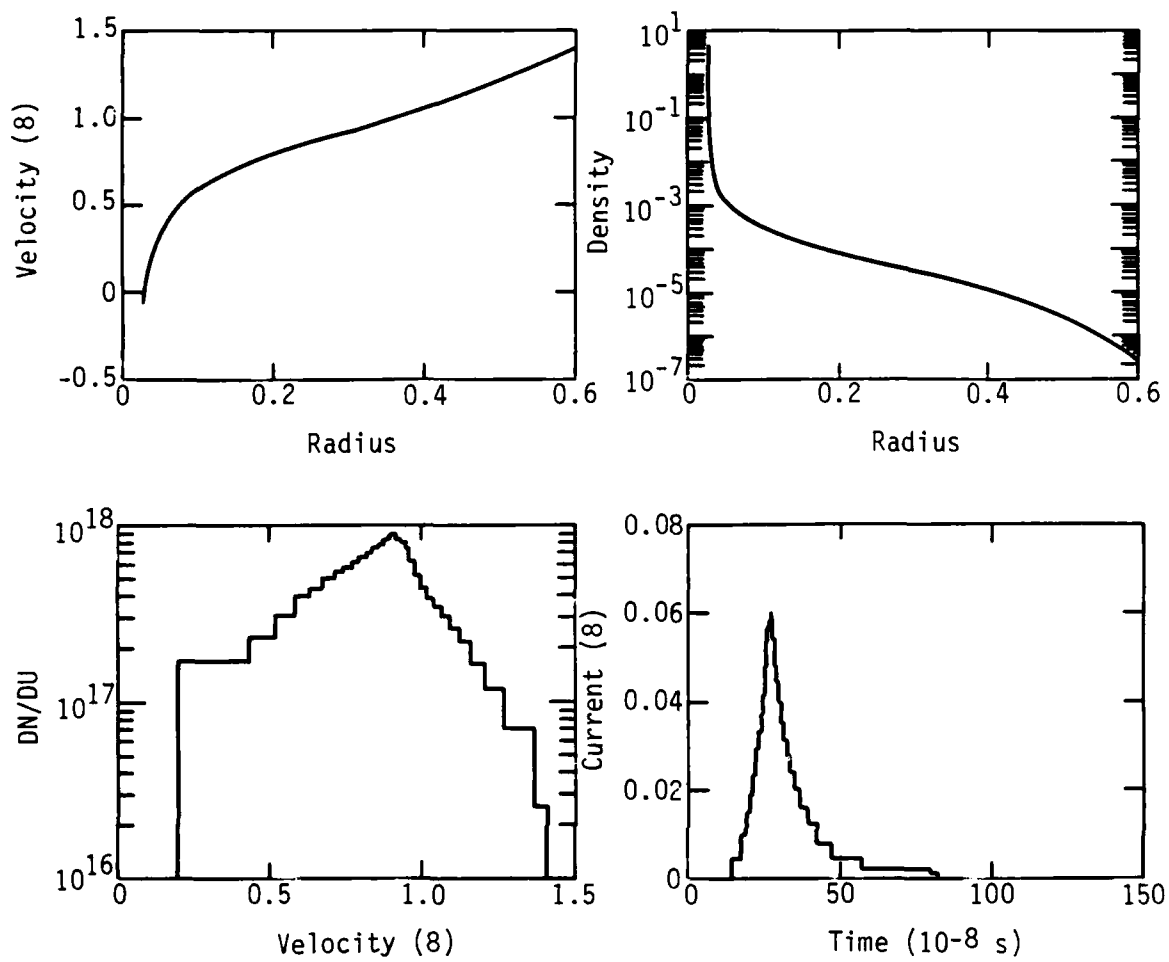
Figure 7-4. Characteristics of Model U5-4 at time = 7 ns.
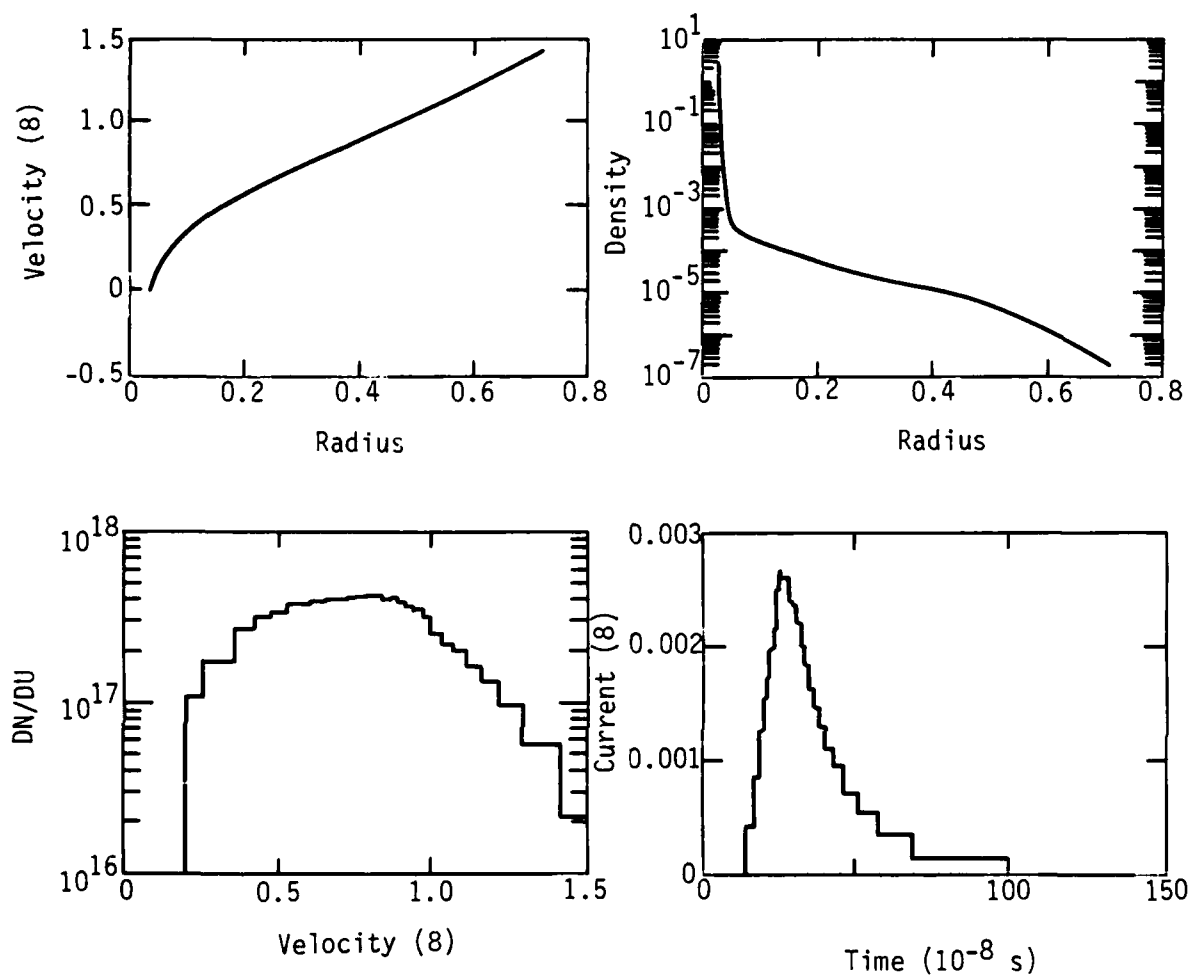
Figure 7-3.   Characteristics of Model U5-3 at time = 7 ns.
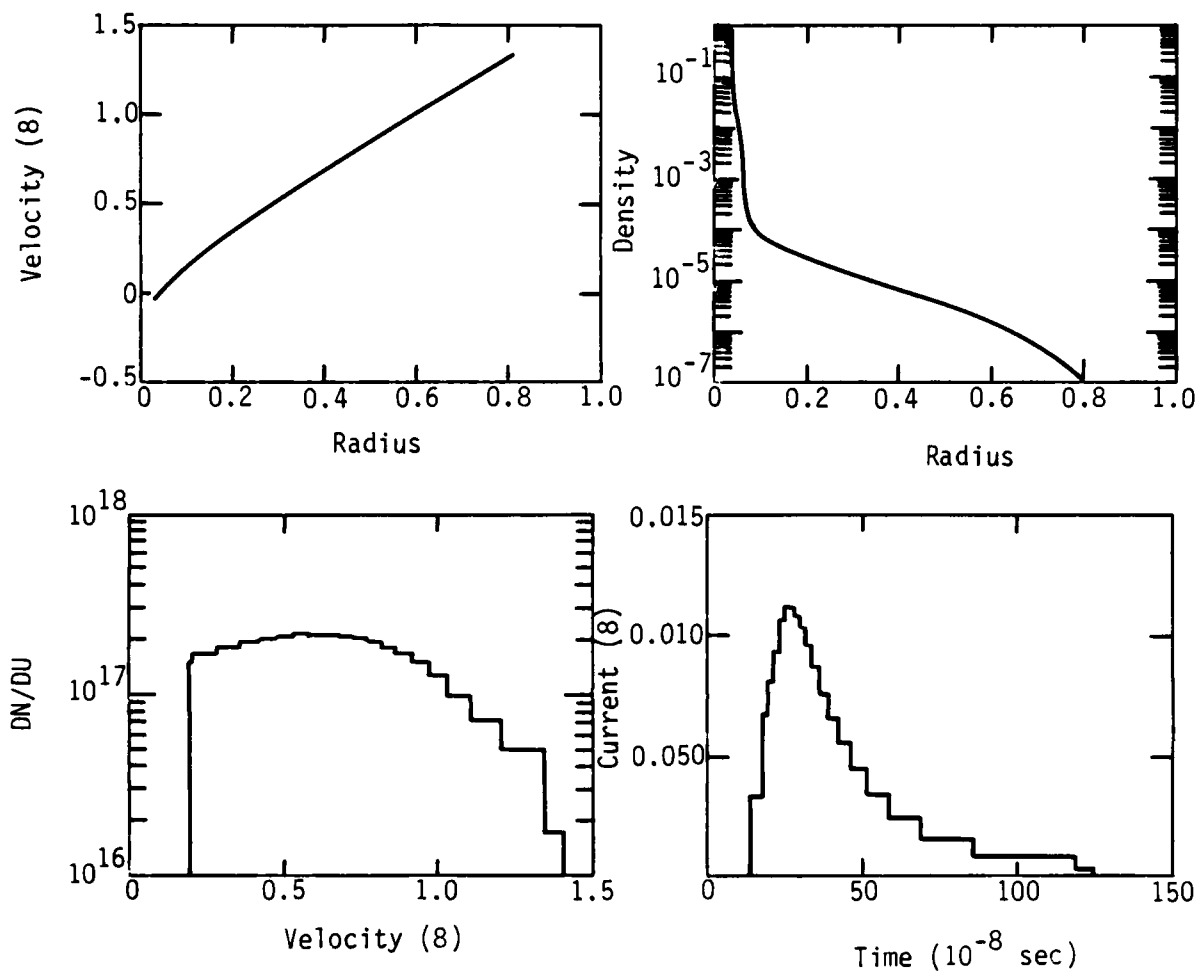
Figure 7-2. Velocity, density, velocity distribution function and ion
current for model U5-2 at time = 7 ns.
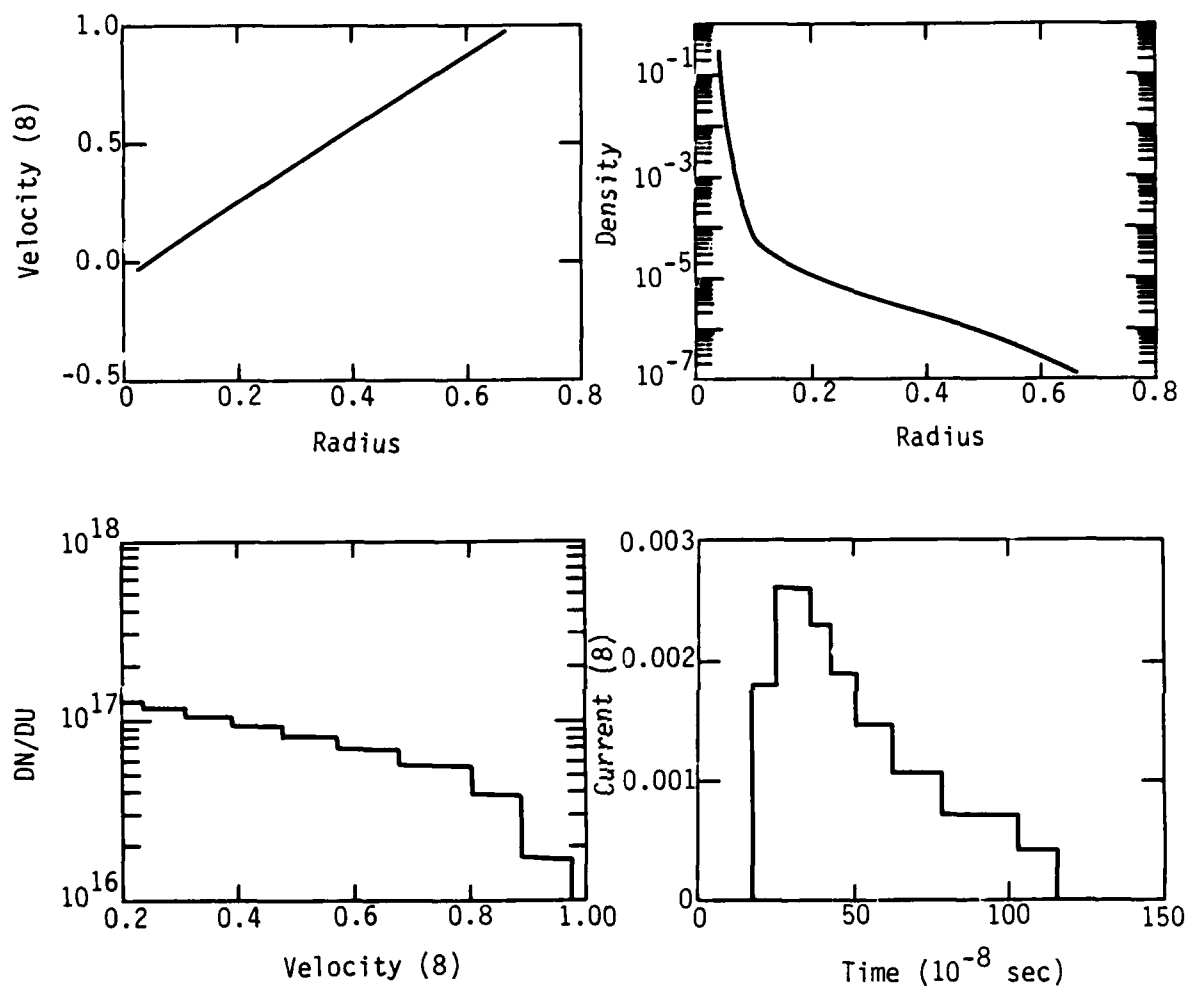
Figure 7-1. Velocity, density, velocity distribution function and ion current for model U5-1 at time = 7 ns.

TABLE 7-3.

Sequence U5: Power Law Scale Factors

$Q = \lambda(\text{Pulse Length})^\beta$, r = correlation coefficient (log)

Quantity	α	β	r
Absorption	0.82 ± .02	0.071 ± .02	0.87
KE fraction	0.76 ± .03	-0.083 ± .03	-0.81
RE fraction	0.17 ± .01	-0.20 ± .05	-0.91
Corona Mass	1.17E-6 ± 8E-8	0.45 ± .06	0.97
U ion peak*	0.46 ± .07	0.57 ± .1	0.93
U max*	1.20 ± .08	0.10 ± .06	0.70
Delta U/U	1.47 ± .2	-0.95 ± .1	-0.97
R crit	0.050 ± .003	-0.19 ± .05	-0.90
R outer	0.68 ± .07	-0.12 ± .09	-0.63
T max	0.096 ± .02	1.87 ± .2	0.98
T outer	0.082 ± .01	1.67 ± .1	0.99
ρ outer*	1.76E-7 ± 5E-8	0.59 ± .2	0.86

*These quantities show curvature in their logarithmic dependence on pulse length.

TABLE 7-1.

Sequence U5: Laser Pulse Length - Energy Variation

Model No.	E disk	R disk	P disk	E sphere	R sphere	P sphere
U5-1	0.15	0.0290	3.9E11	1.28	0.0490	3.3E12
U5-2	0.44	0.0290	3.9E11	3.76	0.0490	3.3E12
U5-3	0.88	0.0290	3.9E11	7.53	0.0490	3.3E12
U5-4	1.50	0.0290	3.9E11	12.8	0.0430	3.3E12
U5-5	2.00	0.0290	3.9E11	16.9	0.0430	3.3E12

TABLE 7-2.

Model Results for Sequence U5

	-1-	-2-	-3-	-4-	-5-
Run number	U5-1	U5-2	U5-3	U5-4	U5-5
*E laser (d)	0.15	0.44	0.88	1.50 kJ	2.00
Wavelength	1.06	1.06	1.06	1.06 mic	1.06
*Pulse length	0.34	1.0	2.0	3.4 ns	4.5
Target Z	13	13	13	13	13
Radius (d)	0.0290	0.0290	0.0290	0.0290 cm	0.0290
Divergence	80	80	80	80 deg	80
Intensity-ab	1.04E14	1.24E14	1.22E14	1.28E14	1.25E14
Absorption	0.73	0.87	0.86	0.90	0.88
KE fraction	0.79	0.79	0.77	0.69	0.62
RE fraction	0.19	0.18	0.16	0.13	0.11
Corona Mass	6.93E-7	1.19E-6	1.73E-6	2.29E-6 g	1.94E-6
U(ion peak)	0.20	0.60	0.80	0.91 (8)	0.85
U max	0.98	1.34	1.42	1.37 (8)	1.24
Delta U/U	4.0	1.33	1.07	0.38	0.35
R crit	0.0612	0.0554	0.0384	0.0385 cm	0.0409
R outer	0.6700	0.8083	0.7217	0.5770 cm	0.4800
T max	0.017	0.065	0.27	1.26 keV	1.79
T outer	0.017	0.065	0.19	0.75 keV	1.2
Rho outer	1.31E-7	1.14E-7	1.94E-7	3.76E-7 g/cc	6.14E-7

*Varied Quantities

steady (wind) flow solution (with a logarithimic variation of the velocity with radius) for the long pulse case (few ns or longer). This in turn produces a very broad spread in the velocity distribution for the short pulse case.

2. We find a very strong increase in the coronal temperature as the laser pulse length is increased. This is in part due to the energy variation but is mostly due to larger radiative losses for short pulses.

3. Laser absorption increases for longer pulses, although this effect evidently weakens above FWHM $\approx$ 3 ns. Overall, we have

$$\alpha_{INT} \propto FWHM^{0.1} \quad .$$

pure isothermal expansion using 1 ns pulses from the NRL glass laser facility. This is illustrated in Figure 7-1 through 7-5, in which the velocity and density structure of the five models in the current sequence are shown. We see a striking change from the pure linear increase in the velocity versus radius plot of model U5-1, to the strong steady-flow structure seen in the velocity of model U5-5. Also shown are the velocity distributions and the ion current traces for the five models. Here it is seen that a tendency toward a narrower velocity distribution is present, and that this tendency is clearly visible in the current trace. Again, this is a natural consequence of the change in flow character: the short pulses deposit their energy quickly relative to the expansion time, which is determined primarily by the laser intensity, and the expansion resembles an isothermal rarefaction wave. For the longer pulses, on the other hand, the deposition time is long compared to the expansion time, and the flow resembles a steady-state (wind) solution. The primary effect of this trend is the strong dependence of velocity distribution width on pulse length: shorter pulses produce a very broad spread in velocity.

Other effects visible in the figures of Table 7-3 are the coronal temperatures, which increase roughly as the square of the pulse length, thus compounding the timescale effect by lengthening the expansion timescale for the shorter pulse lengths. The reason for this trend seems to be radiative losses from the rather thin envelopes generated in the short pulse cases.

7-3   SUMMARY OF PULSE LENGTH EFFECTS.

The most important effects seen as a result of varying the laser pulse length are:

1. The character of the flow changes strongly from that of an isothermal rarefaction expansion (with a linear increase of the velocity with radius) in the case of a short pulse (1 ns or less), to that of a

71

SECTION 7

LASER PULSE LENGTH EFFECTS

In this section we evaluate the effects of varying the length of
the laser pulse. We will show that shortening the pulse length has the
effect of producing a target expansion that tends toward isothermal rare-
faction expansion, and lengthening the laser pulse tends to produce
steady-flow flow structure.

7-1   MODELS IN SEQUENCE U5.

A sequence of five models were constructed with pulse lengths
varying from 0.34 ns to 4.5 ns. The pulse shapes were not varied, and the
peak laser intensity for each run is the same. Therefore, the total laser
energy does vary from model to model. This simulates a series of shots in
which the pulse length is varied by interrupting (chopping) the beam for
different periods of time. The model parameters used are given in Table
7-1, and the results are summarized in Table 7-2. All models are evaluated
at time = 7 ns as normally done. This affects the last model (U5-5), whose
energy is not completely deposited at this time, but most quantities have
stabilized to sufficient accuracy. Table 7-3 lists the parameters of the
regression fits to the logarithimic variation of all of the diagnostic
parameters.

7-2   PULSE LENGTH EFFECTS.

The expected effects of varying the laser pulse length were
thoroughly discussed in Reference 1 (Stellingwerf, Longmire and Alme 1983)
in connection with a comparison of CO_2 and glass lasers used for HANE simu-
lations (see Figure 5-3 of Ref. 1). The present series of models shows
that it is possible to produce coronal flow structure approaching that of a

MODEL U4C-1
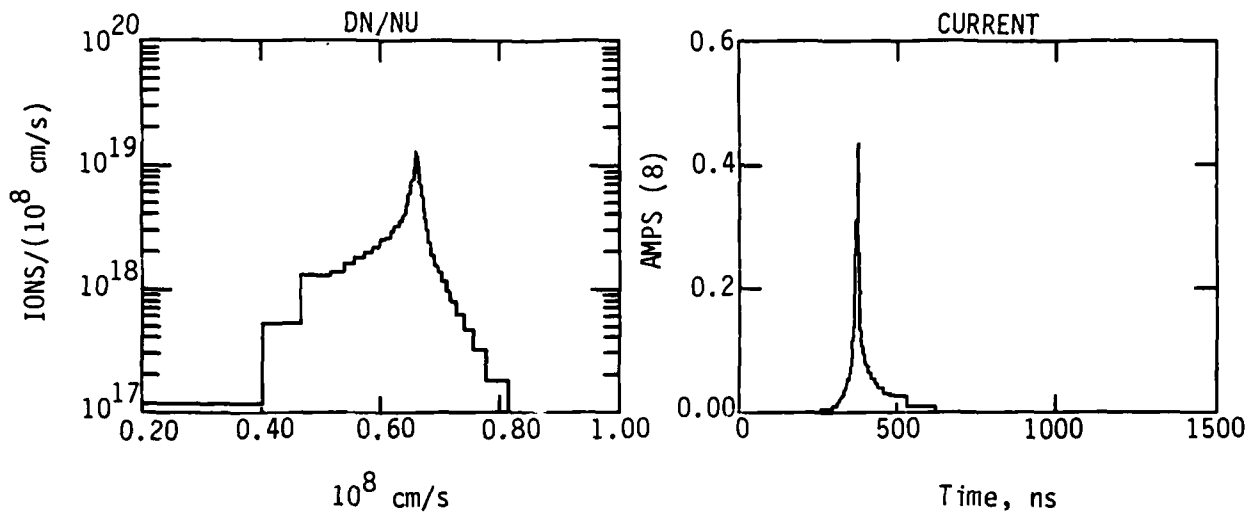
MODEL U4C-4
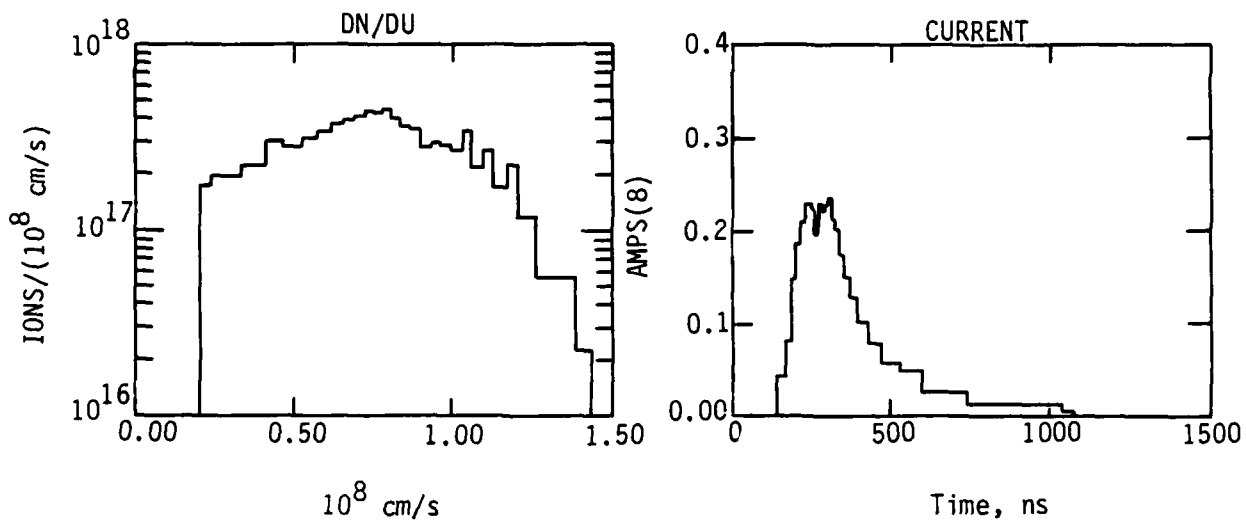
Figure 6-3. Comparison of ion velocity distribution and ion current detected
25 cm from the target for models U4C-1 (λ = 0.25 μm) and
U4C-4 (λ = 2.5 μm).

69
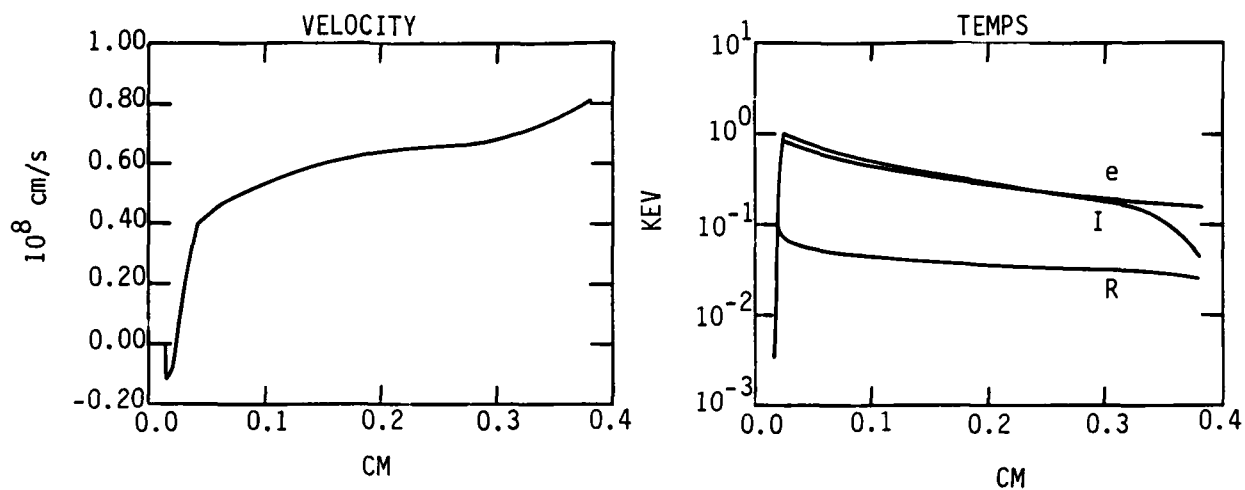
MODEL U4C-1

MODEL U4C-4
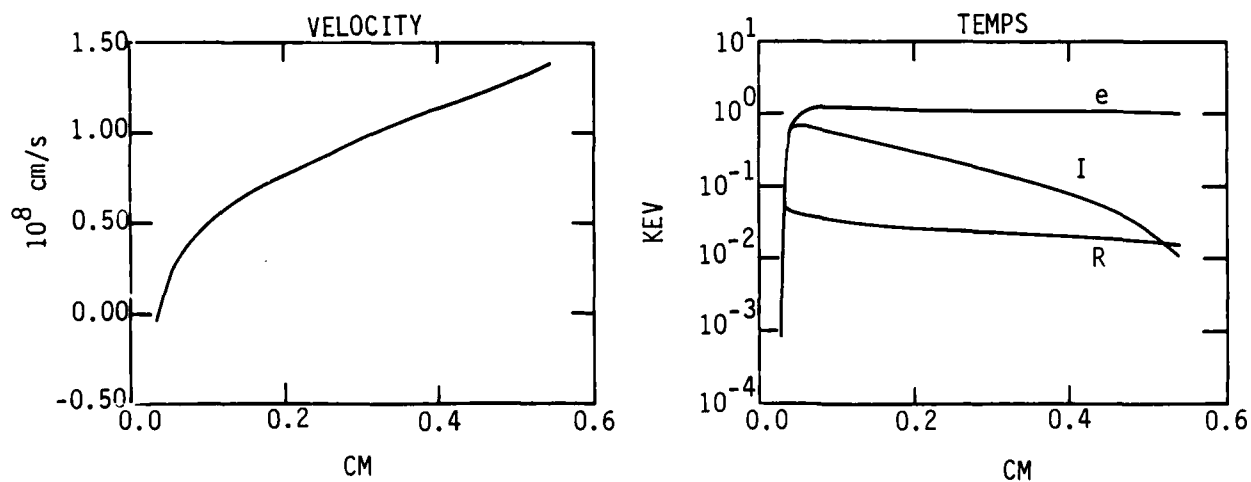
Figure 6-2. Comparison of velocity and temperature structure for models
U4C-1 (λ = 0.25) and U4C-4 (λ = 2.5 μm).

68

MODEL U4-1

MODEL U4-4
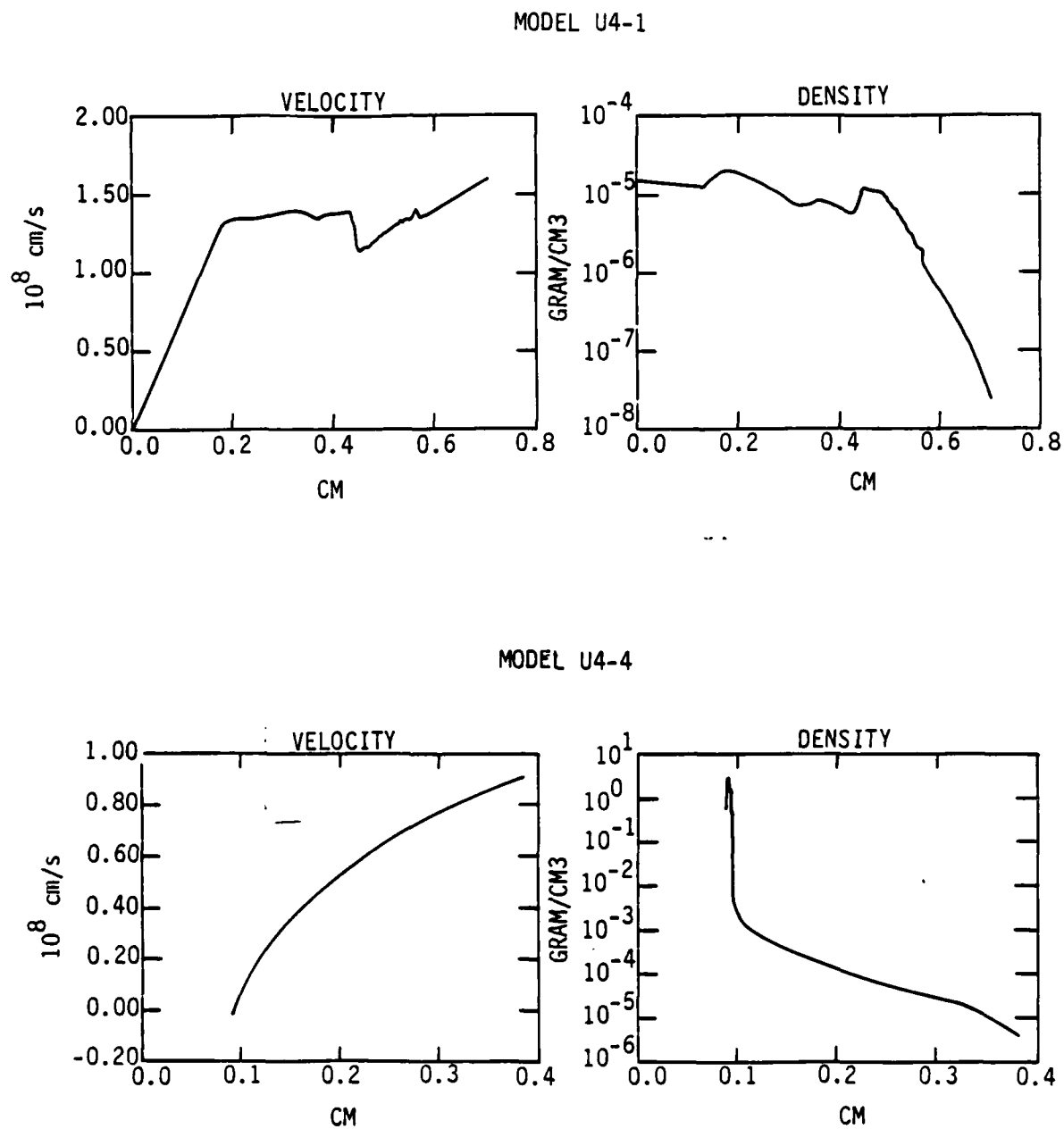
Figure 6-1. Comparison of velocity and density profiles versus radius for models U4-1 (λ = 0.25, top) and U4-4 (λ = 2.5, bottom) at time = 7 ns.

67

TABLE 6-8.

Sequence U4C: Power Law Scale Factors

$$Q = \alpha \lambda^{\beta}, \ r = \text{correlation coefficient}$$

Quantity	α	β	r
Absorption	0.832 ± .04	-0.162 ± .05	-0.90
KE fract	0.657 ± .02	0.014 ± .03	0.29
RE fract	0.149 ± .01	-0.253 ± .07	-0.92
Corona Mass	2.26E-6 ± 4E-8	-0.461 ± .02	-1.00
U ion peak*	0.781 ± .06	0.063 ± .08	0.49
U max*	1.220 ± .07	0.231 ± .07	0.93
Delta U/U	0.310 ± .03	1.395 ± .09	1.00
R crit	0.043 ± .003	0.575 ± .09	0.98
R outer	0.545 ± .04	0.074 ± .08	0.55
T max	1.20 ± .03	0.114 ± .02	0.96
T outer*	0.586 ± .06	0.815 ± .1	0.98
Rho outer	5.59E-7 ± 1E-7	-0.851 ± .2	-0.93

*These quantities show curvature in their logarithmic dependence on λ.

SECTION 8

TARGET MATERIAL EFFECTS

In this section the effects of varying the target material are discussed. It will be shown that the primary effect of target material in the range Z = 4-26 is a strong increase in radiated energy loss as Z is increased.

8-1   MODELS IN SEQUENCE U6.

Four models were computed in this sequence, with the target materials beryllium (Z=4), carbon (Z=6), aluminum (Z=13) and iron (Z=26). High Z materials were not investigated in this survey. Model U6-3 is model UO, and all parameters except material were held fixed for the other models in the sequence. The results are given in Table 8-1 in the standard format (evaluated at 7 ns), and power law fits to this data are summarized in Table 8-2. These results can be compared to previous analyses discussed in Reference 1 (Stellingwerf, Longmire and Alme, 1983) in which a lower laser energy regime was explored. In that study, significant differences in absorption, flow structure, temperature, and flow velocity were found for different Z models.

8-2   RESULTS.

We find that at higher laser energy the effects of varying target material are not as pronounced as found in the 200 Joule energy range. The characteristics of the two extreme models U6-1 and U6-4 are shown in Figures 8-1 and 8-2. The characteristics found at low energy are visible: higher electron temperature and lower coupling between electron and ion temperatures at low Z, more extensive outer rarefaction region at low Z, broader velocity distribution at low Z. In each case, however, the effect

is weaker at these higher laser energies. Examination of Table 8-2 shows that the main strong correlation is that of the Radiated Energy Fraction, which increases sharply as target Z is increased, reaching 41% of the absorbed energy for the iron target. The increased radiative losses tend to lower the outer temperatures and velocities, while increasing the outer density. These effects then explain the other differences. Another effect of this energy loss is that the total mass in the corona decreases as the target Z increases.

8-3   SUMMARY OF TARGET MATERIAL EFFECTS.

The primary effect of increasing target Z is:

1. Radiative energy losses increase from 2% of the absorbed energy at Z=4 to 41% of the absorbed energy at Z=26.

This induces the following secondary effects:

2. Coronal mass decreases,

3. Outer temperatures and velocities decrease, outer density increases,

4. Electron/ion coupling is stronger, and

5. Ion velocity distribution width is slightly narrower.

These secondary effects are weaker in the present energy range than in previous models at lower laser energy.

TABLE 8-1.

Model Results for Sequence U6

	-1-	-2-	-3-	-4-
Run number	U6-1	U6-2	U6-3	U6-4
E laser (d)	1.50	1.50	1.50 ku	1.50
Wavelength	1.06	1.06	1.06 mic	1.06
Pulse length	3.4	3.4	3.4 ns	3.4
*Target Z	4	6	13	26
Radius (d)	0.0290	0.0290	0.0290 cm	0.0290
Divergence	80	80	80 deg	80
Intensity-ab	1.16E14	1.25E14	1.28E14	1.15E14
Absorption	0.82	0.88	0.90	0.81
KE fraction	0.78	0.77	0.69	0.45
RE fraction	0.02	0.04	0.13	0.41
Corona Mass	2.83E-6	2.55E-6	2.29E-6 g	1.59E-6
U(ion peak)	0.80	0.85	0.91 (8)	0.81
U max	1.27	1.39	1.37 (8)	0.97
Delta U/U	0.38	0.47	0.38	0.25
R crit	0.0338	0.0287	0.0385 cm	0.0399
R outer	0.5507	0.5950	0.5770 cm	0.3649
T max	1.16	1.26	1.26 keV	1.13
T outer	0.77	0.84	0.75 keV	0.34
Rho outer	4.49E-7	3.40E-7	3.76E-7 g/cc	3.47E-6

*Varied Quantities

82

TABLE 8-2.

Sequence 6: Power Law Scale Factors

$$Q = \alpha Z^\beta, \; r = \text{correlation coefficient (log)}$$

Quantity	α	β	r
Absorption	0.87 ± .03	-7.5E-3 ± .04	-0.12
KE fraction	1.24 ± .09	-0.28 ± .09	-0.91
RE fraction	2.2E-3 ± 4E-5	1.60 ± .02	1.00
Corona Mass	4.34E-6 ± 2E-7	-0.29 ± .06	-0.96
U ion peak*	0.82 ± .03	0.012 ± .05	0.17
U max*	1.69 ± 0.1	-0.14 ± .1	-0.69
Delta U/U*	0.63 ± .07	-0.25 ± .1	-0.79
R crit	0.026 ± .002	0.14 ± .08	0.76
R outer	0.82 ± .08	-0.21 ± .1	-0.76
T max*	1.25 ± .04	-0.018 ± .05	-0.27
T outer*	1.64 ± .3	-0.42 ± .2	-0.83
ρ outer*	6.59E-8 ± 4E-8	1.03 ± .6	0.77

*These quantities show curvature in their logarithmic dependence on Z.
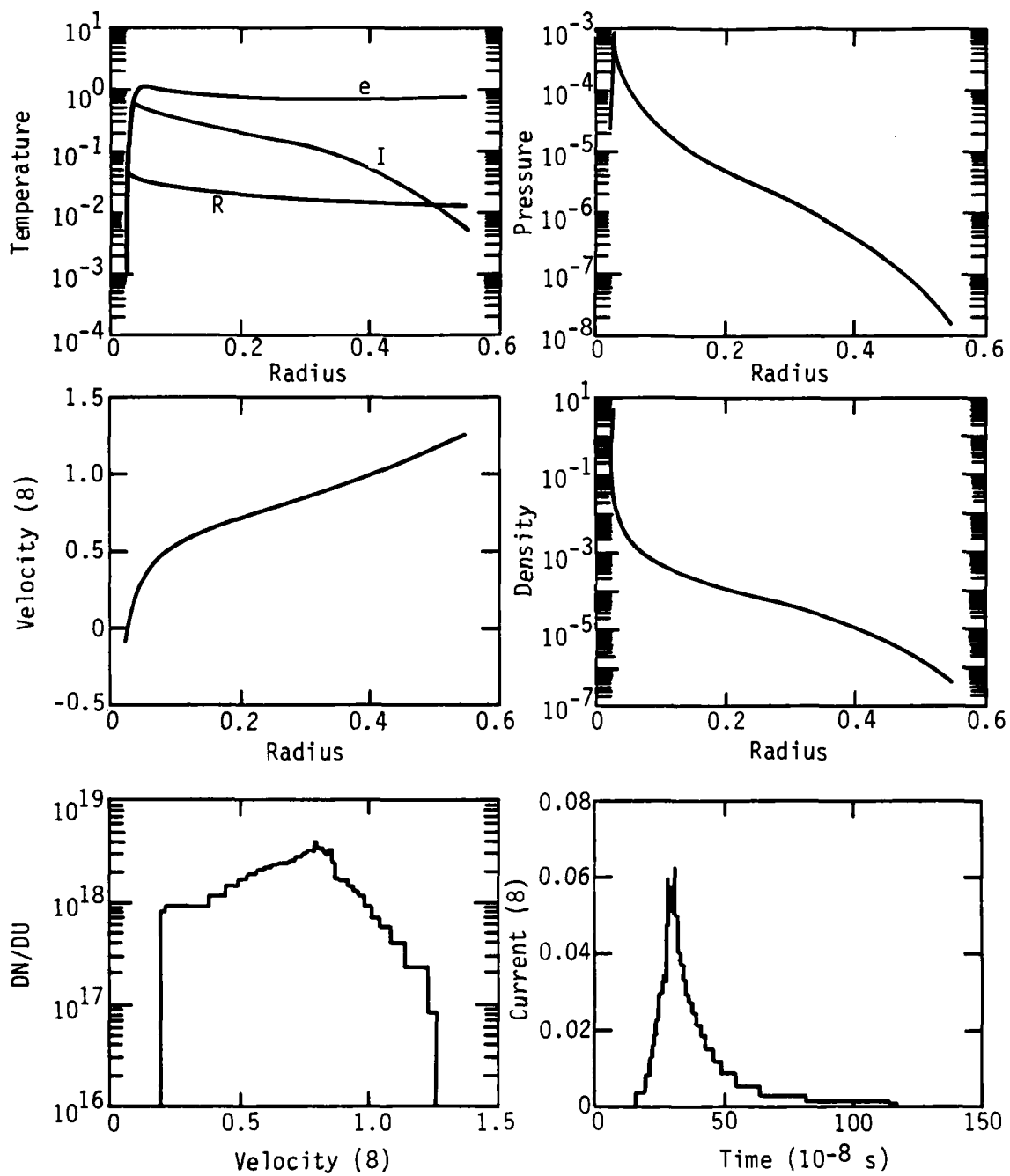
83

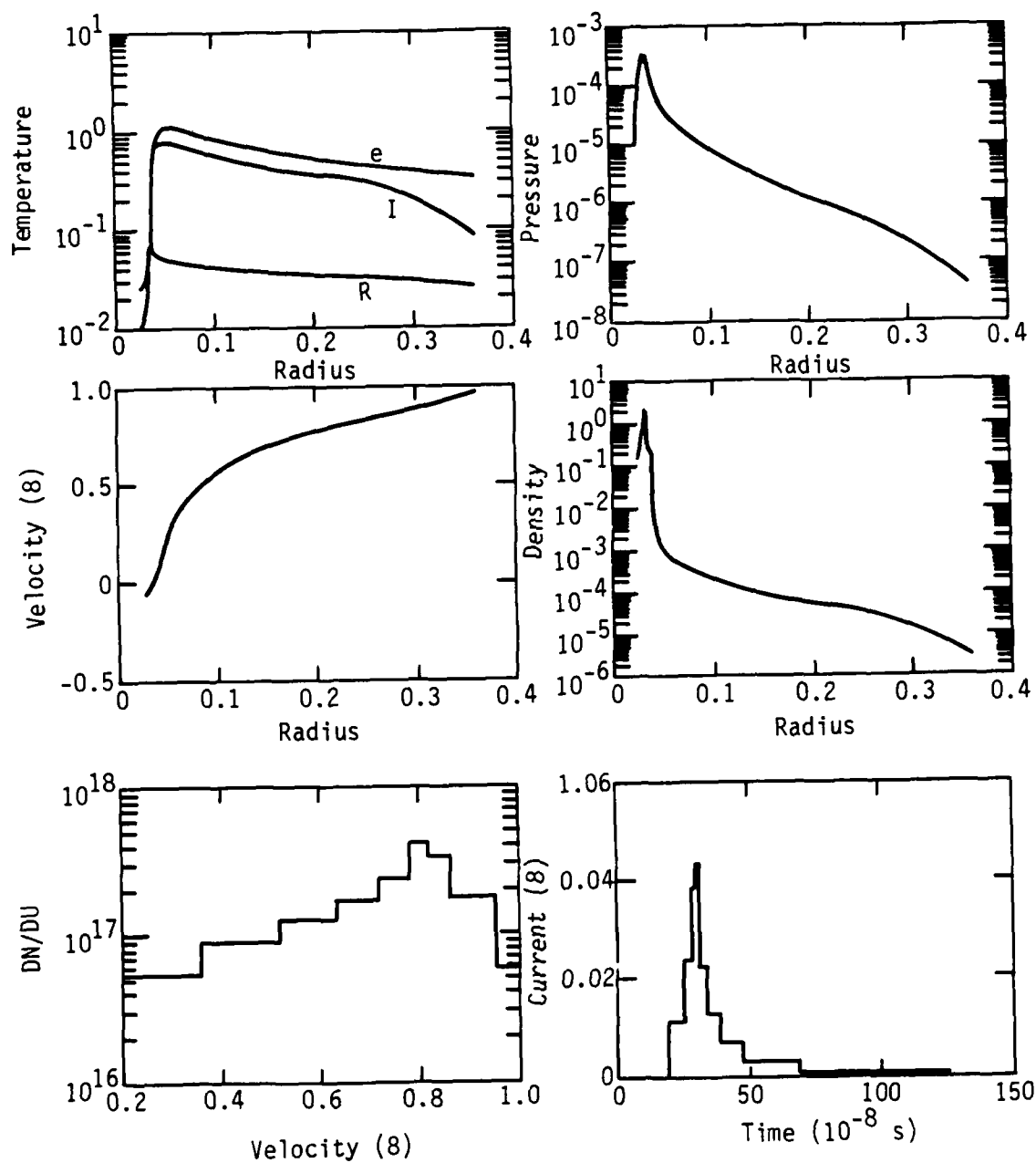Figure 8-1. Characteristics of Model U6-1 at time = 7 ns.

84

Figure 8-2. Characteristics of Model U6-4 at time = 7 ns.

SECTION 9

LOW POWER MODELS

Irradiation at low power and somewhat lower intensities is a technique employed to reduce the interaction lengths in possible HANE coupling mechanisms. Extensive experimental shots of this type were undertaken at NRL in late 1982 to explore this regime.[4] In this section, we briefly discuss a series of models computed in support of the analysis of the resulting data. The models discussed here were all computed with 23 J laser energy. Three aluminum targets and two carbon targets of varying sizes comprise sequence L1.

9-1   MODELS IN SEQUENCE L1.

Table 9-1 summarizes the model parameters. Model L1-1 is the same model as U1-1. Models L1-2 and L1-3 increase the disk radius from 41 microns to 115 and 364 microns, lowering the intensity on target from about 10^{14} W/cm^2 to 10^{13} and 10^{12}. Models L1-2C and L1-3C are identical to the two previous models, but with carbon targets.

The full summary of model parameters and results at t = 7 ns is given in Table 9-2. The dependence of these quantities on intensity is shown in Figures 9-1 through 9-7, and the power law fits to this data are given in Table 9-3. This table is intended only to be a rough guide to compare with the other model sequences. The two Z values and small number of intensity points reduce the reliability of the fit parameters in many cases, as indicated by the error bars.

9-2   MODEL RESULTS.

Figure 9-1 shows that at these low laser powers, the absorption decreases slowly from 85% to 60% as intensity increases, independent of

target material. The kinetic energy fraction, however, increases from 50% to 75% for the aluminum target, and gains about 15% for the carbon targets, whose radiated losses are lower.

Figure 9-2 shows a strong dependence of target temperature (T_{max}) on intensity. Table 9-3 shows $T_{max} \propto I_{ab}^{0.3}$. This is expected on simple energy balance grounds ($T_{max} \propto I_{ab}^{2/7}$ predicted, see Section 4), and is consistent with earlier models[1] and with experiments. The outer temperature (outer edge of expanding corona) increases to about 130 eV at $I = 10^{13}$ W/cm^2, and remains constant at higher intensities. The coronal temperature shows only a weak dependence on target Z.

The increasing coronal temperatures produce higher coronal velocities, as shown in Figure 9-3. We have $U \propto I^{0.2}$, with velocities in the range 3 - 7 x 10^7 cm/sec. These higher velocities in turn produce larger debris radii at higher intensities, as seen in Figure 9-4, which also shows that the critical surface at 7 ns is always about 50% larger than the initial disk target radius. The net result of this trend is sharply reduced debris densities at higher intensities, as seen in Figure 9-5, with $\rho_{outer} \propto I_{ab}^{-1.3}$.

The higher velocity expansion at higher intensities into a lower density corona tends to produce a narrower ion velocity distribution, as seen in Figure 9-6. Both the aluminum and carbon targets show relatively narrow distribution above 10^{13} W/cm^2, but broad distribution at 10^{12} W/cm^2.

Finally, Figure 9-7 shows the coronal mass decreasing at higher intensities, due mainly to smaller target mass.

Target dependence on intensity and material at higher power is discussed in Sections 4 and 8.

Figure 9-8 shows the structure and radiation spectrum of model L1-2C at 7 ns. For this model, peak debris kinetic energy occurs at $U = 5 \times 10^7$ cm/s, which is also the peak of the ion velocity distribution. It is the flattening of the velocity curve at this point that is responsible for the narrow range of ion velocities produced. We note that the electron and ion temperatures remain comparable except at the outer edge of the corona. Compare with the model L1-1 velocity curve shown in Figure 3-8a, which shows an actual dip in the velocity versus radius, characteristic of high intensity runs.

An important experimental diagnostic is the ion current arriving at a charge collector as a function of time. Figures 9-9 and 9-10 show the model current traces (collector at 25 cm from target, scale arbitrary) for models L1-2C and L1-3C. Also shown are experimental traces for similar shots of carbon targets. The shapes and widths agree well with the models.

TABLE 9-1.

Sequence L1: Low Energy Models

Model No.	E disk	R disk	P disk	E sphere	R sphere	P sphere
L1-1	0.023	0.0041	5.9E09	0.20	0.0060	5.1E10
L1-2	0.023	0.0115	5.9E09	0.20	0.0168	5.1E10
L1-3	0.023	0.0364	5.9E09	0.20	0.0532	5.1E10
L1-2C	0.023	0.0115	5.9E09	0.20	0.0168	5.1E10
L1-3C	0.023	0.0364	5.9E09	0.20	0.0532	5.1E10

TABLE 9-2.

Model Results: Low Energy Sequence L1

	-1-	-2-	-3-	-4-	-5-
Run number	L1-1	L1-2	L1-3	L1-2C	L1-3C
E laser (d)	0.023 kJ	0.023	0.023	0.023	0.023
Wavelength	1.06 μm	1.06	1.06	1.06	1.06
Pulse length	3.4 ns	3.4	3.4	3.4	3.4
Target Z	13	13	13	6	6
*Radius (d)	0.0041 cm	0.0115	0.0364	0.0115	0.0364
Divergence	80 deg	80	80	80	80
*Intensity-ab	6.70E13 W/cm^2	1.12E13	1.21E12	1.10E13	1.23E12
Absorption	0.59	0.78	0.85	0.77	0.86
KE fraction	0.77	0.65	0.49	0.81	0.68
RE fraction	0.13	0.17	0.18	0.03	0.05
Corona Mass	4.60E-8 g	1.05E-7	2.64E-7	1.20E-7	3.31E-7
U(ion peak)	0.69 (8) cm/s	0.48	0.28	0.51	0.31
U max	0.81 (8) cm/s	0.56	0.34	0.64	0.40
Delta U/U	0.09	0.10	0.54	0.15	0.53
R crit	0.0071 cm	0.0172	0.0547	0.0151	0.0523
R outer	0.3567 cm	0.2300	0.1670	0.2700	0.1870
T max	0.52 keV	0.35	0.17	0.33	0.16
T outer	0.13 keV	0.13	0.10	0.13	0.08
Rho outer	3.78E-8 g/cm^3	8.10E-7	9.64E-6	3.52E-7	6.93E-6

*Varied Quantities

TABLE 9-3.

Sequence L1: Power Law Scale Factors

$$Q = \alpha I_{ab}^{\beta} \quad , \quad r = \text{correlation coefficient (log)}$$

QUANTITY	α	β	r
Absorption*	$8.84 \pm .3$	$-0.083 \pm .02$	-0.93
KE fraction	$0.066 \pm .006$	$0.078 \pm .05$	0.67
RE fraction	$0.030 \pm .02$	$0.04 \pm .3$	0.08
Corona Mass	$0.106 \pm .06$	$-0.46 \pm .03$	-0.99
U(ion peak)/10^8	$7.13\text{E-}4 \pm 2\text{E-}5$	$0.22 \pm .02$	0.99
U max/10^8	$1.39\text{E-}3 \pm 7\text{E-}5$	$0.20 \pm .03$	0.97
$\Delta U/U$*	$3.92\text{E}5 \pm 8\text{E}4$	$-0.49 \pm .1$	-0.94
R_{crit}	$8.03\text{E}4 \pm 3\text{E}3$	$-0.51 \pm .02$	-1.00
R_{outer}	$1.48\text{E-}3 \pm 6\text{E-}5$	$0.17 \pm .02$	0.97
T_{max} (keV)	$4.61\text{E-}5 \pm 2\text{E-}6$	$0.30 \pm .02$	0.99
T_{outer} (keV)	$4.58\text{E-}3 \pm 3\text{E-}4$	$0.11 \pm .04$	0.84
ρ_{outer}	$7.9\text{E}10 \pm 2\text{E}10$	$-1.32 \pm .1$	-0.99

*These quantities show curvature in their dependence on I_{ab}. See Table
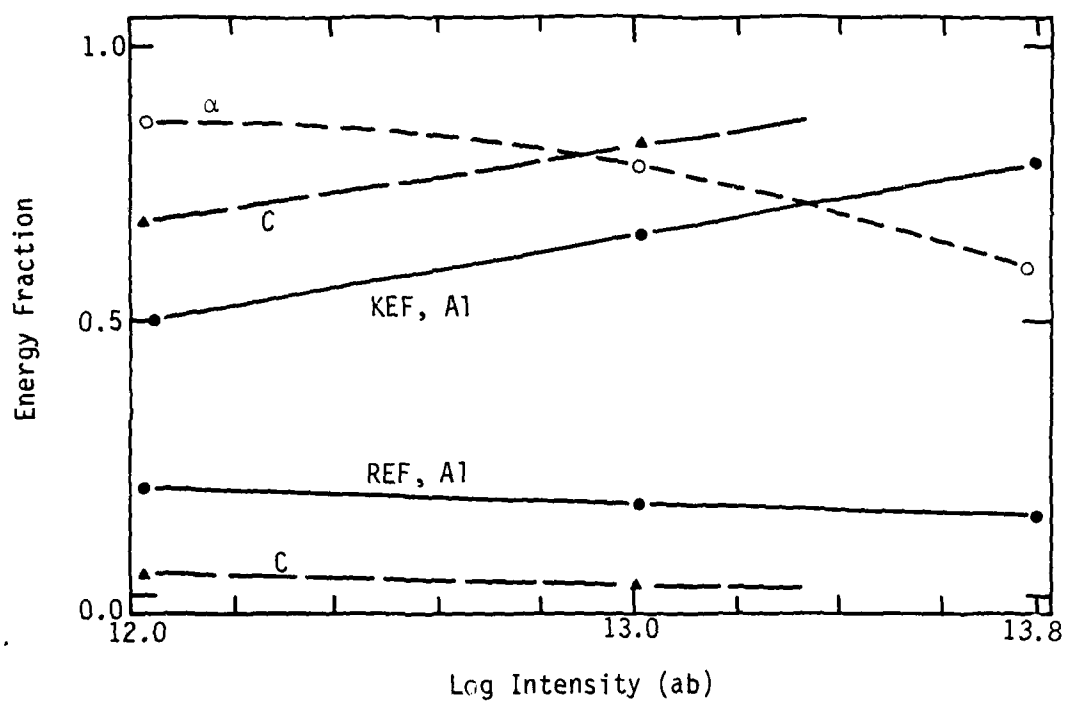9-2 and figures for the nature of the relation.

Figure 9-1. Integrated absorption fraction (α), kinetic energy fraction, and radiated energy fraction for Al and C models.

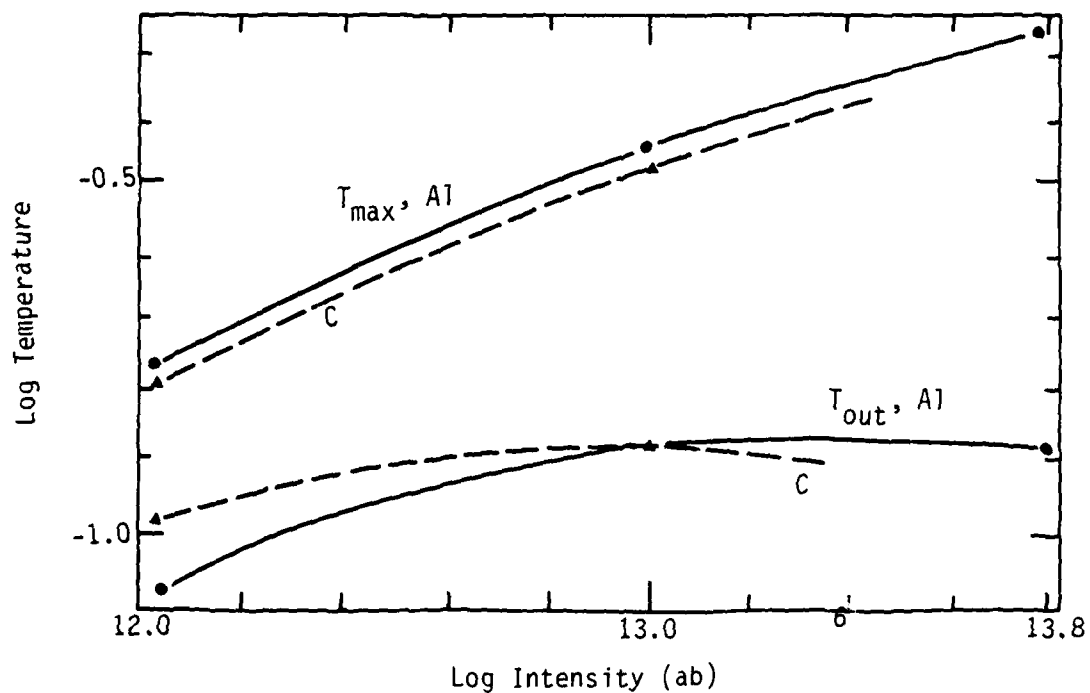Figure 9-2. Maximum and outer coronal temperatures for Al and C models.
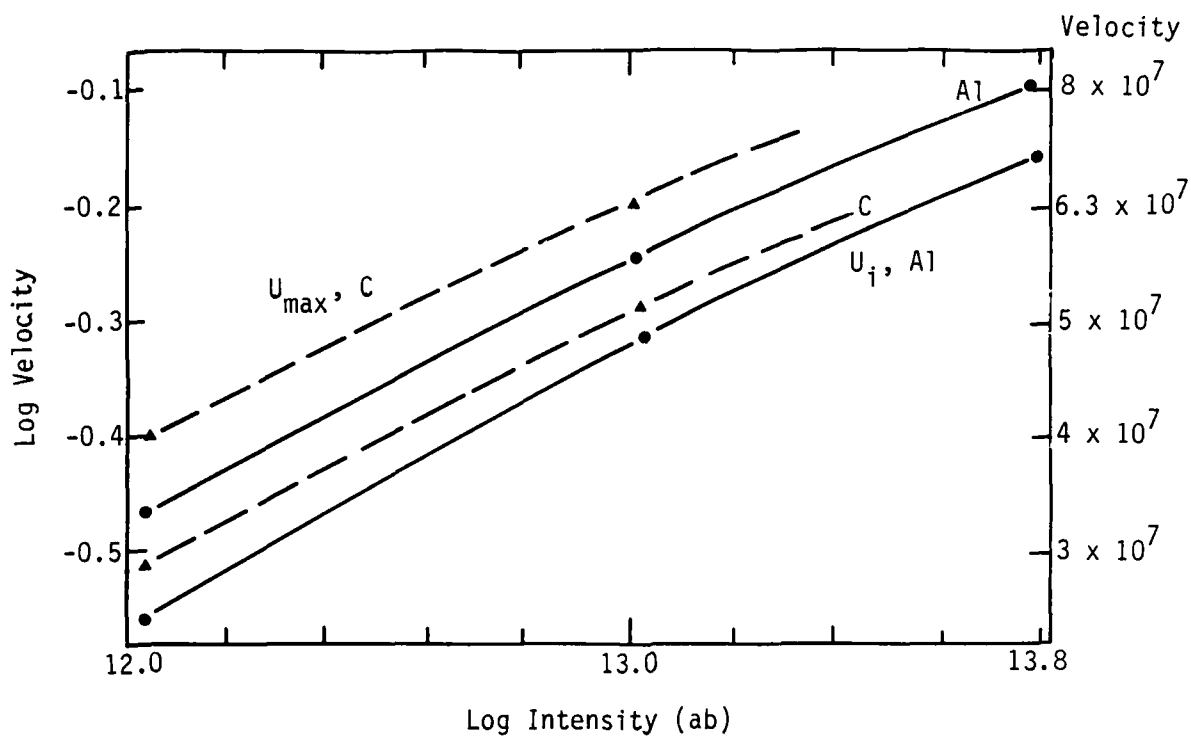
Figure 9-3. Velocity at the ion distribution peak, U_i, and maximum coronal velocity for Al and C models.
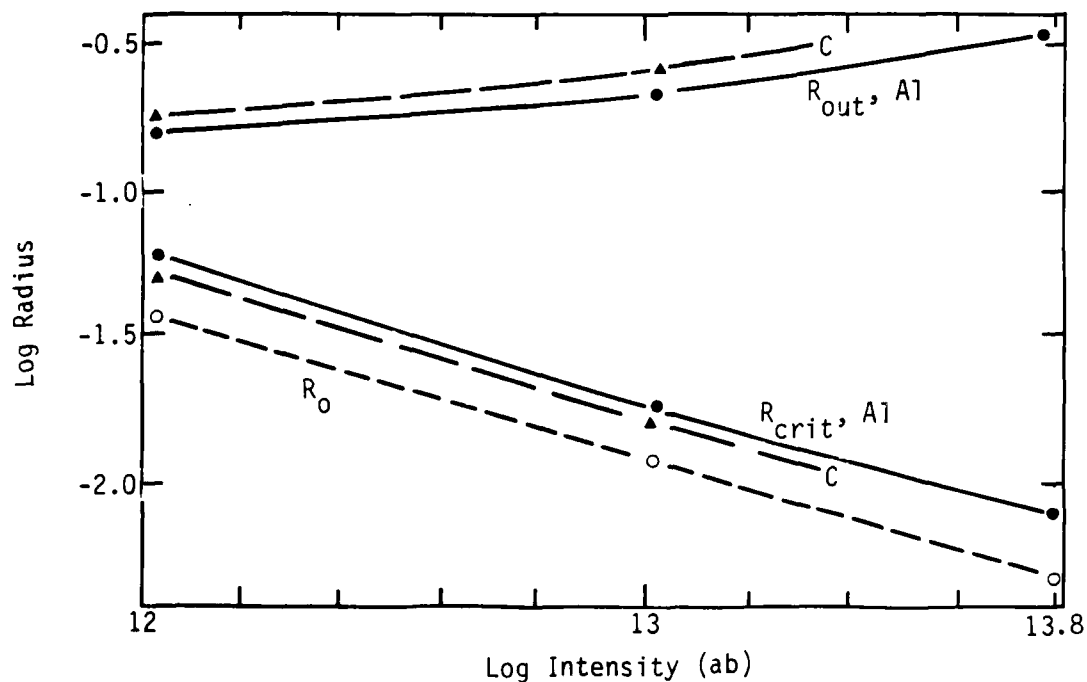
Figure 9-4. Outer radius, critical radius and disk target radius for Al and C models.
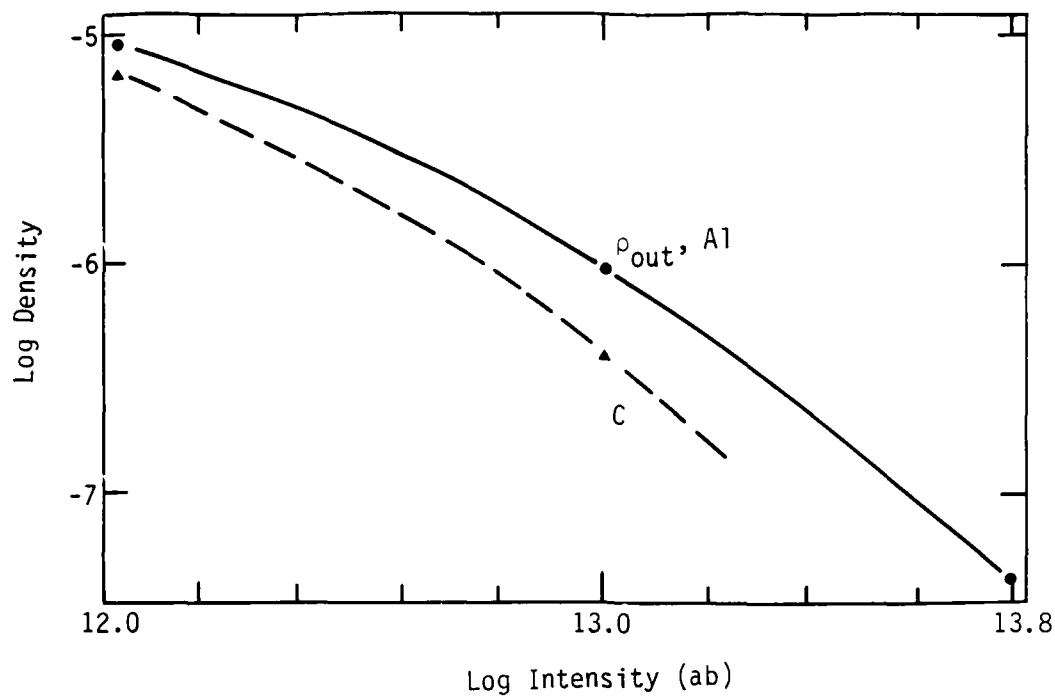
Figure 9-5.   Outer density for Al and C models.
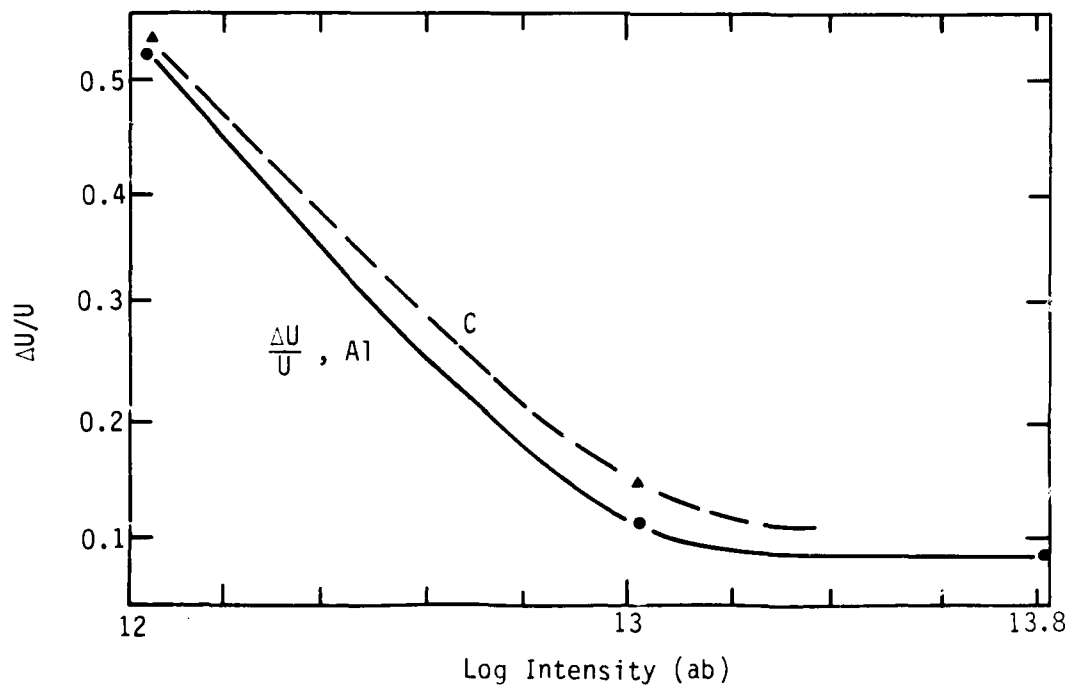
Figure 9-6.   Velocity distribution width for Al and C models.

END
FILMED
DTIC

						1.0			2.8		2.5
									3.2		2.2
									3.6		
						1.1			4.0		2.0
											1.8
						1.25		1.4			1.6

MICROCOPY RESOLUTION TEST CHART
NATIONAL BUREAU OF STANDARDS-1963-A
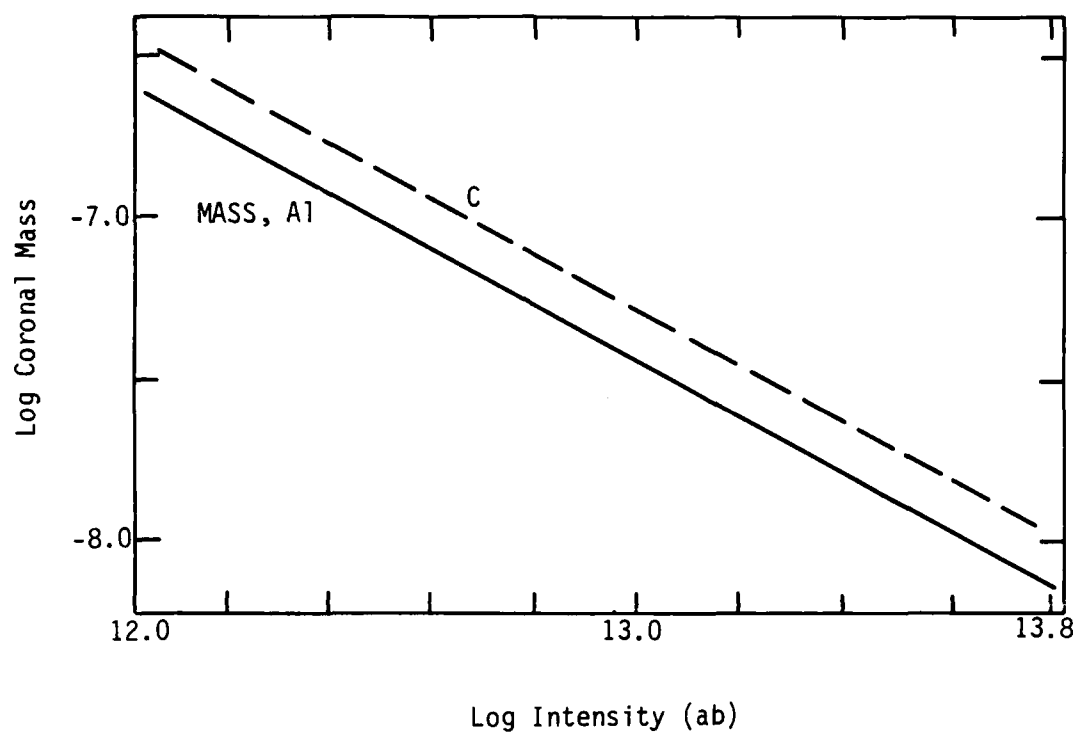
Figure 9-7.   Coronal mass for Al and C models.
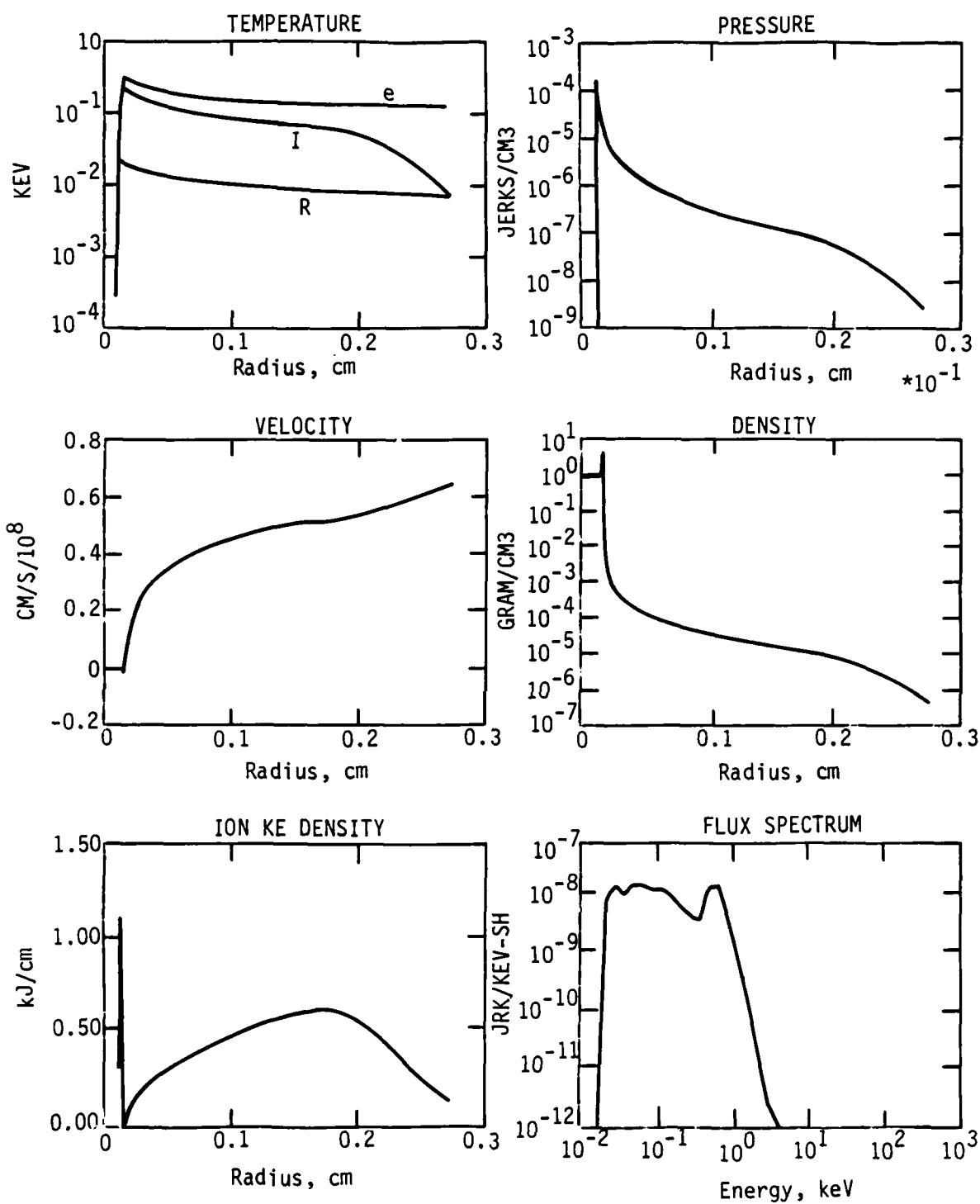
Figure 9-8.   Structure of model L1-2C at 7 ns, and its radiation spectrum.
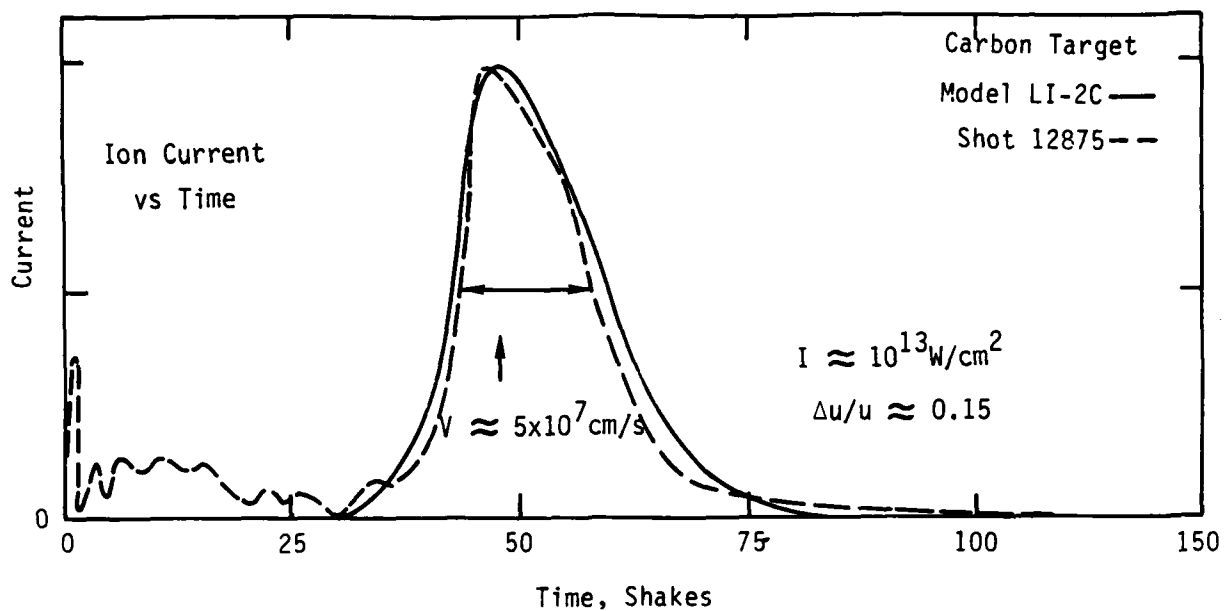
Figure 9-9. Ion current versus time for model L1-2C, and comparison with experiment.
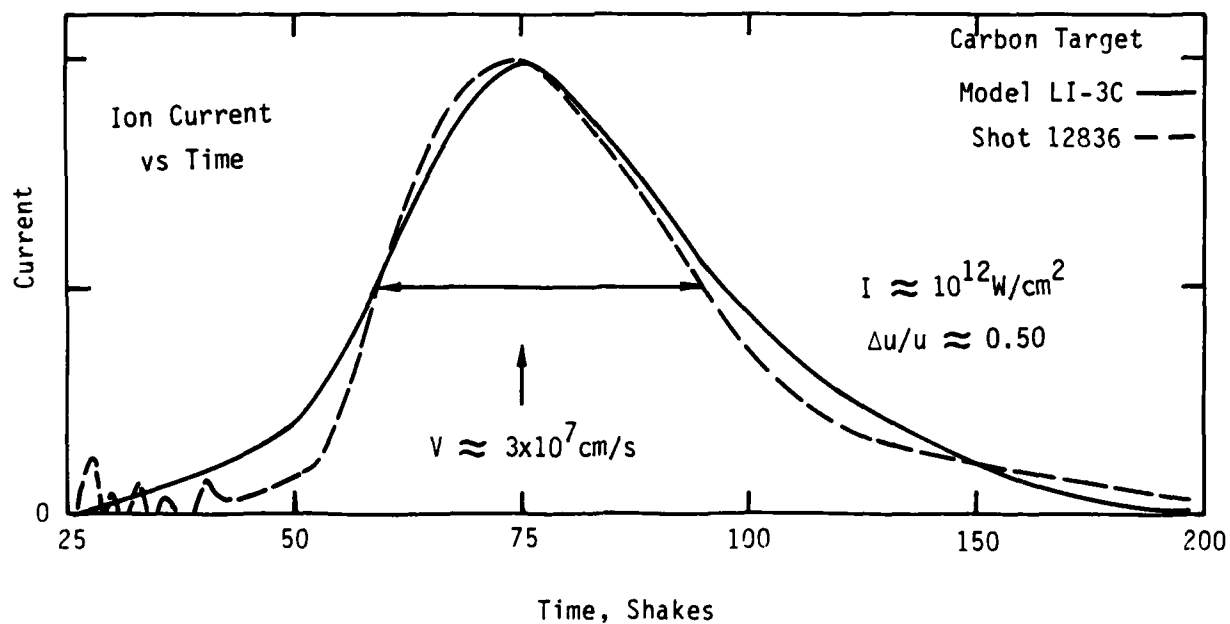
Figure 9-10. Ion current versus time for model L1-3C, and comparison with experiment.

SECTION 10

MULTIVARIATE SCALING LAWS FOR ALL SEQUENCES

In this section all of the data obtained in the "upgrade" (U)
sequences are combined and analyzed for functional relationships. Power
law scaling is obtained for all twelve monitored quantities as functions of
laser intensity, laser energy, wavelength, pulse length, and target
material.

10-1   THE COMBINED MODEL SEQUENCES.

All of the "U" sequences were combined for the present analysis.
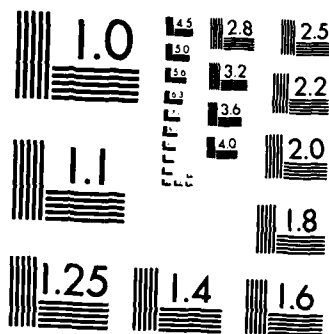The low energy models discussed in Section 9 were omitted, as were dupli-
cate models in different sequences. This resulted in twenty-five unique
models with a variety of model parameters.

The selection of independent variables varies slightly from the
analysis given in Section 5-2 of Reference 1, in which scaling laws were
derived for lower energy models. Here we select the variables.

1. I = Absorbed laser intensity (see Section 2-3),
2. E = laser energy,
3. λ = laser wavelength,
4. FW = laser pulse length, and
5. Z = target Z.

We choose both laser intensity and laser energy as independent
variables because these two quantities are indeed treated independently in
this survey. We wish to know the effects associated with increasing the
laser energy at constant intensity, and in Section 3 it is shown that
important energy effects do exist. In addition, we desire to predict the
overall effects of varying the laser intensity. In Reference 1, the

97

variables could be taken to be intensity and target radius, but in the present survey intensity and energy are more appropriate variables.

10-2   ANALYSIS TECHNIQUE.

The present analysis consists of a stepwise multiple regression computation relating each of the twelve "below the line" quantities to the five variables listed above. This analysis consists of a determination of which of the five variables (if any) accounts for the largest significant portion of the observed variation in the dependent variable. The computation is carried out in the logarithm of the quantities. A least-squares fit is made, and the effect of the most significant variable is removed. A test is then performed to see if the addition of an additional variable to the relation will improve the fit. If so, a new two-variable fit is calculated. This procedure is repeated until no further significant dependence is found. At every stage of the computation a test is also performed to determine if the fit can be improved by dropping a previously included variable (this never happened in the present analysis). The results of this procedure consists of a sequence of multivariate fits to the data for each dependent variable. The criteria used to determine if a given fit is significantly better than the preceding fit involves the evaluation of an "F" statistic (a ratio of variances), whose value must exceed 4 for 0.01 confidence level with this data set. This means that there is only a 1% chance that the relationships given below are due to random fluctuations.

The overall results of this analysis are given in Table 10-1, which includes all fits obtained with F values of 4 or greater. The larger the F value, the more variance is accounted for by a given variable. Table 10-1 includes the F values actually obtained for each variable in each fit, so stronger (and therefore more reliable) dependences can be easily identified. In addition, error estimates are provided for each of the exponents, and these correlate in the sense that the more significant the fit, the more accurately the exponent is determined.

In addition to these general fits, Table 10-2 lists four fits that are considerably stronger than average. The exponents differ from those in Table 10-1 since a different stage in the fitting process is used in this case. Finally, Table 10-3 gives a list of the first step in each of the fits: this is the strongest single variable fit in each case and corresponds to the fits given in earlier sections, except that here the full set of variables is used in the analysis. The single variable analysis is sometimes called a "partial correlation analysis". If several variables contribute strongly to the variation of a given quantity, then the multivariate coefficients could differ significantly from the single variable fits.

An additional diagnostic parameter, the ablation pressure, P_{ab}, has been added for this analysis to permit comparison with previous work and with experiment. Since no provision was made to keep a careful inventory of momentum flux in these models, the ablation pressure as usually obtained experimentally cannot be determined. Instead, we define P_{ab} as the maximum pressure achieved in the model at a time shortly after peak laser power. Usually, this is also the peak pressure in time. This is intended to provide a rough comparison with the experimental measurement derived from the time-averaged debris momentum.

The present survey of models includes sequences in which each of the independent parameters are varied in a systematic way about the standard model UO. The multivariate fits given here thus represent scaling laws in the vicinity of the standard model, i.e., a local approximation to the actual global relations, which could be nonlinear in the log-log plane. In some cases, such as the wavelength scaling, the manner in which the variation is done is of prime importance, and here the discussion in the relevant previous sections will be more useful than the general relation.

10-3 RESULTS.

Looking first at the very strong relations given in Table 10-2, we find strong dependence of the coronal mass on the intensity and on the laser energy (linearly). The intensity effect is due primarily to the smaller targets used to obtain high intensities at fixed laser energy. This relationship is readily understood as the mass varying directly with the energy deposited and with the surface area of the target. The ion velocities are found to depend strongly on the intensity, as predicted by the energy balance model discussed in Section 4. In addition, the velocity at the ion distribution peak depends on the laser pulse length, due to increased laser energy and smaller radiative losses with longer pulses. Finally, the maximum electron temperature also tracks the intensity and the pulse length, for the same reasons as the ion velocity. All of the strong relations are consistent with the single parameters fits given in each section and with the previous results given in Reference 1, with the exception of the coronal mass scaling - the mass is defined differently in the present analysis.

The "first" parameter relations given in Table 10-3 are useful to quickly determine the principal factor in each case (the one parameter that explains the greatest amount of variation in the given variable). In all cases, the exponent agrees with the general result given in Table 10-1.

The scaling summary given in Table 10-1 represent the most general digest of the results of this survey. All significant correlations have been included. The greatest uncertainty is associated with the weaker terms in each fit, which could be influenced by the choice of models actually computed.

Clearly the most important single variable is the intensity, which appears in every relation (except $\Delta U/U$), although it is not always

100

the strongest determiner of a given quantity. Comparison with the indivi-
dual fits given in each section shows that the multivariate results are, in
general, consistent with the partial correlations, with the single excep-
tion of the dependence of the coronal mass on the pulse length, a weak term
in the relation because the pulse length and the laser energy are also
correlated. Another point of interest is the dependence of the coronal
temperatures and velocities on laser wavelength: the exponents found here
are generally larger than those computed from sequence U4C, and closer to
the expected variation of $\lambda^{0.4}$ (see Section 6).

10-4   COMPARISON WITH OTHER RESULTS.

This survey, although intended as a tool for specific HANE appli-
cations, is general enough to allow comparison with many previous theoreti-
cal and experimental analyses of laser phenomena. In this section, several
recent papers are reviewed to place the present results in proper perspec-
tive.

Of most interest are the experimental results obtained at NRL.
In experiments just preceding the current HANE simulations, Grun, et. al.[5]
measured ablation pressure, debris velocity, and mass ablation rate, with
the results:

$P_{ab} \propto I^{0.8}$		(0.89, U2)
$U \propto I^{0.2}$	(0.22, L1)	(0.29, U2)
$dm/dt \propto I^{0.6}$	(0.54, L1)	(0.40, U2)

where the exponents as determined by the present survey are given in paren-
theses: for the intensity sequence (U2), and for the low power sequence
(L1), as indicated. The mass ablation rate per unit area is obtained by
adding unity to the total coronal mass exponent. The low power results are
in very good agreement with the experimental values , while the U2 numbers
can be taken as an indication of the effect of higher laser energies and
intensities.

101

As a second data point, we examine the results of Mead et. al.[6], who present LASNEX calculations as well as experimental data obtained with the Argus laser at Livermore. Most of these numbers refer to much lower laser energies and shorter pulse lengths than addressed in this report, but the comparison is interesting nevertheless. The first result of interest concerns several shots with different laser energies, but with the spot size varied to obtain the same intensity, as in sequence U1. They report "no spot-size dependent effects were observed." The shots in question were at laser energies of 12 J and 33 J, at the lower limit of the U1 sequence. Examination of Figures 3-2 through 3-8 shows that most quantities show only a small variation across this energy range, consistent with the above statement, but do show a stronger dependence on laser energy at higher energies. This prediction needs to be tested in future experiments on the upgraded system.

Also reported in this reference is the dependence of absorption on laser wavelength and intensity: absorption is found to be near unity at wavelength 0.25 microns, dropping to 0.4 at 1.06 microns, and also near unity at intensities below 10^{14} W/cm^2, dropping to 0.4 at about 3×10^{15} W/cm^2. Comparing with sequence U4C (Table 6-7), we have agreement at short wavelengths, but our curve remains at about 0.90 at 1.06 microns. This is an effect of the short pulses used by Mead et. al.,[6] as seen in sequence U5 (Table 7-2). The intensity results in Table 4-2 are in much better agreement, dropping to 0.49 at 10^{16} W/cm^2, but also reflect the pulse length effect to a degree.

Max[7] reports experimental results obtained at École Polytechnique for laser absorption as a function of wavelength, intensity, and laser pulse length, with results very similar to those reported in the previous reference. Here, however, a full curve of results are shown for the case: 1.06 microns and pulse length = 2.5 ns, reproduced here in Figure 10-1. These experimental points fall only slightly below those shown in

Table 9-2 (Sequence L1), consistent with the somewhat longer pulse length in the HANE models. Note that the models in sequence U2 (higher laser energy) show a considerably higher absorption, a very favorable trend if confirmed.

Combining the results given in Tables 10-1 and 7-3, the present survey predicts:

$$\text{Absorption} \propto \text{Intensity}^{-0.1} \times \text{Wavelength}^{-0.24} \times \text{Pulse Length}^{0.1}$$

Although many more studies of this type of laser experiment are available, the above examples suffice to show several points of agreement as well as several discrepancies between present models and previous work. In many cases we have identified trends of considerable benefit to the HANE program on the upgraded NRL laser, and these items should be carefully investigated.

10-5   SUMMARY OF IMPORTANT SCALING LAWS.

We summarize here the scaling laws found that are of particular interest to HANE simulations.

1. Laser Absorption $\propto I^{-.1} \lambda^{-.25}$

2. Ion Velocity $\propto I^{.3} \lambda^{.2} FW^{.5}$

3. Ion Velocity Spread $\propto E^{.4} \lambda^{1} FW^{-1}$

4. Outer Temperature $\propto I^{.5} E^{.3} \lambda^{1} FW^{1.5}$

where I is the absorbed laser intensity, E is the laser energy, λ is the laser wavelength, and FW represents the laser pulse length (FWHM).

Assuming that all of the above quantities should be maximized except the velocity spread, which should be minimized, we obtain the following general conclusion:

1. Increasing I improves all quantities except the absorption, which is a very weak effect.

2. Increasing E will increase temperatures but also increase the velocity distribution width.

3. Decreasing the wavelength will improve absorption and narrow the ion distribution but decreases ion velocities and temperatures.

4. Increasing the pulse length does not affect the absorption and is favorable in all of the other cases.

We caution that in nearly all aspects of target design, other considerations are important that modify these general conclusions. See the appropriate section of this report for detailed discussions of each factor.

TABLE 10-1.
SUMMARY OF PARAMETER SCALING (F ≥ 4)

ITEM	SCALING LAW	F LEVEL
1. Integrated Absorption	$\alpha_{INT} \propto I^{-0.10 \pm .02}\, \lambda^{-0.24 \pm .06}$	6/14
2. Kinetic Energy Fraction	$KEF \propto I^{-0.10 \pm .01}\, E^{-0.07 \pm .02}\, Z^{-0.25 \pm .06}$	23/10/17
3. Radiated Energy Fraction	$REF \propto I^{-0.22 \pm .04}\, \lambda^{-0.43 \pm .1}\, Z^{1.6 \pm .2}$	11/15/30
4. Coronal Mass	$M \propto I^{-0.60 \pm .04}\, E^{1.0 \pm .06}\, \lambda^{-0.7 \pm .1}\, FW^{-0.6 \pm .1}$	48/26/17/16
5. Ion Velocity at Distribution Peak	$U_{ion} \propto I^{0.29 \pm .02}\, \lambda^{0.17 \pm .04}\, FW^{0.51 \pm .04}$	55/15/70
6. Maximum Ion Velocity	$U_{max} \propto I^{0.28 \pm .02}\, E^{0.07 \pm .02}\, \lambda^{0.30 \pm .06}$	94/8/15
7. Velocity Distribution Width	$\Delta U/U \propto E^{0.38 \pm .1}\, \lambda^{1.3 \pm .2}\, FW^{-1.4 \pm .3}$	11/13/12
8. Critical Surface Radius	$R_{crit} \propto I^{-0.93 \pm .1}\, E^{0.4 \pm .2}$	35/5
9. Outer Target Radius	$R_{out} \propto I^{0.15 \pm .03}$	19
1 . Maximum Electron Temperature	$T_{max} \propto I^{0.42 \pm .05}\, E^{0.16 \pm .07}\, \lambda^{0.4 \pm .1}\, FW^{1.8 \pm .2}$	54/6/5/40
11. Outer Coronal Temperature	$T_{out} \propto I^{0.46 \pm .06}\, E^{0.3 \pm .1}\, \lambda^{1.0 \pm .2}\, FW^{1.5 \pm .2}$	16/10/14/20
12. Outer Coronal Density	$\rho_{out} \propto I^{-1.1 \pm .1}\, E^{0.7 \pm .2}$	36/22
13. Ablation Pressure	$P_{ab} \propto I^{0.89 \pm .08}\, \lambda^{-0.4 \pm .2}$	189/4

I = absorbed intensity, E = laser energy, λ = wavelength, FW = laser pulse length, Z = target material Z.

TABLE 10-2.

STRONG PARAMETER SCALING (F $\geq$ 48)

ITEM	SCALING LAW	F LEVEL
4. Coronal Mass	$M \propto I^{-0.48 \pm .07} E^{1.0 \pm .1}$	48
5. Ion Velocity	$U_{ion} \propto I^{0.25 \pm .02} FW^{0.50 \pm .06}$	71
6. Maximum Ion Velocity	$U_{max} \propto I^{0.24 \pm .02}$	94
10. Maximum Electron Temperature	$T_{max} \propto I^{0.38 \pm .05} FW^{1.9 \pm .2}$	53
13. Ablation Pressure	$P_{ab} \propto I^{0.97 \pm .07}$	189

TABLE 10-3.

PRINCIPLE PARAMETER SCALING (FIRST FACTOR)

ITEM	SCALING LAW	F LEVEL
1. Integrated Absorption	$\alpha_{INT} \propto I^{-0.06 \pm 0.02}$	6
2. Kinetic Energy Fraction	$KEF \propto I^{-0.08 \pm 0.02}$	23
3. Radiated Energy Fraction	$REF \propto Z^{1.6 \pm .3}$	30
4. Coronal Mass	$M \propto E^{0.8 \pm .2}$	26
5. Ion Velocity at Distribution Peak	$U_{peak} \propto I^{0.26 \pm .03}$	55
6. Maximum Ion Velocity	$U_{max} \propto I^{0.24 \pm .02}$	94
7. Velocity Distribution Width	$\Delta U/U \propto \lambda^{1.1 \pm .3}$	13
8. Critical Surface Radius	$R_{crit} \propto I^{-0.8 \pm .1}$	35
9. Outer Target Radius	$R_{out} \propto I^{0.15 \pm .03}$	19
10. Maximum Electron Temperature	$T_{max} \propto FW^{2.0 \pm .3}$	40
11. Outer Coronal Temperature	$T_{out} \propto FW^{1.7 \pm .4}$	20
12. Outer Coronal Density	$\rho_{out} \propto I^{-0.95 \pm .1}$	36
13. Ablation Pressure	$P_{ab} \propto I^{0.89 \pm .1}$	189

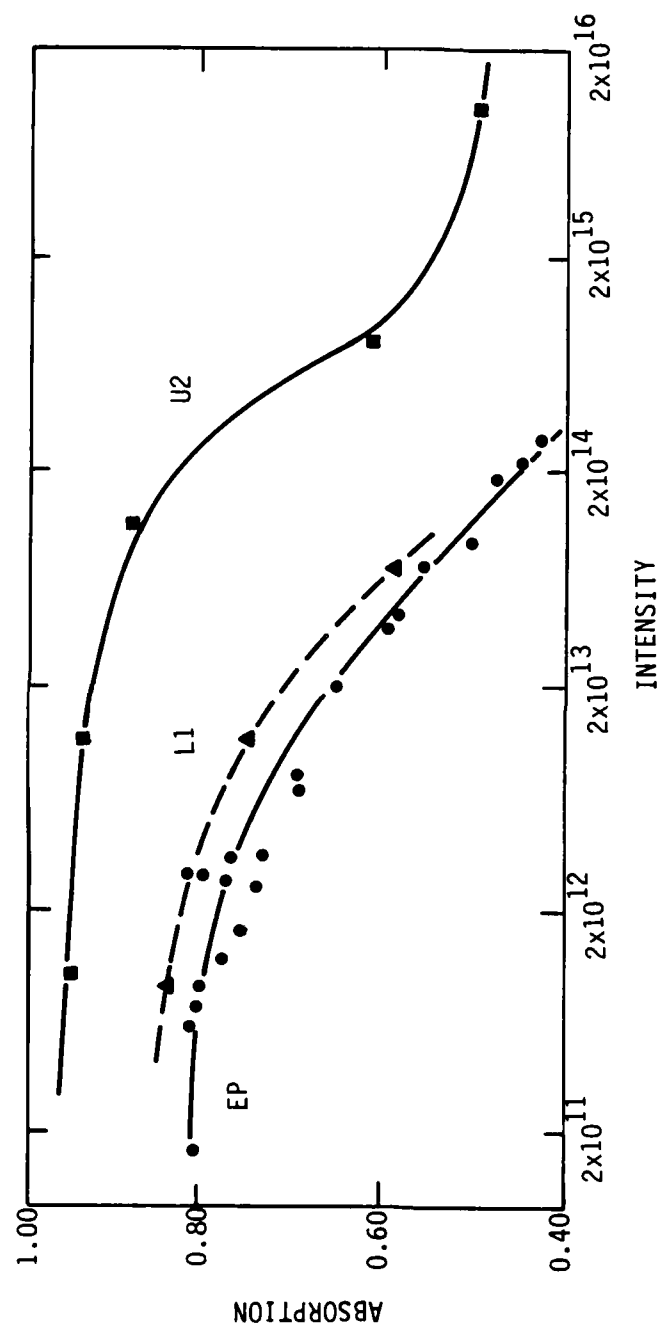I = absorbed intensity, E = laser energy, λ = wavelength, FW = laser pulse

Figure 10-1. Laser absorption versus intensity for three cases: "EP": experimental results from Ecol Polytechnique, λ = 1.06 microns, pulse length = 2.5 ns. "L1": low power sequence, pulse length = 3.4 ns. "U2": shows the expected effect of larger laser energy (spot size).

108

REFERENCES

1. Stellingwerf, R. F., C. L. Longmire and M. L. Alme, "Laser Simulation of Early-Time HANE Phenomena," AMRC-R-465, Mission Research Corporation, April 01, 1983.

2. Langdon, A. B., Phys. Rev. Lett., 44, 575 (1980).

3. Jones, R. D. and K. Lee, Phys. Fluids, 25, 2307 (1982).

4. Ripin, B. H., J. Grunn, S. Kacenjar, E. A. LcLean and J. A. Stamper, 1984, NRL Report 5768.

5. Grun, J., S. P. Obenschain, B. H. Ripin, R. R. Whitlock, E. A. McLean, J. Gardner, M. H. Herbst and J. A. Stamper, 1982, NRL Report 4747.

6. Mead, W. C., E. M. Cambell, K. G. Estabrook, R. E. Turner, W. L. Kruer, P. H. Y. Lee, B. Pruett, V. C. Rupert, K. G. Tirsell, G. L. Stradling, F. Ze, C. E. Max, M. D. Rosen and B. F. Lasinski, 1983, Phys. Fluids, 26, 2316.

7. Max, C. E., 1981, Livermore Report UCRL - 53107.

DISTRIBUTION LIST

DEPARTMENT OF DEFENSE

Defense Nuclear Agency
       ATTN: STNA
       ATTN: RAEE
       ATTN: NAWE
       ATTN: RAAE, P. Lunn
       ATTN: NATF
       ATTN: RAAE, K. Schwartz
3 cys ATTN: RAAE
4 cys ATTN: STTI-CA

Defense Tech Info Ctr
12 cys ATTN: DD

DEPARTMENT OF THE NAVY

Naval Research Laboratory
       ATTN: Code 4720, J. Davis
       ATTN: Code 4700, S. Ossakow
       ATTN: Code 7500, B. Wald
       ATTN: Code 4780
       ATTN: Code 4700
       ATTN: Code 4187
       ATTN: Code 7950, J. Goodman
       ATTN: Code 6700
       ATTN: Code 4108, E. Szuszewicz

DEPARTMENT OF THE AIR FORCE

Air Force Weapons Laboratory
       ATTN: SUL
       ATTN: NTN

DEPARTMENT OF ENERGY CONTRACTORS

Los Alamos National Laboratory
       ATTN: D. Sappenfield
       ATTN: J. Wolcott
       ATTN: R. Jeffries
       ATTN: P. Keaton
       ATTN: D. Simons
       ATTN: G-6, E. Jones
       ATTN: MS 664, J. Zinn
       ATTN: J. Hopkins
       ATTN: T. Kunkle, ESS-5

DEPARTMENT OF DEFENSE CONTRACTORS

Berkeley Rsch Associates, Inc
       ATTN: J. Workman
       ATTN: C. Prettie
       ATTN: S. Brecht

DEPARTMENT OF DEFENSE CONTRACTORS (Continued)

EOS Technologies, Inc
       ATTN: B. Gabbard
       ATTN: W. Lelevier

JAYCOR
       ATTN: H. Dickinson

JAYCOR
       ATTN: J. Sperling

Kaman Tempo
       ATTN: DASIAC

Kaman Tempo
       ATTN: B. Gambill
       ATTN: DASIAC
       ATTN: W. McNamara

Mission Research Corp
2 cys ATTN: R. Stellingwerf

Mission Research Corp
       ATTN: G. McCartor
       ATTN: F. Guigliano
       ATTN: Tech Lib
       ATTN: F. Fajen
       ATTN: R. Bogusch
       ATTN: R. Hendrick
       ATTN: D. Knepp
       ATTN: R. Kilb
       ATTN: S. Gutsche
       ATTN: R. Dana
       ATTN: C. Lauer
       ATTN: R. Bigoni

Pacific-Sierra Research Corp
       ATTN: E. Field, Jr
       ATTN: F. Thomas
       ATTN: H. Brode, Chairman SAGE

R&D Associates
       ATTN: P. Haas

Toyon Research Corp
       ATTN: J. Garbarino
       ATTN: J. Ise

Visidyne, Inc
       ATTN: H. Smith
       ATTN: J. Carpenter
       ATTN: W. Reidy
       ATTN: O. Shepard
       ATTN: C. Humphrey

END

FILMED

8-85

DTIC